To the Graduate Council:

I am submitting herewith a dissertation written by Kathryn A. Walter entitled "Geochemistry and Trace-Element Models for the Petrogenesis of Mafic rocks in the Hayesville Thrust Sheet, Georgia-North Carolina Blue Ridge." I have examined the final copy of this dissertation for form and content and recommend that it be accepted for the degree of Doctor of Philosophy with a major in Geology.

Harry Y. McSween
Major Professor

We have read this dissertation
and recommend its acceptance:

Accepted for the Council:

Vice Provost
and Dean of The Graduate School

GEOCHEMISTRY AND TRACE-ELEMENT MODELS FOR THE PETROGENESIS OF MAFIC ROCKS IN THE HAYESVILLE THRUST SHEET, GEORGIA-NORTH CAROLINA BLUE RIDGE

A Dissertation

Presented for the

Doctor of Philosophy

Degree

The University of Tennessee, Knoxville

Kathryn A. Walter

August, 1990

ACKNOWLEDGMENTS

The author would like to thank committee chairman, Dr. Harry Y. McSween, Jr., for suggesting the mafic rocks of the Blue Ridge as a topic for this study and for many helpful suggestions throughout the project. Discussions with committee members Dr. Kula C. Misra, Dr. Theodore C. Labotka and Dr. Jeffrey Kovac and their help in improving the final draft are greatly appreciated. Dr. Otto Kopp provided valuable assistance in operating the X-ray fluorescence equipment. Contributions of samples and analyses by Roger Kittelson and Janet Hopson and outcrop maps of the field area compiled by Dr. Robert D. Hatcher's group greatly shortened sample collection time. The U.S. Forest Service allowed access to logging roads, which also aided in sampling. Finally, special thanks go to my family and friends for encouragement throughout the project.

ABSTRACT

Abundant mafic rocks, mostly amphibolites, occur near the leading edge of the Hayesville Thrust sheet in the eastern Blue Ridge Province of northern Georgia and southwestern North Carolina. These rocks are found in three large mafic/ultramafic complexes - Chunky Gal Mountain, Carroll Knob and Lake Chatuge, in the Kimsey Bald amphibolite body, and in isolated bodies, pods or lenses in the metasedimentary host rocks of the region. Petrologic and geochemical data indicate that the protoliths of all the amphibolites of the region were cumulate rocks. Bulk-rock X-ray fluorescence data for Chunky Gal Mountain, Kimsey Bald and isolated amphibolites and many of the Lake Chatuge amphibolites show similar major-, minor- and trace-element abundances and trends. Comparison of mathematical models of cumulate processes with immobile trace- and minor-element patterns for these rocks indicates that the trends result from the trapping of residual liquid among cumulus crystals. Although the coexistence of cumulus crystals and trapped liquid in these rocks altered bulk-rock trace- and minor-element abundances and ratios from liquid values, a liquid composition can be estimated from the model. The model-derived liquid composition indicates that the parent magma of these suites was tholeiitic and is consistent with genesis in either an ocean floor or within-plate setting.

The compositions of the rocks from the Carroll Knob Complex cannot be related to those of the other four suites by any plausible magmatic process, and the Carroll Knob rocks must have been derived from a parent magma of different trace- and minor-element composition. The estimated Carroll Knob liquid composition is most compatible with a tholeiitic arc basalt. Relict igneous lithologies observed at the mafic/ultramafic complexes and inferred phase relations also suggest the parent magma for the Carroll Knob Complex was different from that of the other mafic rocks of the region and are consistent with the inferred tectonic settings.

TABLE OF CONTENTS

CHAPTER		PAGE
I.	INTRODUCTION	1
II.	FIELD RELATIONS AND PETROLOGY	8
	Introduction	8
	Regional Setting	8
	Carroll Knob Complex	14
	Field Relations	14
	Petrology	18
	Amphibolites	19
	Metagabbros and Pyroxenites	23
	Epidosites and Hornblendites	28
	Chunky Gal Mountain Complex	29
	Field Relations	29
	Petrology	33
	Amphibolites	33
	Dunites and Troctolites	35
	Kimsey Bald Amphibolites	36
	Field Relations	36
	Petrology	37
	Lake Chatuge Complex	38
	Field Relations	38
	Petrology	40
	Isolated Amphibolites	43
	Field Relations	43
	Petrology	44
III.	GEOCHEMISTRY	46
	Introduction	46
	Major-Element Chemistry	51
	Igneous Protoliths	52
	AFM Diagrams - Magma Types and Trends	54
	Differentiation Index	57
	Cumulate Components and Two-Element Variation Diagrams	57
	Trace- and Minor-Element Chemistry	68
	Trends	68
	Element Mobility	77
IV.	MODELS FOR TRACE-ELEMENT EVOLUTION IN CUMULATE ROCKS	79
	Introduction	79

Approach 79
Constraints 83
Bulk Distribution Coefficients 83
Other Parameters 92
Closed-System Fractional Crystallization (CFC) 93
Two-Element Plots 95
Computer-Generated Plots 96
CFC Model Curves 97
Cumulate with Trapped Intercumulus Liquid (CTL) 100
Constant k 100
Estimating Liquid Compositions 101
Trends Produced by Variable k (CTL Model Curves) 102
Fractionation of Elements 106
Estimating k 108
Combined Liquid Trapping and Fractionation 110
Crystal Sorting 110
Combined Crystal Sorting and Fractionation 115
Open-System Fractional Crystallization (OFC) 116
Additional Processes 124

V. PETROGENETIC MODELS FOR THE MAFIC SUITES . . . 126

Introduction 126
Models for the Chunky Gal Mountain, Isolated and Kimsey Bald Amphibolites 127
Introduction 127
Chunky Gal Mountain 128
Closed-System Fractional Crystallization 128
Cumulate Plus Trapped Liquid Model . . . 138
Metamorphic Processes 147
Liquid Composition 148
Isolated Amphibolites and Kimsey Bald Amphibolites 155
Models for the Lake Chatuge Complex 157
Models for the Carroll Knob Complex 162
Relationships to the Chunky Gal Mountain/Isolated Amphibolite Trends . . . 162
Liquid Composition 169
Relationships Within the Carroll Knob Suite 172
Phase Relations and Crystallization Sequences 177

VI. CONCLUSIONS 182

REFERENCES 184

APPENDICES 192

Appendix A - Electron Microprobe Data and Geothermometry for Carroll Knob Complex Pyroxenes 193
Appendix B - XRF Analytical Methods and Data . . . 200

VITA 224

LIST OF TABLES

TABLE		PAGE
1.	Relict Lithologies	13
2.	Correlation Coefficients for Least Squares Linear Regressions between Selected Elements and Zr	76
3.	Mineral/Liquid Partition Coefficients	85
4.	Bulk Distribution Coefficients for Model Eutectic Assemblages	90
5.	Estimated Liquid Compositions	149

LIST OF FIGURES

FIGURE		PAGE
1.	Generalized Geological Map of the Study Area . . .	2
2.	Generalized Lithologic Map of the Carroll Knob Complex, Modified from Hatcher (1980)	16
3.	Generalized Lithologic Map of the Chunky Gal Mountain Complex and the Kimsey Bald Amphibolite Body	31
4.	Generalized Lithologic Map of the Northern Portion of the Lake Chatuge Complex	39
5.	Discriminant Diagrams for Para- and Ortho-Amphibolites from Leake (1964)	53
6.	AFM Diagrams from Irvine and Baragar (1971)	55
7.	Plots of CaO + MgO (wt. %) Versus Zr (ppm)	59
8.	Plots of MgO (wt. %) Versus Zr (ppm)	62
9.	Plots of CaO (wt. %) Versus Zr (ppm)	63
10.	Plots of Total Iron Calculated as Fe_2O_3 (wt. %) Versus Zr (ppm)	64
11.	Plots of SiO_2 (wt. %) Versus Zr (ppm)	65
12.	Plots of Na_2O (wt. %) Versus Zr (ppm)	66
13.	Plots of Al_2O_3 (wt. %) Versus Zr (ppm)	67
14.	Plots of TiO_2 (ppm) Versus Zr (ppm)	69
15.	Plots of Y (ppm) Versus Zr (ppm)	70
16.	Plots of P_2O_5 (ppm) Versus Zr (ppm)	71
17.	Plots of Nb (ppm) Versus Zr (ppm)	72
18.	Plots of Ni (ppm) Versus Zr (ppm)	73
19.	Plots of Cr (ppm) Versus Zr (ppm)	74

20. Phase Diagrams and ACF Plots 88

21. CFC Model Liquid and Cumulate Lines for an Olivine Gabbro Cumulus Assemblage 98

22. Selected CTL (Filled Symbols) and CFC (Open Symbols) Model Curves for an Olivine Gabbro Cumulus Assemblage 103

23. Model Curves for the Ratio C_i/C_j Vs C_j for Incompatible Elements for an Olivine Gabbro Cumulus Assemblage 107

24. Crystal Sorting Curve (Filled Circles) Superimposed on CTL and CFC Curves for $\bar{D}_j = 0.06$ and $\bar{D}_i = 0.17$. $D_i^p = 50$, and $D_j^p = 0.28$ 113

25. AFC Model Cumulate or Liquid Curves for an Olivine Gabbro Cumulus Assemblage (Filled Symbols) and Selected CFC Lines (Open Symbols) for Comparison 120

26. Chunky Gal Mountain Complex Data for Selected Elements Plotted Against Zr with Linear Regression Lines Fit to the Amphibolite Data . . 130

27. Chunky Gal Mountain Complex Data for Selected Elements Plotted Against Zr with CTL Model Curves and Corresponding CFC Model Cumulate and Liquid Lines Superimposed 138

28. Model-derived Liquid Composition (Large Lined Symbol) and Chunky Gal Mountain Complex Amphibolite Data Plotted on Diagrams Showing Basalt Fields 151

29. Selected Isolated Amphibolite Data Plotted Against Zr with Chunky Gal Mountain CTL Model Curves and Corresponding CFC Model Cumulate and Liquid Lines Superimposed 156

30. Selected Lake Chatuge Complex Data Plotted Against Zr with Chunky Gal Mountain CTL Model Curves and Corresponding CFC Model Cumulate and Liquid Lines Superimposed 158

31. Selected Carroll Knob Complex Data Plotted Against Zr with Chunky Gal Mountain CTL Model Curves and Corresponding CFC Model Cumulate and Liquid Lines Superimposed 163

32. Carroll Knob Complex Data for TiO_2 Vs Zr with Ilmenite Sorting Curves 175

33. Phase Diagram Models Adapted from Irvine (1970) Showing Hypothetical Liquid Compositions and Liquid Fractionation Paths (Connected Squares and Arrows) Consistent with Observed Relict Lithologies 178

A.1. Data for Selected Carroll Knob Complex Coexisting Orthopyroxenes and Clinopyroxenes Projected onto a Pyroxene Quadrilateral Showing Polythermal Orthopyroxene + Augite, Orthopyroxene + Augite + Pigeonite, and Pigeonite + Augite Relations, Contoured at 100 ^{0}C Intervals for Use in Geothermometry (from Lindsley, 1983) 199

CHAPTER I

INTRODUCTION

Mafic rocks, consisting mostly of amphibolites and subsidiary metagabbros and troctolites, are abundant in the eastern Blue Ridge Province in northern Georgia and southwestern North Carolina (Figure 1). These rocks occur associated with ultramafic rocks in large mafic/ultramafic complexes, in amphibolite bodies of various sizes and in small pods or lenses in metasedimentary host rocks (Misra and McSween, 1984). Three large mafic/ultramafic complexes - the Lake Chatuge Complex, the Chunky Gal Mountain Complex and the Carroll Knob Complex - occur near the leading edge of the Hayesville Thrust. The Hayesville Thrust appears to mark an important boundary between the basement and shelf/slope metasedimentary rocks of the western Blue Ridge and the deeper-water metasedimentary, granitic and mafic rocks of the eastern Blue Ridge (Rankin, 1975; Hatcher, 1978; Wehr and Glover, 1985). The occurrence of deep-water metasediments and mafic rocks in the eastern Blue Ridge is generally regarded as evidence that a late Proterozoic rifting event took place eastward of the ancient continental shelf (Rankin, 1975; Hatcher, 1978; Williams and Hatcher, 1982). Based on their locations near the Hayesville Thrust and on limited petrologic

Figure 1. Generalized geological map of the study area. Geology and isograds from McSween and Hatcher (1985), Hopson (1990), Eckert et al. (1989) and Kittelson (1988). V&R = Valley and Ridge province. BR = Blue Ridge province. P = Piedmont province. CK = Carroll Knob Complex. CGM = Chunky Gal Mountain Complex. KB = Kimsey Bald Amphibolite Body. LCH = Lake Chatuge Complex. Quadrangles are labeled at lower center. CN = Corbin Knob. F = Franklin. P = Prentiss. WB = Wayah Bald. RBS = Rainbow Springs. HB = Hightower Bald. SC = Shooting Creek. Small, lower case letters within quadrangles indicate isolated amphibolite XRF sample locations and are keyed to data presented in Appendix B.

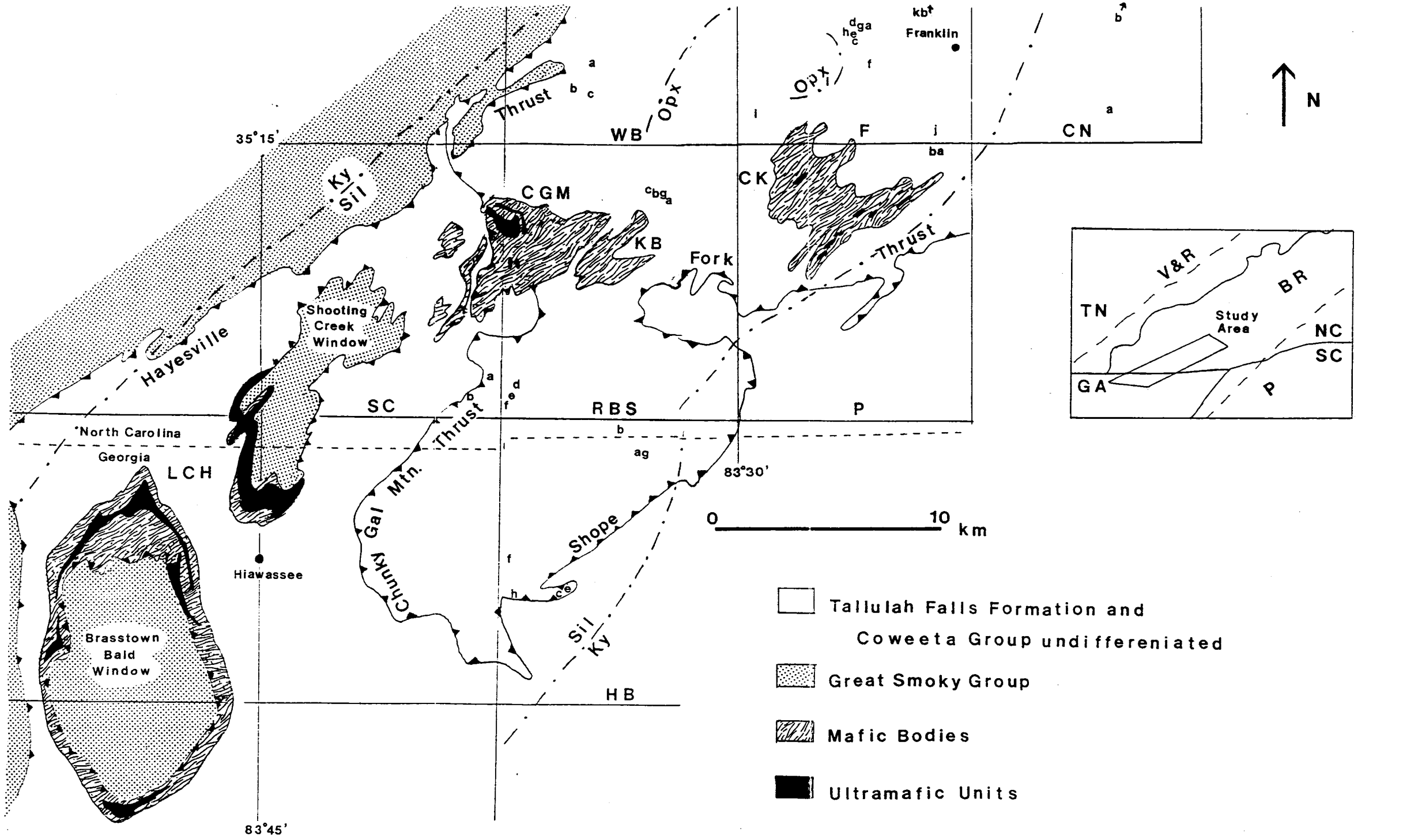
N
35°15'
83°30'
83°45'
Franklin
Opx
Thrust
WB
F
CN
CK
CGM
KB
Fork
Ky
Sil
Hayesville
Shooting Creek Window
SC
RBS
P
North Carolina
Georgia
LCH
Hiawassee
Brasstown Bald Window
Chunky Gal Mtn. Thrust
Shope
Sil
Ky
HB
0
10
km
V&R
BR
TN
Study Area
NC
SC
GA
P
Tallulah Falls Formation and Coweeta Group undifferenciated
Great Smoky Group
Mafic Bodies
Ultramafic Units

and geochemical evidence, several authors have suggested that the mafic/ultramafic complexes may be segments of ophiolites derived from a rift-related ocean floor (Hatcher, 1978; Williams and Hatcher, 1982; Hatcher et al., 1984; McElhaney and McSween, 1983; Shaw and Wasserburg, 1984; McSween and Hatcher, 1985). In fact, McSween and Hatcher (1985) proposed that these bodies are isolated exposures of a continuous layer of oceanic crust on which host-rock sediments were deposited, and that this substratum is exposed only near the Hayesville Fault where the thrust sheet is thin. Alternatively, these complexes could be differentiated plutons unrelated to oceanic magmatism (Rankin et al., 1973; McElhaney and McSween, 1983). Distinguishing between these alternatives has obvious tectonic implications for the region.

In addition to the mafic/ultramafic complexes, a smaller amphibolite body, Kimsey Bald, occurs immediately east of the Chunky Gal Mountain Complex, and several other isolated amphibolite bodies, pods or lenses occur throughout this region. Based on geochemical arguments, Eggers (1983) suggested an island arc origin for the Kimsey Bald amphibolites. The mafic bodies and lenses in this area have not previously been studied in detail, but they have been considered by many to be meta-volcanics which were once interlayered with the protoliths of the metasedimentary rocks. Such an origin has been documented for the mafic rocks in the

Ashe Formation which occurs along strike to the north (Abbott and Raymond, 1982; Conte, 1986; Misra and Conte, in press).

Although crucial for understanding the geologic history of the eastern Blue Ridge and despite the previous work mentioned above, the nature and origin of and relationships among the mafic rocks of this region remain obscure. This is in part because strong deformation and high-grade metamorphism have largely obliterated the original field relations between the mafic rocks and the metasediments and have, in addition, destroyed most of the primary textures and mineralogies of the rocks. Consequently, there is a lack of the usual kinds of physical evidence used to evaluate the nature and origin of mafic rocks.

Although little petrographic and field evidence related to these rocks remains, data which will be presented in a later chapter indicate that primary chemical compositions for several elements have been preserved. The main purpose of this dissertation is to explore the origins of and the relationships among the mafic rocks of this region by a comprehensive analysis and comparison of their geochemistries. The geochemical analysis is supplemented and guided by available data on field relations and petrography.

The actual area studied for this dissertation is a northeast-southwest-trending belt approximately 50 km long and 15 km wide which lies southeast of the Hayesville Thrust and northwest of the Shope Fork Thrust (Figure 1). The boundaries

of the area (except for the Hayesville) are somewhat arbitrary. They were chosen because they include the three major mafic/ultramafic complexes in the region, as well as Kimsey Bald and several isolated amphibolite occurrences.

For the purposes of this study, the rocks of the study area are divided into five major suites: Carroll Knob Complex, Chunky Gal Mountain Complex, Lake Chatuge Complex, Kimsey Bald amphibolites and isolated amphibolites. The first four suites are made up of rocks which, because of proximity, are presumably associated with a given complex or body. The isolated amphibolite suite is based primarily on mode of occurrence and includes rocks found in small bodies across the entire study area. Chapter II describes the regional setting and the field occurrence and petrography of each suite of rocks and makes some relevant comparisons among the suites.

Chapter III is mostly devoted to the presentation and discussion of new major- , minor- and trace-element X-ray fluorescence (XRF) data obtained for this dissertation but also includes discussions of XRF data published by other authors. The XRF data indicate that all the suites are of igneous origin. In addition, they suggest that several trace- and minor-elements have been immobile during metamorphism, and are, therefore, reliable indicators of primary chemistry.

Data presented in both Chapters II and III demonstrate that many of the rocks of all five suites have cumulate protoliths, and thus are not likely to represent liquid

compositions. Consequently, many of the standard techniques of igneous petrology are not directly applicable to these suites, and other methods of analysis had to be explored. Chapter IV modifies and extends models of trace-element evolution in liquids to account for processes that are likely to affect trace-element evolution in cumulate rocks and develops type curves that represent how compositional data controlled by the processes would be distributed on two-element variation diagrams. These model curves are then used in Chapter V to explain the geochemical data for the eastern Blue Ridge suites and to make some inferences about liquid compositions, relationships among the suites and possible origins of the rocks.

CHAPTER II

FIELD RELATIONS AND PETROLOGY

Introduction

This chapter describes in more detail the regional setting, field relations and petrology of the five suites of mafic rocks that were introduced in Chapter I. The first section gives an overview of the region and the mafic rocks. It discusses much of the previous work done in this region, including descriptions of regional metamorphism, deformation and tectonic interpretations. The natures of contacts between the mafic rocks and the metasedimentary host rocks and relict igneous mineralogy are briefly reviewed, and results of isotope studies which pertain to the provenance of some of the rocks are also discussed. This first overview section is followed by five sections that describe in more detail available data on field relations and petrology for each suite separately.

Regional Setting

The Hayesville Thrust (Figure 1) is considered to be the southern portion of a major fault system, the Hayesville-Fries-Rockfish Valley Fault, which extends

northward into Virginia and which marks an important boundary between the western Blue Ridge and the eastern Blue Ridge Provinces (Wehr and Glover, 1985). As outlined in Chapter I, deep-water metasediments and mafic rocks in the eastern Blue Ridge indicate a late Proterozoic rifting event in the region (Rankin, 1975; Hatcher, 1978; Williams and Hatcher, 1982). Favret and Williams (1988) interpreted seismic reflection data to indicate the presence of fault-block structures similar to those at rifted continental margins in the basement beneath the allocthonous eastern Blue Ridge and Inner Piedmont, supporting this view. The extent of rifting is debated: it may have resulted only in crustal thinning and the formation of fault-block basins accompanied by subsidence (Wehr and Glover, 1985); or it may have culminated in the formation of an ocean floor underlying what is sometimes referred to as the Proto-Atlantic or Ieapetus Ocean (Rankin, 1975; Hatcher, 1978; Williams and Hatcher, 1982).

Closing of the basins or sea, as the case may be, is thought to have taken place during the Ordovician Taconian Orogeny, causing the present juxtaposition of eastern Blue Ridge rocks against western Blue Ridge rocks along the Hayesville-Fries-Rockfish Valley system and producing the high-grade metamorphism in the region. The entire assemblage was transported at least 100 km westward along the Great Smoky fault system during Alleghenian time (Hatcher and Odom, 1980;

Williams and Hatcher, 1982; Hatcher, 1978; Wehr and Glover, 1985).

The metasedimentary rocks in the region are predominantly late Precambrian biotite gneiss and schists of the Tallulah Falls Formation and Coweeta Group (Hatcher, 1979; Rankin et al., 1973). The metasediments and the mafic rocks were multiply deformed and metamorphosed during Paleozoic time. Metamorphism is commonly upper amphibolite facies in the area shown in Figure 1 but reaches granulite facies in the thermal core of the region centered west of Franklin, North Carolina (Rankin et al., 1973; Hatcher, 1977; Hatcher, 1978; Absher and McSween, 1985; Kittelson, 1988; Force, 1976; Eckert et al., 1989). Force (1976) indicated that the hypersthene isograd crosses the northern portion of the Carroll Knob Complex. However, all the orthopyroxene observed in extensive sampling of that complex done for this study is igneous in origin (see next section), and the location of Force's isograd is incorrect. Data from Kittelson (1988) also indicate that the hypersthene isograd should be farther north. Various dating techniques place the time of peak metamorphism in this part of the Blue Ridge in the Ordovician, and the peak metamorphic event is considered to be associated with the Taconian orogeny (Glover et al., 1983). A later retrograde metamorphic event is indicated by greenschist facies assemblages in many of the mafic rocks across the region (McElhaney and McSween, 1983;

Hatcher et al., 1984; Kittelson, 1988; Eggers, 1983). This event is usually assigned to the Devonian Acadian orogeny.

A regional kinematic sequence for the southern Appalachians has been worked out (Hatcher, 1977; Hatcher, 1978; Hatcher and Butler, 1979), and deformation in the five mafic suites can be correlated with this sequence. Four folding events are recognized in the region. The first generation of folding (F_1), consisting of isoclinal, recumbent flow folds that are probably pre- to synmetamorphic, is uncommon and is not observed in any of the mafic rocks of this study. The second generation of folding (F_2) produced isoclinal, recumbent to upright folds that are associated with the dominant northeast trending foliation (S_2) of both the metasediments and the mafic rocks of the region. These folds are syn- to post-metamorphic and are assigned to the Taconian orogeny. F_2 folds were subsequently refolded by upright isoclinal folds (F_3), and a later event produced crenulations which are designated F_4. These last two folding events did not produce strong penetrative fabrics. The retrograde metamorphic event observed in the region appears to have occurred at the time of F_3 folding.

Similarity of metamorphic and structural characteristics indicate that the mafic rocks of the region were in contact with the metasedimentary host rocks at least by the time of peak metamorphism and F_2 folding. The original natures of the contacts between the mafic rocks and the metasediments are not

altogether clear. Hartley (1973) and Hartley and Penley (1974) suggested that the Lake Chatuge Complex is a sill, but mapping by Hatcher and Butler (1979) and McSween and Hatcher (1985) showed the complex as part of a window in the Hayesville thrust sheet. There is good evidence that the Chunky Gal Mountain Complex is bordered in part by the Chunky Gal Mountain Thrust, and Eggers (1983) suggested that the Kimsey Bald amphibolite body may also be fault-bounded. The original natures of the contacts between the Carroll Knob Complex and the metasediments and between the isolated amphibolites and the metasediments are not known. Geophysical maps published by Favret and Williams (1988) showed strong gravity and aeromagnetic highs centered near the Carroll Knob Complex, and it is possible that the mafic and ultramafic rocks exposed at the surface in this area are parts of a much larger body or sheet of mafic and ultramafic material in the subsurface. All available evidence also suggests that the ultramafic portions of the mafic/ultramafic complexes were in contact with the mafic portions at least by the time of F_2 deformation and peak metamorphism.

Enough relict mineralogy and texture are preserved in the rocks of the three mafic/ultramafic complexes to conclude that they are almost certainly igneous in origin, and that large portions of them probably had plutonic protoliths. Table 1 shows a comparison of the relict lithologies occurring in the complexes.

Table 1. Relict Lithologies

Carroll Knob Complex[a]	Chunky Gal Mountain Complex[b]	Lake Chatuge Complex[c]
	Dunite	Dunite
	Troctolite	Troctolite
		Ol-Gabbro
		Wehrlite**
Websterite		
Clinopyroxenite		Pyroxenite**
2Px-Gabbro		2Px-Gabbro**
Cpx-Gabbro		Cpx-Gabbro

Wehrlite = Ol + Cpx, and websterite = Opx + Cpx.
[a]Reported by Hatcher (1980) or observed in this study.
[b]Reported by McElhaney (1981).
[c]Reported by Hartley (1973).
**minor float

These lithologies are discussed in detail below, but I note here that the primary igneous lithologies at Carroll Knob appear to have been different from those at Chunky Gal Mountain and Lake Chatuge. No relict mineralogy has been observed at Kimsey Bald or in the isolated amphibolites.

Some whole-rock isotope data are available for the amphibolites of the Chunky Gal Mountain and Lake Chatuge complexes. Neodymium isotope data for two Chunky Gal Mountain amphibolites and one Lake Chatuge amphibolite have the signature of oceanic crust ($\epsilon_{Nd} > +5$) (Shaw and Wasserburg, 1984). Sr^{87}/Sr^{86} isotope ratios obtained for Lake Chatuge samples by Jones et al. (1973) are in the range of mantle values, 0.7023 to 0.7047, which is consistent with the neodymium results. Although there is a good possibility of post-crystallization isotopic exchange in the strontium system, the Nd system appears to preserve original isotopic compositions even at the high grade of metamorphism observed in the region. Isochrons were not obtained in either study.

Carroll Knob Complex

Field Relations

The Carroll Knob Complex is located about 6 km south of Franklin, North Carolina (Prentiss Quadrangle, North Carolina, 7.5′ series, 167-SW). The complex covers an area of approximately 15 km^2 and consists of a large, irregularly

shaped, body of amphibolite, which encloses much smaller bodies of metagabbros, ultramafic rocks, epidosites, and hornblendites (Figure 2). A geologic map of the Prentiss quadrangle was prepared by Hatcher (1980). Field work done for this dissertation generally confirms the contacts and structural trends mapped by Hatcher for the Carroll Knob Complex. Figure 2 is based on Hatcher's map but contains some changes related to the locations and lithologies of metagabbro and ultramafic bodies. The main changes are the addition of a large metagabbro/ultramafic body south of Carroll Knob, the addition of metagabbro associated with a large ultramafic body in the northern portion of the complex, and the reclassification of several bodies, which were mapped by Hatcher as melagabbros or dunites, but are actually associations of epidosites and hornblendites.

The amphibolites of the complex are in contact with rocks of the late Precambrian Tallulah Falls Formation. The outline of the contact is highly irregular and suggests a complex fold interference pattern (Hatcher et al., 1984). No data were obtained either by Hatcher or this author that would suggest the nature of the contact between the complex and the Tallulah Falls Formation. Hatcher (1979) suggested that the Tallulah Falls formation in this quadrangle is thrust over the younger (late Precambrian or early Paleozoic) Coweeta Group along the Shope Fork Thrust, and small windows of Coweeta group rocks are mapped within the Carroll Knob Complex, although my

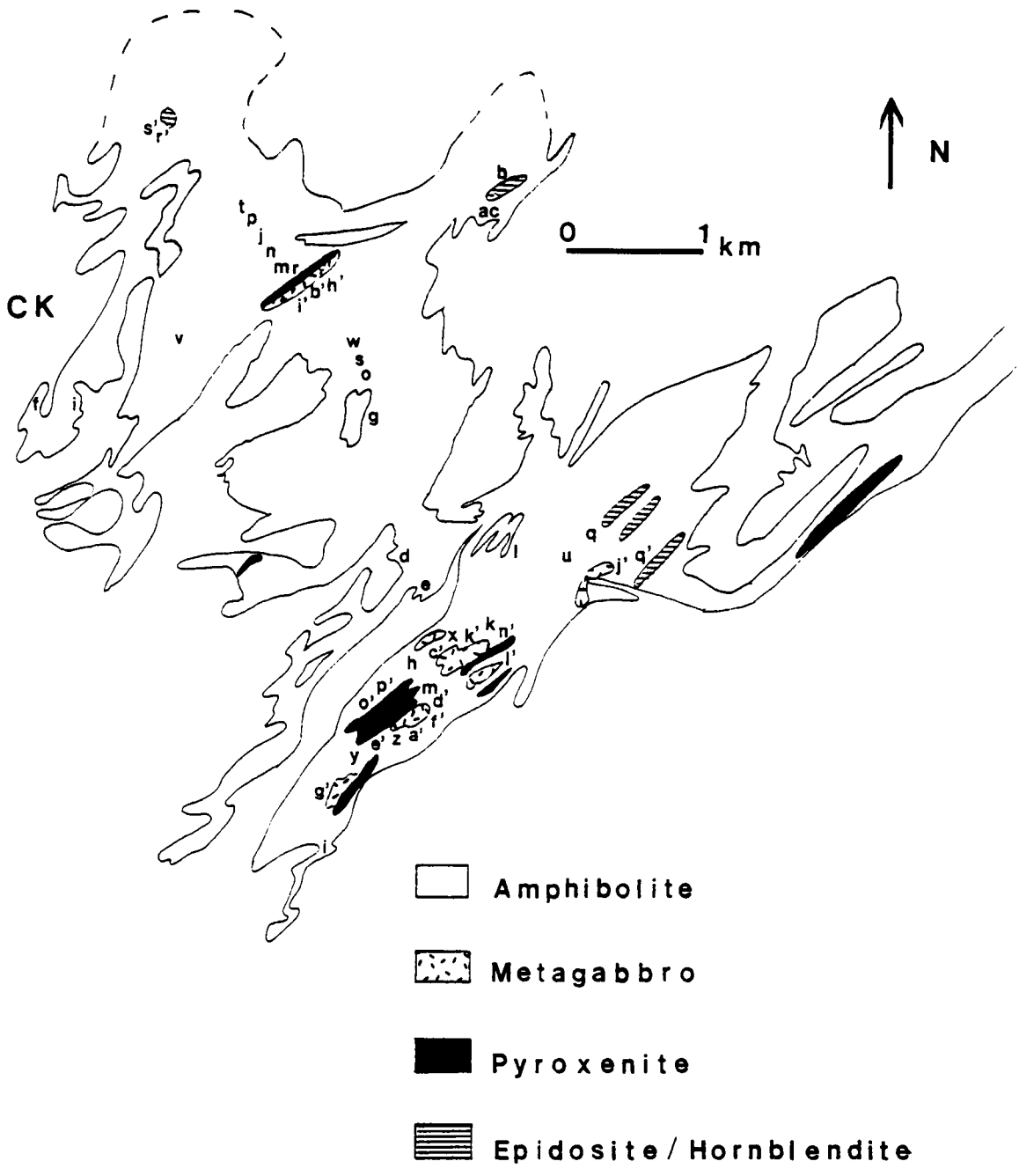

Figure 2. Generalized lithologic map of the Carroll Knob Complex, modified from Hatcher (1980). See Figure 1 for regional location. Small, lower case letters indicate XRF sample locations and are keyed to data presented in Appendix B.

examination of these contacts provided no evidence of the nature of the contacts.

The dominant fold generation in both the metasedimentary rocks and all the lithologies of the Carroll Knob Complex is F_2. Foliation surfaces trend predominantly northeast-southwest and dip from about 30^0 to 80^0 to either the southeast or northwest. Additional centimeter-scale folding in the amphibolites was observed at one location. Where outcrop is best (in the northern portion of the complex) quartz-filled joints in at least three orientations cross cut the amphibolites. Compositional layering, on scales from centimeters to meters, is common in the amphibolites and is parallel to foliation.

Metamorphic index minerals in the metasedimentary rocks, as mapped by Hatcher, indicate that the rocks of the complex have undergone kyanite- to sillimanite-grade metamorphism, with metamorphic grade increasing from southeast to northwest. Amphibolite assemblages observed in this study are consistent with this picture: metamorphic clinopyroxene and scapolite are observed only in the northwestern half of the complex. Garnet-bearing amphibolites and those not containing garnet are intercalated across the entire complex, indicating that the occurrence of garnet is controlled by relatively small-scale compositional variations and is not an indicator of metamorphic grade.

As is evident from Figure 2, amphibolites constitute by far the most abundant rock type of the complex. These amphibolites include several mineralogical and textural varieties, which will be discussed in more detail in the petrology section below.

The metagabbros and ultramafic rocks almost always occur spatially associated with each other as lenses or pods within the amphibolite. The ultramafic rocks are pyroxenites, mostly clinopyroxenites, and their metamorphosed equivalents. No olivine was observed in rocks from the complex. The nature of the contacts between the metagabbro/ultramafic associations and the amphibolite could not be inferred from field evidence, although field mapping suggests that the contacts are concordant with foliation.

Small lenses or pods of epidosite and hornblendite occur within the amphibolites of the complex. These two lithologies are also always spatially associated with each other. Again the nature of the contacts between these rocks and the amphibolites is not known, although mapping suggests that the contacts are concordant with foliation. At one location the contact between the epidosites and the hornblendites can be seen to be parallel to foliation and rather sharp.

Petrology

The petrographic descriptions that follow are based on the examination, both in hand sample and thin section, of over

two hundred rocks collected from the Carroll Knob Complex by the author and 23 thin sections which were made available to the author by R. D. Hatcher. For purposes of discussion the rocks are divided as outlined above. The term amphibolite is used here to mean the dominant rocks of the complex, which consist mostly of hornblende and plagioclase. Other rocks which are strictly speaking amphibolites but are clearly altered metagabbros and pyroxenites and the hornblendites and epidosites are discussed under those headings. All modal proportions given are visual estimates rather than point counts.

Amphibolites

In hand sample the amphibolites are black or black and white banded (cm scale), with bands defined by modal variations in plagioclase. They are generally medium- to coarse- grained and moderately to strongly foliated, although some samples suggest relict gabbroic texture. Mineral assemblages observed in amphibolites that have been collected from the complex are:

1) hornblende + plagioclase + quartz,
2) hornblende + plagioclase + quartz + garnet,
3) hornblende + plagioclase + quartz + biotite ± chlorite ± epidote,
4) hornblende + plagioclase + quartz + clinopyroxene,

5) hornblende + plagioclase + quartz + clinopyroxene + garnet, and

6) hornblende + plagioclase + quartz + garnet + staurolite + anthophyllite.

Assemblages 1 and 2 are by far the most common of the amphibolites, and their abundances appear to be approximately equal. These two assemblages also have similar modal variations, accessory and secondary minerals and textures, and they are, therefore, described together here. The microscopic textures of assemblage 1 and assemblage 2 amphibolites are quite variable, sometimes on the scale of a thin section. However, most samples can be classified as belonging to one of three textural types which are principally defined by the habit of hornblende. In type A textures, hornblende occurs primarily as coarse to very coarse, columnar grains which are interpreted as pseudomorphs of clinopyroxene. Type B textures are characterized by aggregates of recrystallized, medium to coarse, subpolygonal hornblende grains producing an overall texture similar to that of replaced metagabbros described later. The hornblende grains in type C textures are strongly deformed, often with ragged edges, and their elongation defines foliation. Hornblende in all types is pleochroic, generally light to olive green. Modal hornblende varies from about 20% to 70%.

Plagioclase occurs in habits similar to those found in hornblende and in modal proportions complementary to those of

hornblende. Coarse plagioclase in some samples strongly suggests relict igneous laths. Plagioclase is often replaced by epidote, and the epidote is often strongly zoned. In some samples epidote, which rims plagioclase, appears as a symplectite with vermicular quartz inclusions. Similar textures have been reported by McElhaney and McSween (1983) in Chunky Gal Mountain amphibolites and Kittelson (1988) in isolated amphibolites occurring in the metasediments north of Carroll Knob.

In the garnet-bearing amphibolites, garnet occurs in two distinct textural types, sometimes within the same thin section. In one type the garnet is in fine - to - coarse, anhedral - to - subhedral grains, and in the other type it occurs as reaction rims between plagioclase and hornblende. The grain-type garnet is sometimes zoned and sometimes not. Modal garnet is less than 10%.

Quartz is anhedral and usually comprises less than 10% of the rock. In addition to epidote, chlorite is a common secondary mineral, and secondary biotite sometimes occurs. Scapolite, apparently replacing plagioclase, was observed in several rocks from the northern half of the complex. Thin section-scale fractures are usually filled with quartz and, less commonly, with calcite. Accessory minerals commonly include rutile and apatite and, occasionally, titanite and zircon. The opaque suite consists of some combination of pyrrhotite, pyrite, chalcopyrite, ilmenite and magnetite.

Rutile and ilmenite are sometimes in a replacement reaction relationship.

Assemblage 3 consists of several amphibolite samples that differ from those described above primarily in that biotite appears to be in equilibrium with hornblende and plagioclase. The biotite in these samples is strongly pleochroic (yellow to green) and occurs in fine to medium plates that, in most cases, are unoriented with respect to foliation. Chlorite and epidote are common in these rocks, but it is not always possible to determine if they are part of an equilibrium assemblage or are secondary. Most of these samples have opaque suites composed primarily of iron oxides rather than sulfides. Biotite-bearing amphibolites are usually found near contacts with the metasediments. This distribution, together with the unoriented biotite and the prevalence of oxide opaque suites, suggests that these rocks have undergone late-stage metasomatism and retrogression.

Based on only a few samples, the characteristics of assemblages 4 and 5 appear also to be similar to assemblages 1 and 2, except that they contain clinopyroxene. In one sample the clinopyroxene appears to be a relict igneous phase. It is neutral in color, columnar, deformed, and partly replaced by hornblende. In all other samples the clinopyroxene is interpreted to be metamorphic. It is medium- to coarse-grained, strongly pleochroic (pale green to dark green), and partly replaced by a blue-green hornblende.

Amphibolites containing this distinctive green clinopyroxene are found at three locations in the northern part of the complex. These clinopyroxenes are optically very similar to metamorphic clinopyroxenes observed by Kittelson (1988) in isolated amphibolites from north of the Carroll Knob Complex.

Assemblage 6 is represented by only one sample collected from the southeastern portion of the complex. This sample does not appear to be in equilibrium: there are two generations of garnet and the staurolite, which is fine- to medium-grained and anhedral, is apparently resorbed. Assemblages like assemblage 6 were observed at the Laurel Creek Complex about 30 km southeast of Carroll Knob by Helms et al. (1987), who attributed them to metamorphism under high pressure.

Metagabbros and Pyroxenites

The term metagabbro includes a spectrum of rocks that vary widely in mineralogy and texture but which can be related by the progressive replacement of pyroxene and plagioclase by amphiboles and clinozoisite, respectively. A few samples retain many of their primary features, including relict igneous textures. In most of the metagabbros, however, the primary minerals have been largely or completely replaced, and most of the original texture has been obliterated. In hand sample the least replaced metagabbros are coarse- to very coarse-grained, equigranular rocks with a bluish tint from the

pyroxene. The metagabbros which have undergone extensive replacement are coarse- to very coarse-grained, moderately foliated and green in color. Preferential weathering of plagioclase gives these rocks a distinctive rough surface.

The least replaced metagabbros have relict heteradcumulate or adcumulate textures. The primary mineral assemblage is pyroxene + plagioclase. Modal pyroxene is variable, ranging from about 25% to 80%. The pyroxene is either augite alone or augite coexisting with bronzite. Two-pyroxene thermometry confirms that the pyroxenes are igneous in origin (Appendix A). Both types of pyroxene grains are coarse to very coarse, equigranular and anhedral. The augite is colorless or neutral in plain light. The bronzite is strongly pleochroic from pink to neutral. Both pyroxenes commonly have two or more sets of very fine (less than 5 microns) exsolution lamellae. Optically these lamellae appear to be clinopyroxene hosted in the bronzite and orthopyroxene hosted in the augite. In addition, both pyroxenes often contain even finer lamellae of magnetite or ilmenite oriented along one or two cleavage directions. Augite occasionally contains fine, globular grains of bronzite which may be either inclusions or exsolution blebs. Both pyroxenes are sometimes strongly kinked.

Plagioclase sometimes appears as very coarse laths, which appear to be relict igneous forms, but is more typically partially or completely recrystallized into aggregates of

medium to coarse, subpolygonal grains. It is almost always twinned and sometimes zoned. A few of the laths seen in fresher samples are kinked.

The pyroxenes are replaced in varying degrees by pale-green calcic amphibole and colorless cummingtonite. Incipient pyroxene replacement is characterized by aggregates of fine, subpolygonal amphibole grains rimming pyroxene grains. In rocks in which pyroxene has been mostly or completely replaced, the amphiboles commonly consist of aggregates of medium to coarse, subpolygonal grains. Clinozoisite commonly replaces plagioclase, occurring as rims, subpolygonal grains, often with plagioclase cores, or sometimes as well developed euhedral grains in rocks in which replacement is essentially complete. It is often strongly zoned.

Metagabbros in which extensive replacement of pyroxene and sometimes plagioclase has occurred are essentially amphibolites consisting of the assemblage actinolite $\pm$ cummingtonite + plagioclase $\pm$ quartz or actinolite $\pm$ cummingtonite + clinozoisite $\pm$ quartz. Quartz occurs only rarely and is always less than 1%. These rocks have overall polygonal or subpolygonal textures, although they are moderately foliated with foliation defined by both elongate subpolygonal amphibole grains or elongate aggregates of subpolygonal amphibole grains.

A few samples, spatially associated with the metagabbros, are banded parallel to foliation on a scale of 1 to 5 cm. The

banding is defined by chlorite-, actinolite- and cummingtonite-rich regions versus clinozoisite-rich regions. Chlorite is the dominant mineral in the mafic sections and sometimes defines a strong foliation. Relict pyroxene and amphibole occur in the mafic areas. Clinozoisite occurs as very coarse, subhedral to euhedral grains which sometimes have plagioclase cores. They are not oriented with respect to the foliation. These rocks are interpreted to be layered metagabbros which have undergone late-stage replacement.

Other secondary minerals occurring in minor amounts in the metagabbros include calcite, scapolite and talc. Zircon and rutile are common accessory minerals. Opaque minerals include pyrite, chalcopyrite, pyrrhotite, ilmenite and magnetite.

The term pyroxenite also refers to rocks which include a range of textural and mineralogical variations primarily due to the replacement of pyroxene by amphiboles. In hand sample the least replaced pyroxenites are coarse- to very coarse-grained, granular rocks which are bluish in color. Rocks in which the pyroxene has been extensively replaced are fine- to coarse-grained, matted or strongly foliated and are usually blue or green in color.

The least replaced pyroxenites have adcumulate textures and consist almost entirely of coarse to very coarse, equant, anhedral augite. Minor bronzite occurs in one sample, in which it is both included in and intergranular to the augite.

Augite grains typically contain two or more sets of fine (less than 5 microns) exsolution lamellae and are sometime kinked. The compositions of the pyroxenes in the pyroxenites are the same as those of the metagabbros (Appendix A).

The pyroxene is replaced to varying degrees by some combination of actinolite, cummingtonite, orthoamphibole, talc and chlorite. Modal proportions of these minerals are variable but in most samples actinolite and cummingtonite are the dominant minerals and orthoamphibole, chlorite and talc are minor. Amphibole grain size and habit vary from fine and matted to very coarse and bladed. Talc and chlorite are fine - to - medium grained and usually anhedral. It is not possible to determine if these minerals form an assemblage with the amphiboles or are replacing them. Actinolite is always zoned with green cores and paler rims. Rocks in which replacement of pyroxene is essentially complete occasionally retain pyroxenite texture but more commonly are matted or strongly foliated.

Chlorite is the dominant mineral in a few samples, occurring with talc, calcic amphibole or orthoamphibole. In these rocks chlorite is coarse- to very coarse-grained, subhedral to euhedral and defines a strong foliation. Relict clinopyroxene appears in one sample. These chlorite schists are similar to the chlorite-bearing bands in the metagabbros which were described earlier. Both occurrences are ascribed to late-stage replacement of pyroxene-rich rocks or bands.

Epidosites and Hornblendites

The epidosites are distinguished by their high modal epidote, usually in excess of 70%, and a distinctive blue-green hornblende. In hand sample these rocks are green in color and have a coarse-grained granular appearance, although there are strong partings parallel to the long axes of the epidote grains. The common major mineral assemblage is epidote + hornblende + quartz.

The epidote is coarse- to very coarse-grained, subhedral to euhedral, usually strongly zoned and sometimes kinked. The grains are oriented with their long axes in a single plane. Epidote grains sometimes have plagioclase cores, indicating that the epidote replaces plagioclase. Hornblende is strongly pleochroic, green to blue-green. It occurs either as medium to coarse, columnar grains, very reminiscent of pyroxene, or in anhedral grains interstitial to epidote. In one sample a pleochroic, neutral to pale green clinopyroxene appears interstitial to the epidote grains. Both columnar and interstitial hornblende are interpreted as replacements of clinopyroxene.

The most common accessory mineral is titanite, but apatite and rutile also occur in some samples. Secondary minerals include chlorite and minor biotite and calcite. Only two polished sections were made of this lithology. The opaque phases observed in those two sections were ilmenite and magnetite.

The epidosites and the hornblendites appear to form a bimodal association, with most epidosites having modal hornblende of 30% or less, and most hornblendites having modal hornblende in excess of 90%. The hornblende of the hornblendites is coarse- to very coarse-grained, columnar and generally blue-green in color but sometimes zoned with brownish cores. Modal plagioclase and epidote are less than 10%, and modal quartz is less than 1%.

Rutile is the most common accessory mineral, but titanite also occurs. Chlorite, biotite and, occasionally, calcite occur as secondary minerals. The opaque suite usually consists of ilmenite, magnetite and hematite. The hematite is derived from the alteration of magnetite. Pyrite occurs as cores to magnetite grains in one sample.

Chunky Gal Mountain Complex

Field Relations

The Chunky Gal Mountain Complex is located about 10 km west-southwest of the Carroll Knob Complex (Rainbow Springs Quadrangle, North Carolina, 7.5′ series, 159-SE and Shooting Creek Quadrangle, North Carolina, 7.5′ series, 159-SW). The complex was mapped and studied by McElhaney (1981) and most recently described in McElhaney and McSween (1983), from which most of the following description is taken. The complex covers an area of approximately 25 km^2 and consists of an

irregularly shaped body of amphibolites which surrounds a smaller body of dunite, sometimes referred to as the Buck Creek ultramafic body, and small lenses of troctolite, which are spatially associated with dunite (Figure 3). The complex lies within garnet muscovite schist and biotite gneiss of the Tallulah Falls Formation and Coweeta Group (Hatcher and Butler, 1979). At least part of the contact between the amphibolites of the complex and the surrounding gneiss is interpreted as a major thrust fault, the Chunky Gal Mountain Thrust, based on a change in the orientation of foliation at the contact and mylonitization in the amphibolites and the metasedimentary host rocks near the contact (Hatcher, 1978; Hatcher and Butler, 1979). The contact between the ultramafic rocks and the amphibolites is concordant with the foliation in the amphibolites, and no thermal aureole has been observed.

The dominant S surface in the amphibolites is the northeast-southwest trending S_2 foliation associated with the F_2 fold generation. F_3 folds and local F_4 crenulations are also observed. Petrofabric studies have indicated that the dominant mineral fabric in the dunites is discordant to S_2 foliation; however, partings in the dunite are parallel to S_2 foliation in the amphibolites, implying that the dunites and amphibolites were in contact by the time of F_2 deformation. Metamorphic grade in the area is upper amphibolite facies.

Figure 3. Generalized lithologic map of the Chunky Gal Mountain Complex and the Kimsey Bald amphibolite body. Base maps from McElhaney and McSween (1983) and Eggers (1983). See Figure 1 for regional location. Small, lower case letters indicate XRF sample locations and are keyed to data presented in Appendix B.

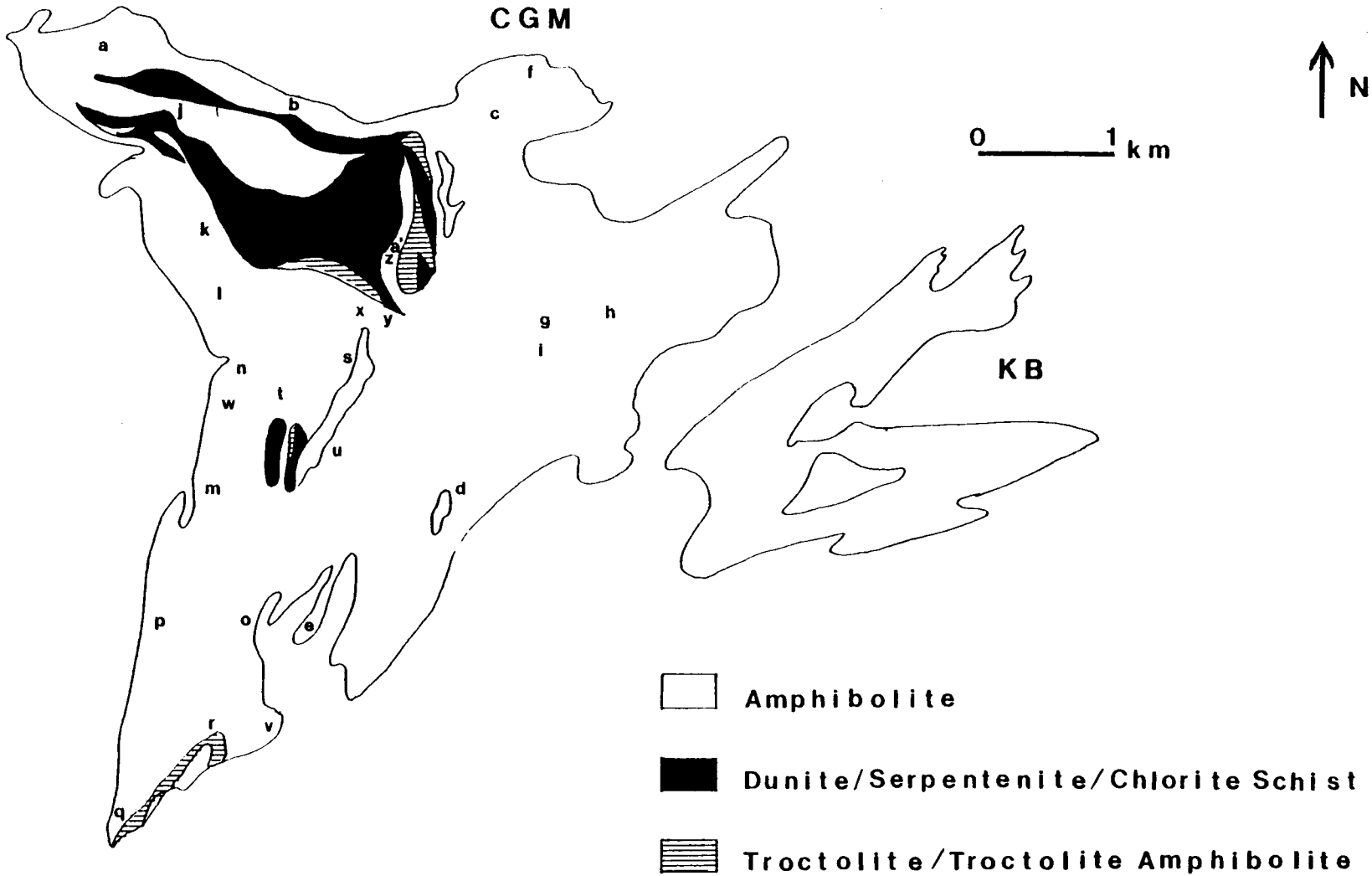
CGM
KB
N
0 1 km
a
b
c
d
e
f
g
h
i
j
k
l
m
n
o
p
q
r
s
t
u
v
w
x
y
z
a'
Amphibolite
Dunite/Serpentenite/Chlorite Schist
Troctolite/Troctolite Amphibolite

Petrology

Amphibolites

McElhaney (1981) and McElhaney and McSween (1983) divided the Chunky Gal Mountain amphibolites into two broad types: Type I, found in the eastern portion of the complex, and Type II, found in the western part of the complex. Equilibrium assemblages in Type I amphibolites are hornblende + plagioclase and hornblende + plagioclase + clinopyroxene. In Type II amphibolites they are hornblende + plagioclase, hornblende + plagioclase + epidote, and hornblende + plagioclase + garnet. The hornblendes in both amphibolite types are tschermakitic, although the hornblendes of Type I amphibolites have distinctly lower FeO/MgO and higher TiO_2 than those of Type II amphibolites. Plagioclase compositions for Type I amphibolites cluster around An_{52}, and for Type II amphibolites they range from about An_{20} to An_{30}. McElhaney and McSween (1983) suggested that observed differences in amphibolite assemblages, described below, represent increasing metamorphic grade to the northeast. However, Lacazette (1986) mapped a series of sheer zones in the amphibolites of the complex and suggested that lithologies of different grade could be separated by a fault.

Type I amphibolites are medium- to coarse-grained with granoblastic textures. Hornblende and plagioclase form homogeneous diablastic intergrowths, but hornblende prisms

define a mineral lineation that is parallel to S_2. Hornblende is pleochroic from brown or reddish-brown to greenish-brown and does not contain inclusions. Plagioclase grains are generally equant, unzoned or slightly zoned, and often twinned. Many samples show prograde breakdown of plagioclase to scapolite. Accessory minerals include quartz, scapolite, calcite, magnetite, ilmenite, hematite, rutile, pyrite and pyrrhotite. Ilmenite, hematite and magnetite are the most common opaque phases, and pyrite and pyrrhotite are rare.

Type II amphibolites have well-developed S_2 foliation, commonly have two or more deformational fabrics and are texturally quite variable. They vary from fine- to coarse-grained and are typically inequigranular. Hornblende is often poikiloblastic, with inclusions of quartz, epidote and plagioclase. It is pleochroic either from brown to yellow-green or from dark green to bluish-green. Plagioclase occurs in spherical, low surface-energy shapes. Garnet porphyroblasts are commonly rolled and contain inclusions of hornblende and epidote. Epidote occurs as both a primary and as a retrograde mineral. Euhedral titanite is an abundant accessory mineral.

Retrograde effects are common in both types of amphibolites. Retrograde minerals include amphiboles, chlorite, epidote, clinozoisite and sericite.

Dunites and Troctolites

Unaltered dunites are the most abundant ultramafic lithology at Chunky Gal Mountain. They are composed primarily of fine- to medium-grained, anhedral olivine. The dunites show granulation textures, patchwork extinction, deformation bands and translation lamellae. Accessory minerals include magnetite, minor chromite, diopsidic augites, hornblende and minor sulfides. The dunite was clearly not produced by dehydration of serpentinites during the major prograde metamorphic event because the mineral fabric in the dunites is discordant to regional foliation. Principal alteration products are talc, serpentinite, tremolitic amphibolite and chlorite.

Troctolite consists of varying amounts of olivine and plagioclase with accessory salitic pyroxenes, chromite and magnetite. It is characterized by a well-developed corona texture. The troctolite grades into anorthositic rocks. Troctolite is replaced by a troctolite amphibolite, which contains relict corona texture and a fabric which parallels S_2. Compositions of olivines in the dunites and the troctolites are similar, with an average composition of Fo_{89-90}. The plagioclase composition in the troctolites is An_{94}.

Kimsey Bald Amphibolites

Field Relations

The Kimsey Bald amphibolite body is located immediately east of the Chunky Gal Mountain Complex (Rainbow Springs Quadrangle, North Carolina, 7.5′, 159-SE). The body was mapped and studied by Eggers (1983), and the descriptions that follow are based entirely on her work. The body is very irregularly shaped and covers and area of about 5 km^2 (Figure 3). Eggers identified two separate rock units within the complex: amphibolite and garnet amphibolite. Both amphibolites are in contact with quartzofeldspathic or biotite gneiss. Based on the observation of decreasing grain size in the amphibolites toward contacts and textures in amphibolites along the contact suggestive of mylonites, Eggers interpreted the amphibolite/metasediment contact as a fault.

F_2 is the dominant fold generation in the Kimsey Bald area and the trend of foliation (S_2) is predominantly northeast-southwest. A later generation of folds assigned to F_3 and crenulations assigned to F_4 were also observed in the study area. Compositional layering is parallel to foliation.

Peak metamorphism appears to have been amphibolite facies. Eggers did not report the presence of pyroxene in the amphibolites. The presence of chlorite in some garnet amphibolites may indicate a later retrograde metamorphic event.

Petrology

Except for the presence of garnet, the amphibolites and the garnet amphibolites are petrographically similar and are described together here. Both amphibolites are medium- to coarse-grained, with textures that range from massive "salt and pepper" to layered gneissic (mm scale). The major assemblage is hornblende + plagioclase, with accessory garnet (in the garnet amphibolites), epidote, opaque oxides, chlorite, clinozoisite and titanite. The amphibole is reported to be hastingsite and occurs as short, stubby, subhedral to euhedral crystals oriented parallel to S_2. It is pleochroic, yellowish brown to brown, dark green and bluish green. Modal hornblende varies from about 50% to 70%.

Plagioclase occurs as subhedral grains, which vary in composition from An_{40} to An_{60}, based on the Michel-Levy method. Epidote usually comprises less than 8% of the rock but is much more abundant in some samples found near contacts with the metasedimentary host rocks. The garnet amphibolites contain very coarse (up to 5 cm), euhedral garnets. The garnets are unzoned, contain few inclusions and have well-developed hornblende rims.

Lake Chatuge Complex

Field Relations

Rocks of the Lake Chatuge Complex outcrop in two main sections located around the periphery of Lake Chatuge and on the flanks of Brasstown Bald about 10 to 20 km southwest of the Chunky Gal Mountain Complex (Shooting Creek Quadrangle, North Carolina, 7.5′ series, 159-SW; Hiawassee Quadrangle, Georgia-North Carolina, 7.5′ series, 151-NE; Macedonia Quadrangle, Georgia-North Carolina, 7.5′ series, 160-NW; Jacks Gap Quadrangle, Georgia, 7.5′ series). Figure 4 shows the northern portion of the complex. Total outcrop area is of the order of 10's of km^2. Descriptions of field relations and petrology for the complex can be found in Hartley (1973) and Hartley and Penley (1974). The following descriptions draw heavily from those works but include some observations made during the collection of samples for this study. Hartley (1973) reported dunite, troctolite, olivine gabbro, orthoamphibolite, mafic and metamafic veins and pods, and garnet-pyroxene gneiss as the main rock units present at the complex. Minor wehrlite, pyroxenite and two-pyroxene gabbro float were also reported. He interpreted the amphibolites as metamorphosed equivalents of parts of the relict mafic units, based on gradational contacts, textures and isotope data. Relict igneous textures were also observed in amphibolites collected for this study.

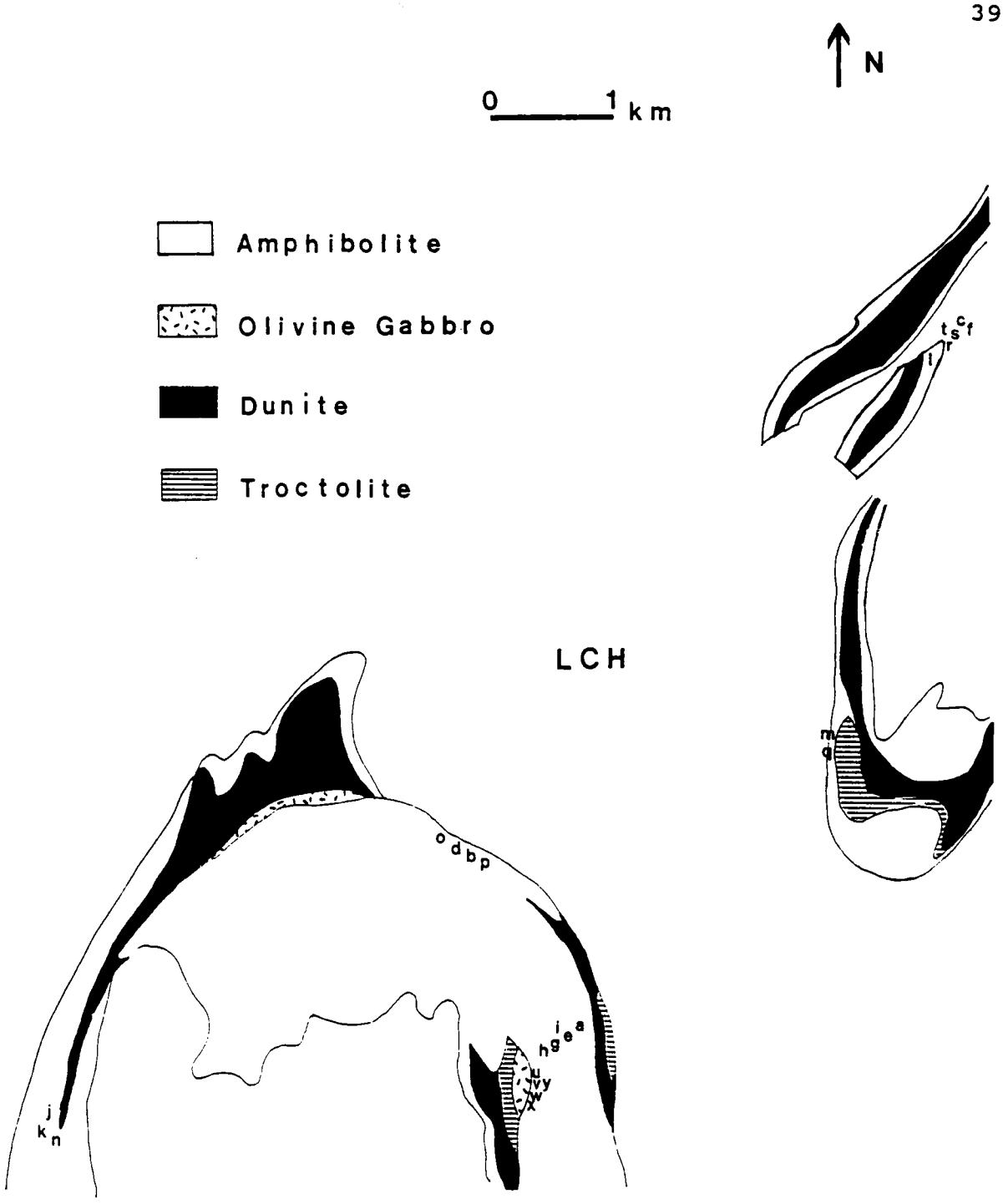

Figure 4. Generalized lithologic map of the northern portion of the Lake Chatuge Complex. Base map from Hartley and Penley (1974). See Figure 1 for regional location. Small, lower case letters indicate XRF sample locations and are keyed to data presented in Appendix B.

The mafic and ultramafic rocks of the complex occur between two main metasedimentary units: garnet-mica schist and biotite gneiss. As discussed earlier, the contact has been described by different authors as intrusive or a fault contact. Metamorphic grade in the area is kyanite to sillimanite. Foliation in the rocks of the complex is concordant with S_2 in the metasedimentary host rocks.

Petrology

Dunite consisting primarily of olivine of composition Fo_{90} is the dominant ultramafic unit. Partial alteration to serpentine and chloritization are common. Other alteration products such as anthophyllite and talc occur locally. Coronite troctolite is often associated with the dunite, and rhythmically banded coronite troctolite occurs locally as lenses within the dunite. These rocks are similar to troctolites observed at the Chunky Gal Mountain Complex (McElhaney and McSween, 1983) and consist of olivine and plagioclase with coronas composed of concentric layers of pyroxene and amphibole-spinel between the olivine and plagioclase grains. The olivine gabbro is similar to the troctolite except that it contains over 10% primary clinopyroxene. Hartley and Penley (1974) reported the composition of the olivine as Fo_{90} and that of the plagioclase as An_{68} to An_{83} in both the troctolites and the gabbros. Anorthositic olivine gabbro is locally common. Both the

troctolites and the gabbros grade into the surrounding amphibolites. Chloritization is locally common in both lithologies.

Amphibolites make up a large proportion of the rocks of the Lake Chatuge Complex. They generally surround the relict igneous rocks and occur in contact with the metasedimentary host rocks. Hartley and Penley (1974) reported that the amphibolites consist mainly of hornblende, plagioclase and clinozoisite, with corundum locally present. Four out of five thin sections of amphibolites examined in the present study consist of bright-green hornblende, plagioclase and epidote with accessory apatite and titanite. Epidote forms discrete grains. Textures vary widely, but some suggest relict adcumulate textures. The fifth amphibolite consists of pale-green amphibole, plagioclase and clinozoisite with accessory sphene. The clinozoisite has plagioclase cores and appears to be replacing it.

A particularly interesting lithology found at the complex is a garnet-pyroxene-plagioclase-amphibole gneiss, sometimes referred to as ecologite or pyroxene granulite. This lithology was first examined by Dallmeyer (1974) and more recently by Means (1988). Although their interpretations differed in detail, both of these authors concluded from the mineral chemistry of coexisting phases that the garnet and clinopyroxene of these rocks first equilibrated at temperature and pressure conditions characteristic of the upper mantle,

and that the rocks later cooled under lower pressure conditions. Dallmeyer postulated that the protoliths of these rocks were clinopyroxenites, and Means suggested they were olivine gabbros. Bulk-rock compositions presented by Dallmeyer are unlike those of pyroxenites but are similar to compositions for Lake Chatuge Complex amphibolites (presented in the next chapter), suggesting that a gabbro protolith is more likely.

Two-pyroxene gabbro and clinopyroxene gabbro float were found in rocks collected for this study; there is only one sample each of these lithologies. The two-pyroxene gabbro consists of slightly pleochroic (neutral to pink) orthopyroxene, augite and plagioclase. The pyroxenes are very coarse and columnar in habit. Plagioclase is coarse to very coarse, occurring as both relict laths and recrystallized masses. Both pyroxene and plagioclase grains are deformed. The clinopyroxene gabbro consists of coarse-grained, neutral, anhedral augite and coarse, anhedral, partially recrystallized plagioclase, with secondary amphibole. Opaque phases exceed 5% of this rock and occur as discrete grains within amphiboles.

Isolated Amphibolites

Field Relations

The rocks classified as isolated amphibolites are from locations in seven quadrangles covering most of the study area (Corbin Knob Quadrangle, North Carolina, 7.5′ series, 167-NE; Franklin Quadrangle, North Carolina, 7.5′ series, 167-NW; Prentiss Quadrangle, North Carolina, 7.5′ series, 167-SW; Rainbow Springs Quadrangle, North Carolina, 7.5′ series, 159-SE; Wayah Bald Quadrangle, North Carolina, 7.5′ series, 159-NE; Shooting Creek Quadrangle, North Carolina, 7.5′ series, 159-SW; Hightower Bald Quadrangle, Georgia-North Carolina, 7.5′ series, 160-NE). Several of the samples from the Franklin and Corbin Knob quadrangles were collected by R. Kittelson, and the samples from the Hightower Bald quadrangle were collected by J. Hopson. The rest of the samples were collected by the author using outcrop maps which were made available by R. D. Hatcher. Sample locations are shown in Figure 1.

Although no effort was made to map the isolated amphibolite occurrences, some sense of their general size and nature was obtained during sample collection. Many of the amphibolites appear to belong to reasonably large bodies or pods (1 to several km^2). For example, an unmapped amphibolite body about the size of Kimsey Bald appears exists in the central part of the Franklin Quadrangle, and the amphibolites

in the southeastern part of Shooting Creek quadrangle belong to a body with an outcrop area of about 1 to 2 km^2. Ultramafic rocks, represented by amphibole-talc-chlorite schists, are associated with the Shooting Creek body. Other occurrences, e.g. on Wayah Bald and in the northern portion of the Prentiss Quadrangle, appear to be lenses (about 100 - 1000 feet thick) of amphibolite intercalated with the metasediments. Foliation in the amphibolites is concordant with that in the metasediments. Only a few amphibolite/ metasediment contacts were observed, and these were all apparently concordant with foliation.

Petrology

As is to be expected for rocks collected over a wide area of varying metamorphic grade, the petrologic characteristics of the isolated amphibolites are quite variable. Kittelson (1988) described thin sections of many samples from Franklin and Corbin Knob quadrangles in detail but reported no relict mineralogy or texture. Hopson (1990) reported that many of the samples for the Hightower Bald quadrangle are coarse grained with textures suggesting gabbroic protoliths. Representative thin sections of samples from all quadrangles except Corbin Knob were examined by the author. No definite relict mineralogy was seen in these samples, but many of the rocks have textures reminiscent of heteradcumulates.

The amphibolites consist of hornblende + plagioclase ± clinopyroxene ± garnet ± quartz. The clinopyroxene always appears to be metamorphic. Orthopyroxene was observed in one sample (RBS6) from the northeastern portion of the Rainbow Springs quadrangle, and it too appears to be metamorphic. Epidote and chlorite sometimes occur as secondary minerals. Titanite is observed in some sections.

CHAPTER III

GEOCHEMISTRY

Introduction

The primary purposes of this chapter are to present new X-ray fluorescence (XRF) data for the suites of rocks described in Chapter II and to discuss some preliminary conclusions regarding the natures of the suites and the relationships among them. This introductory section describes analytical procedures and sample populations and discusses previous bulk chemical studies for rocks from Carroll Knob, Chunky Gal Mountain, Lake Chatuge and Kimsey Bald. This section is followed by summaries and discussions of the major-, minor-, and trace-element chemistry of the five suites considered in this study.

The XRF data for the Carroll Knob, Lake Chatuge, the isolated amphibolite, and Chunky Gal Mountain suites were obtained on an EG&G ORTEC model EEDS-II energy dispersive XRF spectrometer in the University of Tennessee Knoxville (UTK) Department of Geological Sciences. Samples for analysis were pressed-powder pellets prepared according to standard procedures. The samples were analyzed using several USGS and South African standards and the IGROCK protocol, which sets appropriate run conditions and inter-element corrections.

Sample preparation, standards and calibration errors are discussed in more detail in Appendix B. J. Hopson supplied analyses for several isolated amphibolites from the Hightower Bald quadrangle; these analyses were performed on the same instrument with the same protocol as the other analyses. The data cited for Kimsey Bald are from Eggers (1983).

A total of 45 samples from the Carroll Knob Complex were analyzed. These include 9 amphibolites, 15 garnet-amphibolites, 15 metagabbros, 3 pyroxenites and 3 epidosites. Carroll Knob sample locations are indicated on Figure 2, and the data are shown in Appendix B. Twenty seven Chunky Gal Mountain samples were analyzed. Twenty two of these are the same samples analyzed by McElhaney (1981) and include 10 Type I amphibolites and 12 Type II amphibolites. Three additional amphibolites and 2 dunites were also analyzed. Chunky Gal Mountain sample locations are shown on Figure 3, and the data are presented in Appendix B. The isolated amphibolite suite consists of a total of 36 samples, which were collected from 7 quadrangles and include: 1) twenty samples collected in the northeastern part of the study area (Corbin Knob, Franklin, Prentiss and the northeastern part of Rainbow Springs quadrangles), 2) three samples collected from the Wayah Bald quadrangle, 3) eight samples from the Hightower Bald quadrangle, and 4) five samples from the Shooting Creek and southwestern portion of the Rainbow Springs quadrangle (Figure 1). Chemical data are presented in Appendix B. Twenty five

Lake Chatuge Complex samples were analyzed; these include 17 amphibolites, 6 olivine gabbros and 2 gabbros. Figure 4 shows sample locations for the Lake Chatuge rocks, and the chemical data are presented in Appendix B. The Kimsey Bald suite consists of 16 samples of which 7 are amphibolites and 9 are garnet amphibolites. Chemical data for Kimsey Bald are reported in Eggers (1983).

XRF data for Carroll Knob amphibolites and metagabbros have been published previously by Hatcher et al. (1984). The data from their study are consistent, within calibration error, with results obtained in this study for all major, minor and trace elements. These authors attempted to use discriminant diagrams from Pearce and Cann (1973) and Pearce (1976) to assess the original tectonic setting of the Carroll Knob Complex. This approach is problematic for at least two reasons. First, the number of their samples which meet the screening values necessary for plotting on the diagrams is only 6, and the data for these scatter widely. Second, as will be demonstrated in the next two chapters, the approach is overly simplistic for rocks which are likely to have cumulate components, because cumulate processes can significantly alter trace element ratios from magmatic values.

Long (1983) and Eggers (1983) also attempted to infer provenance for the Lake Chatuge Complex and Kimsey Bald amphibolites, respectively, by plotting XRF data directly on discriminant diagrams. Long (1983) presented major- and

minor-element data for seven Lake Chatuge Complex amphibolites and trace-element data for 6 amphibolites; these data are consistent with data for amphibolites obtained in this study. Based primarily on the discriminant diagrams, both Long and Eggers concluded that the rocks they studied are related to island arc settings. Again, it will be shown that this approach is oversimplistic, and the results obtained are misleading.

Twenty two of the samples of Chunky Gal Mountain amphibolites that were analyzed in this study were previously analyzed by McElhaney (1981) on different equipment with a different calibration. There are discrepancies between the values he reported and those measured in this study for several elements. In general McElhaney's data are more scattered, but, except for P_2O_5, elements show approximately the same trends in both data sets. Zr and Nb values in the present data are consistently about 60% and 50%, respectively, lower than McElhaney reported, and TiO_2 and Y are about 10% and 40%, respectively, higher. The most significant difference is in the Zr values; Nb differences are about the same magnitude as the standard error of calibration for this study, and the Y and TiO_2 differences are only slightly larger. P_2O_5 in the present data set shows a range of values and correlates well with Zr, but McElhaney's data are somewhat scattered and uncorrelated with Zr.

The use of standard sample preparation and analytical techniques, little data scatter, and good trace-element correlations, as well as the consistency of the Carroll Knob and Lake Chatuge data from this study with that from Hatcher et al. (1984) and Long (1983), respectively, give confidence in the accuracy of the present data. In any case, the differences in element concentrations between the two data sets are not important for this study, because nearly all arguments and conclusions depend on the nature of data trends rather than exact values, and these trends (except for P_2O_5 and poorer correlations in McElhaney's data) are essentially the same in both data sets.

Based primarily on the chemical data, McElhaney (1981) and McElhaney and McSween (1983) argued that the Chunky Gal Mountain rocks are igneous in origin, probably had cumulate protoliths, and that the trends seen in the data represent magmatic differentiation. In addition, while recognizing potential problems in applying discriminant diagrams to cumulate rocks, they suggested that the protoliths of the amphibolites were of calc-alkaline affinity, based on Pearce and Cann (1973) diagrams. In the next two chapters it will be argued that the Chunky Gal Mountain amphibolites are indeed igneous in origin and do represent cumulate protoliths, but that the trends are produced by a cumulate process rather than magma fractionation, and that this process altered trace

element ratios, making conclusions drawn directly from discriminant diagrams misleading for these rocks.

Major-Element Chemistry

Because they are likely to be mobile under high-grade metamorphic conditions, most major elements cannot be considered reliable process or provenance indicators for the suites of rocks described here. Major elements are, however, worth examining as gross indicators of the probable natures of the protoliths of the suites, magma types to which they are related and possible relationships among suites. In the following paragraphs the major-element data for the five suites of rocks are analyzed using standard igneous ternary and two-element variation diagrams. The data for the Chunky Gal Mountain, isolated amphibolite, Carroll Knob and Lake Chatuge suites are shown on separate diagrams, and the distributions of Eggers (1983) data for the Kimsey Bald amphibolites are indicated on the Chunky Gal Mountain diagrams. The data for all suites were examined to determine if lithologic subgroups or isolated amphibolites collected from different areas were chemically distinguishable. Although the large amount of data to be presented precludes plotting all subgroups separately, significant distinctions will be discussed in the text.

Igneous Protoliths

The field and petrographic data discussed in Chapter II strongly suggest that most of the Chunky Gal Mountain, Carroll Knob and Lake Chatuge suites are of igneous origin. However, the Kimsey Bald amphibolites and the majority of isolated amphibolites are not definitely associated with ultramafic bodies or with rocks having relict igneous textures, and their original natures are less certain. Figures 5a through 5d show the data for each suite plotted on the ternary diagram of Leake (1964), which discriminates para- and ortho-amphibolites. On this diagram amphibolites of igneous origin should follow an essentially vertical trend indicated by the arrow in the figure, and para-amphibolites would be expected to follow a trend at right angles to the orthoamphibolite trend, indicating a mixture of pelitic and carbonate rocks. All the suites show basically vertical trends consistent with igneous protoliths. In addition, many of the samples from all the suites plot outside the dolostone-limestone-shale composition triangle. In the data for the isolated amphibolites and the Carroll Knob amphibolites there is some scatter toward shale compositions; this minor scatter is more likely an indication of element mobility than of a sedimentary component of the protolith.

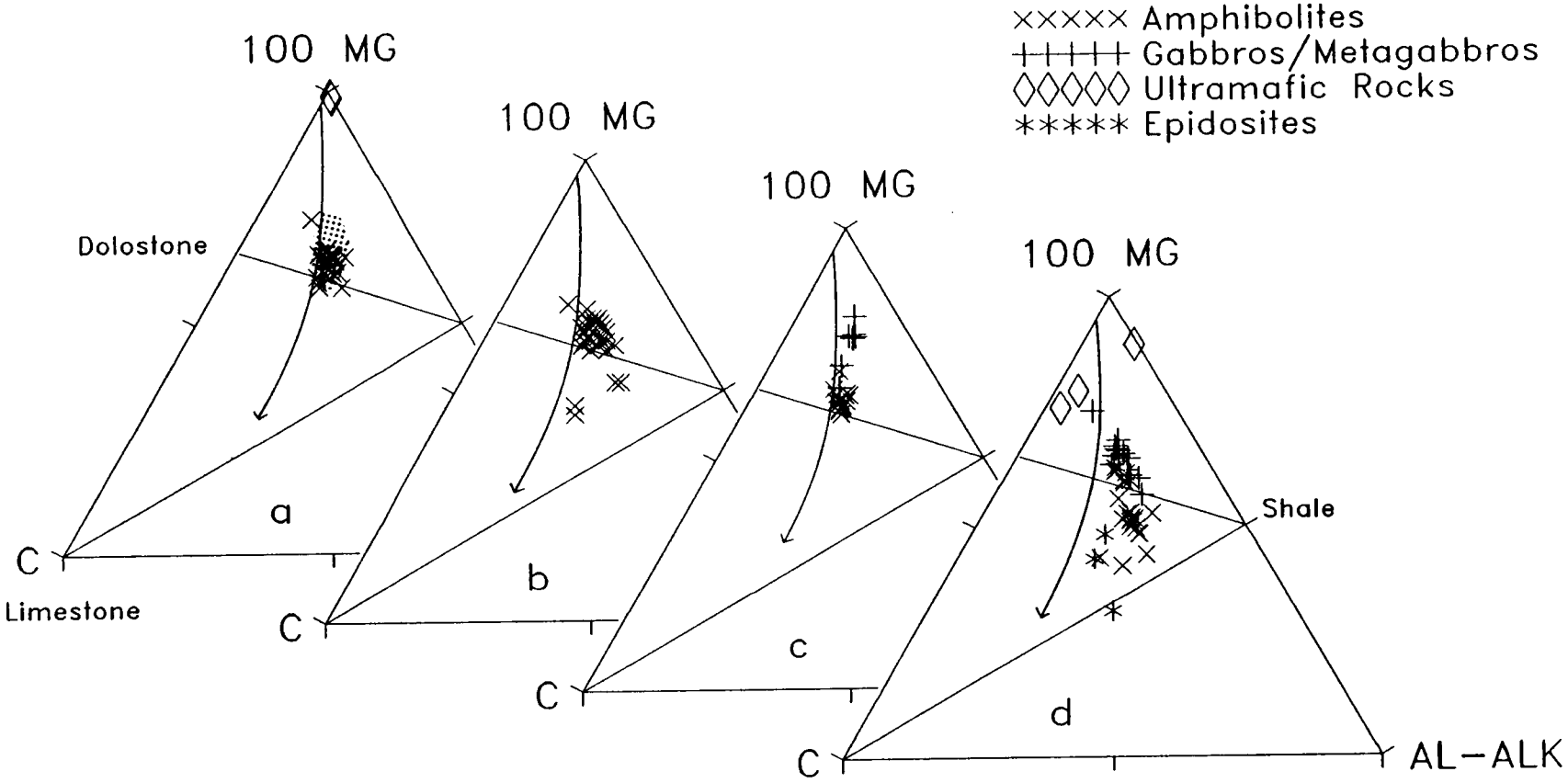

Figure 5. Discriminant diagrams for para- and orthoamphibolites from Leake (1964). MG = MgO/(MgO + FeO + MnO), C = CaO, AL = Al_2O_3, and AlK = $Na_2O + K_2O$, all in wt. %. Arrow follows the approximate trend of the Karoo tholeiites. Lithologic symbols as indicated. (a) Chunky Gal Mountain Complex data and Kimsey Bald amphibolite field (stippled pattern). (b) Isolated amphibolite data. (c) Lake Chatuge Complex data. (d) Carroll Knob Complex data.

AFM Diagrams - Magma Types and Trends

Figures 6a through 6d show the data for the suites plotted on standard igneous AFM diagrams (Irvine and Barager, 1979). Although the possibility of element mobility, especially for alkalis, cannot be ruled out, the data are consistent with all the suites having originated from tholeiitic magmas: although not extensive, there are definite iron-enrichment trends, and there are no indications of calc-alkaline trends. Major-element data for alkaline basalts are normally distinguished from those for tholeiitic basalts on a plot of K_2O+Na_2O versus SiO_2 (Irvine and Baragar, 1979). However, this diagram is not likely to give a reliable indication of magma type for the rocks of this study because these elements are likely to have been mobile and because their concentrations are strongly affected by cumulate processes. Consequently, the possibility of alkaline affinity cannot be ruled out on the basis of major-element data alone.

The majority of the Chunky Gal Mountain, Kimsey Bald and the isolated amphibolite data fall along trends that look somewhat like magma fractionation patterns (Figures 6a and b); the trends show initial iron enrichment followed by an increase in alkalis in the samples with higher FeO/MgO ratios. In contrast to the trends exhibited by the above three suites, the majority of the Carroll Knob samples plot parallel to the FeO-MgO join at low alkali values for all FeO/MgO ratios (Figure 6c). The amphibolites, garnet-amphibolites and

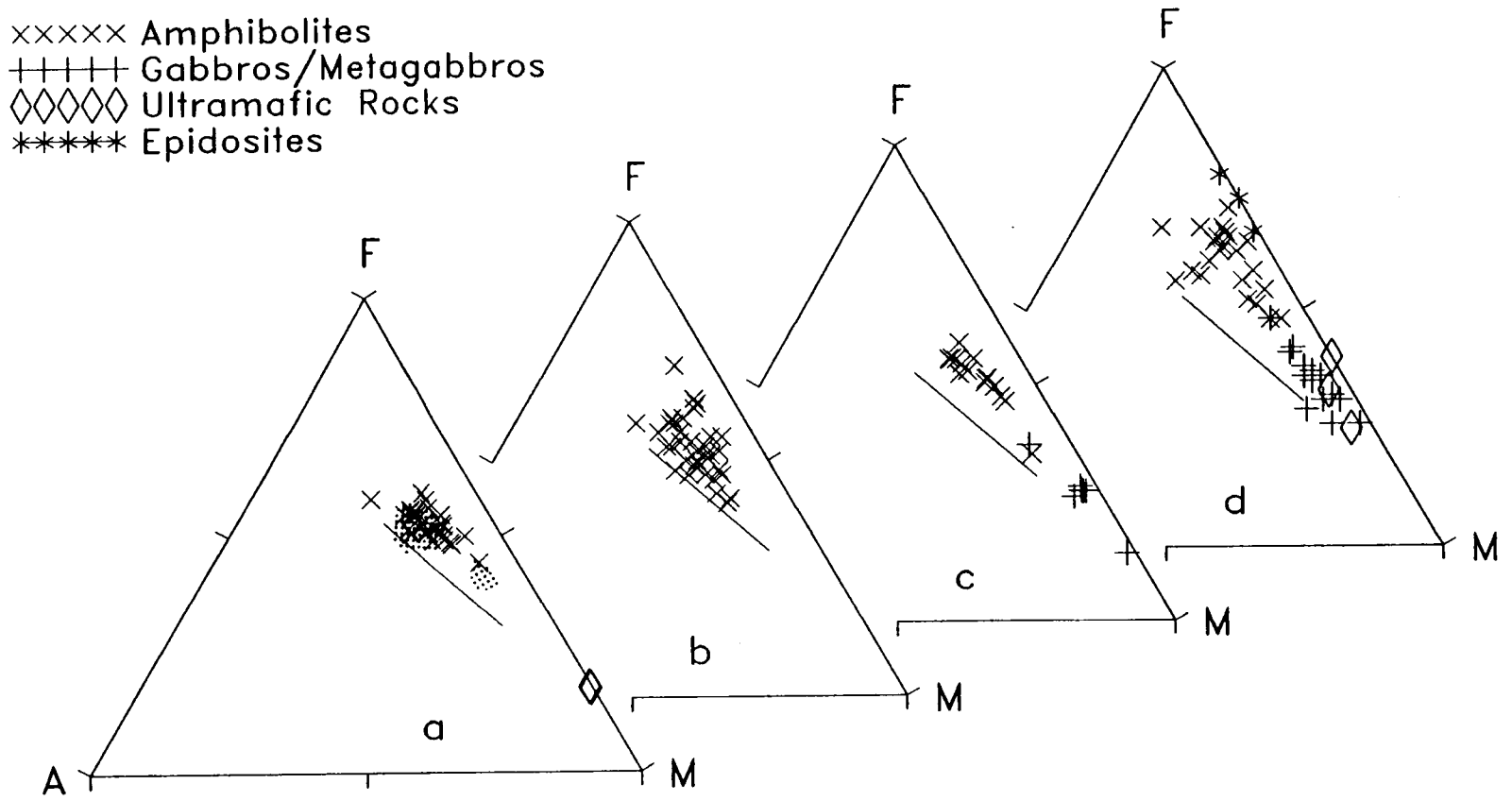

Figure 6. AFM diagrams from Irvine and Baragar (1971). A = $Na_2O + K_2O$, F = FeO + 0.8998 Fe_2O_3 (Fe_2O_3 = 1.5 + TiO_2), and M = MgO, all in wt %. Line separates tholeiitic (above) from calc-alkaline basalts (below). Lithologic symbols as indicated. (a) Chunky Gal Mountain Complex data and Kimsey Bald amphibolite field (stippled pattern). (b) Isolated amphibolite data. (c) Lake Chatuge Complex data. (d) Carroll Knob Complex data.

metagabbros plot in essentially separate fields. Although there is some overlap, the garnet-amphibolites tend to plot at higher FeO/MgO values than the non-garnet-bearing amphibolites, with most of the garnet-amphibolites plotting at unusually high FeO/MgO. A few of the amphibolite analyses extend to relatively high alkali values. The metagabbros plot at low FeO/MgO and low alkali values. The patterns seen in the Carroll Knob data (Figure 6c) are consistent with the FeO/MgO of most of the rocks having been determined primarily by secondary cumulate processes, e.g. crystal sorting, rather than magma fractionation. The compositions of the garnet amphibolites, for example, are most likely influenced by crystal sorting of an Fe-rich phase; further evidence that this is the case is presented in Chapter V. The epidosites plot at high FeO/MgO with very low alkali values; it is unlikely that their compositions result entirely from alteration of the metagabbros because they plot in clearly separate fields on all major- and trace-element diagrams.

The trend of the Lake Chatuge samples (Figure 6d) suggests both cumulate-like and liquid-like components; the former paralleling the FeO-MgO join, and the latter showing some alkali enrichment. The data for olivine gabbros and amphibolites plot in entirely separate fields, indicating that the amphibolites are unlikely to be simply hydrated and metamorphosed olivine gabbros, as suggested by Hartley (1973), but are distinct lithologies; immobile trace-element data

presented later support this distinction. Data for the two-pyroxene gabbro and the clinopyroxene gabbro plot closer to the amphibolite data.

Differentiation Index

Zr is used as a differentiation index in the major-, minor-, and trace-element variation diagrams presented in the following sections because it is highly incompatible and likely to be immobile. Good correlations between other minor and trace elements that are expected to be immobile and Zr for Chunky Gal Mountain and isolated amphibolites (presented later in this chapter) argue that Zr, indeed, has not been mobile in most of the rocks under consideration. Some assimilation and mixing processes can decouple major- and trace-element compositions during differentiation. However, for the suites of this study that show trends, Zr is well correlated with the conventional major-element differentiation index FeO/MgO and, thus, should provide a good differentiation index for major elements as well as trace elements.

Cumulate Components and Two-Element Variation Diagrams

CaO+MgO can be used as a crude screen for cumulate samples among mafic rocks: samples with CaO+MgO above 20 wt% are likely to have had cumulate protoliths (Pearce, 1976). In addition, CaO+MgO should decrease in a regular way with magma fractionation and can be used as an initial indicator of

fractionation processes. Figures 7a through 7d show CaO+MgO plotted against Zr for the suites. In each suite there are samples with CaO+MgO above 20 wt%, indicating the possibility of cumulate components in all the suites. Beyond this fact, three types of patterns are apparent in the data. First, the Chunky Gal Mountain and isolated amphibolite samples show fractionation-like trends with strong horizontal components extending to relatively high values of Zr (Figures 7a and 7b). Second, the Carroll Knob and Lake Chatuge samples show essentially vertical patterns at low Zr that do not look like fractionation trends (Figures 7c and 7d). For both the Carroll Knob and Lake Chatuge suites, however, some samples plot near the Chunky Gal Mountain and isolated amphibolite trends at higher Zr and lower CaO+MgO values. Third, the Kimsey Bald samples plot in a cluster at low Zr near the Chunky Gal Mountain data.

For the Chunky Gal Mountain suite, several samples plot above 20 wt% CaO+MgO and probably represent cumulate protoliths as suggested by McElhaney and McSween (1983). In addition, the Type I and Type II amphibolites classified petrographically by those authors are distinguishable on this diagram, with Type I amphibolites plotting at higher CaO+MgO and lower Zr than most Type II amphibolites. Linear regression of the data gives a correlation coefficient of 0.6, indicating that the data follow a definite fractionation-like

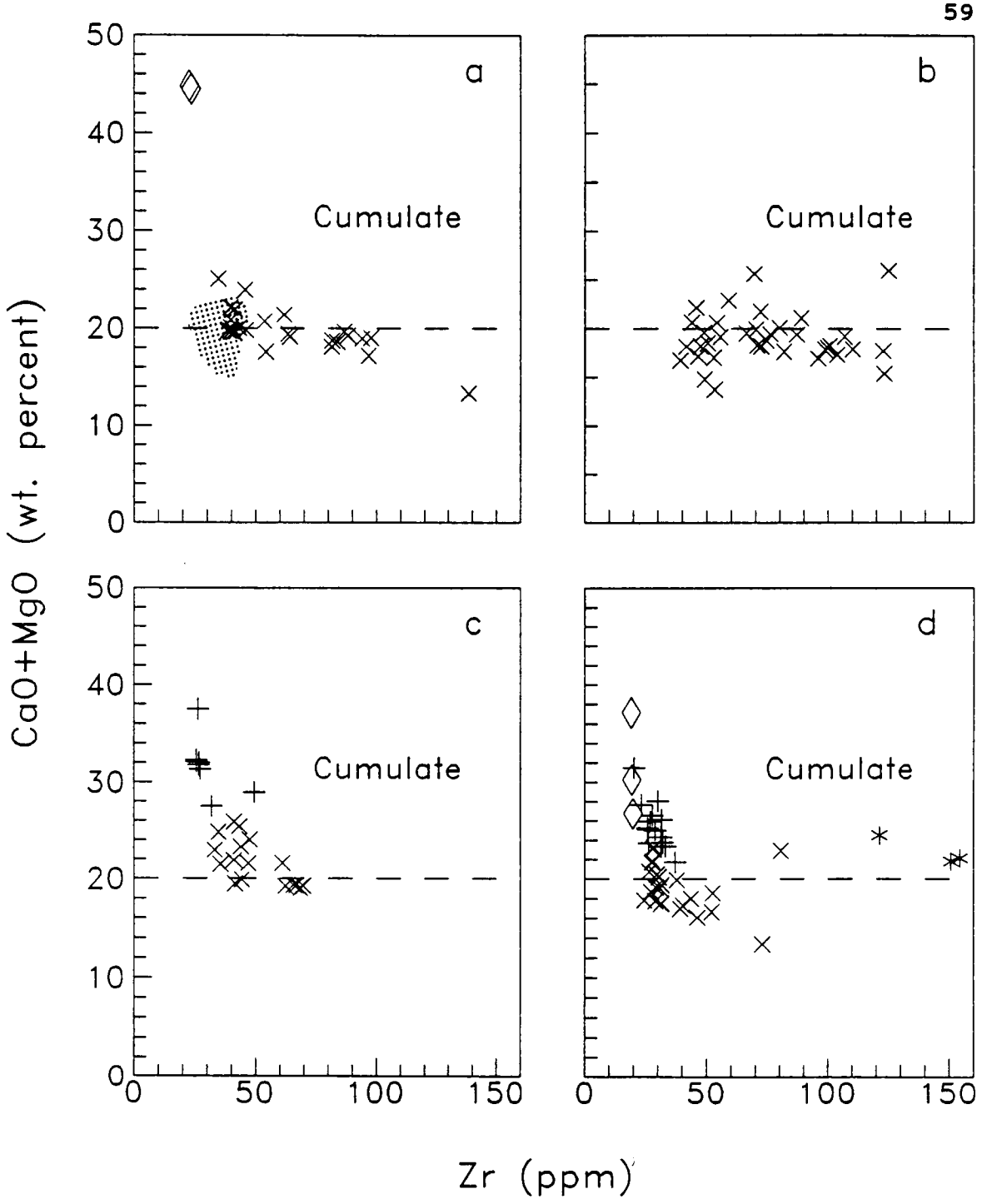

Figure 7. Plots of CaO + MgO (wt. %) versus Zr (ppm). Samples with CaO + MgO above 20% are likely to have cumulate protoliths. Lithologic symbols as in previous figures. (a) Chunky Gal Mountain Complex data and Kimsey Bald amphibolite field (stippled pattern). (b) Isolated amphibolite data. (c) Lake Chatuge Complex data. (d) Carroll Knob Complex data.

trend of decreasing CaO+MgO with increase in differentiation index.

Although the trend followed by the isolated amphibolite data is very much like the Chunky Gal Mountain trend, the isolated amphibolite data are more scattered. Several of the Hightower Bald samples plot at low Zr values below the main data trend, but amphibolites from different locations are not otherwise distinguishable. The fact that the Hightower Bald samples plot off-trend may be a result of major-element mobility because these samples do not plot in anomalous positions on the trace-element diagrams presented later.

The Carroll Knob data for the pyroxenites and metagabbros all plot at very low Zr and relatively high CaO+MgO, consistent with relict cumulate features observed in these groups. The garnet-amphibolites plot on both sides of the 20 wt% dividing line, below the pyroxenites and metagabbros at low Zr in a nearly vertical pattern. Thus, despite their high FeO/MgO ratios, they appear to have been derived from relatively unevolved protoliths. The amphibolites scatter toward higher Zr, but plot slightly below the main Chunky Gal Mountain/isolated amphibolite trend. The off-trend position of these samples may be due to major-element mobility because these samples tend to plot with the Chunky Gal Mountain and isolated amphibolite data on trace-element diagrams. The epidosites again plot in an entirely separate area of the diagram.

The data for the Lake Chatuge olivne gabbros and pyroxene gabbros plot at low Zr and high CaO+MgO values, consistent with their relict mineralogies. Many of the amphibolites plot at low Zr and CaO+MgO values well above 20 wt%, indicating probable cumulate origin for these rocks also. There are, however, several amphibolite samples which plot toward higher Zr and lower CaO+MgO values in positions which lie at the low Zr end of the Chunky Gal Mountain/isolated amphibolite trend.

Figures 8 through 13 show a series of two-element variation diagrams for selected major elements for all the suites. The data for all suites are distributed in generally the same way as described above for CaO+MgO: Chunky Gal Mountain and isolated amphibolite samples show very similar patterns with strong horizontal components; Carroll Knob and Lake Chatuge patterns are mainly clustered or vertical but have components that extend to higher Zr and overlap the Chunky Gal Mountain and isolated amphibolite data; and Kimsey Bald samples plot in loose clusters at low Zr values near the lower ends of the Chunky Gal Mountain trends. Most of the data for all suites show considerable scatter on these plots, and, although suggestions of fractionation-like trends occur for some elements on the Chunky Gal Mountain and isolated amphibolite diagrams, linear correlations are generally poor. Even where the data suggest fractionation-like trends, the limited magnitudes of variation for the major elements

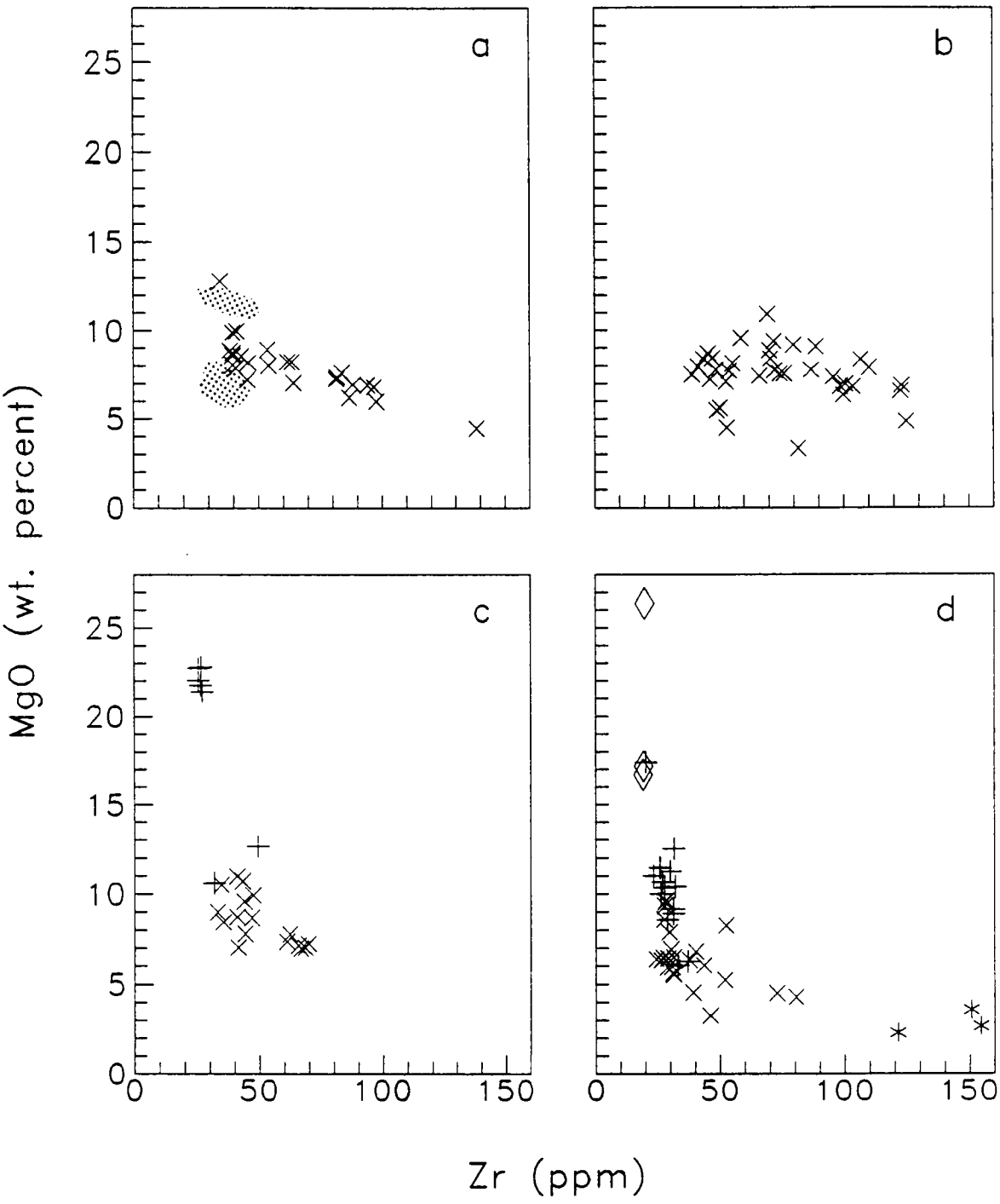

Figure 8. Plots of MgO (wt. %) versus Zr (ppm). Lithologic symbols as in previous figures. (a) Chunky Gal Mountain Complex data and Kimsey Bald amphibolite field (stippled pattern). (b) Isolated amphibolite data. (c) Lake Chatuge Complex data. (d) Carroll Knob Complex data.

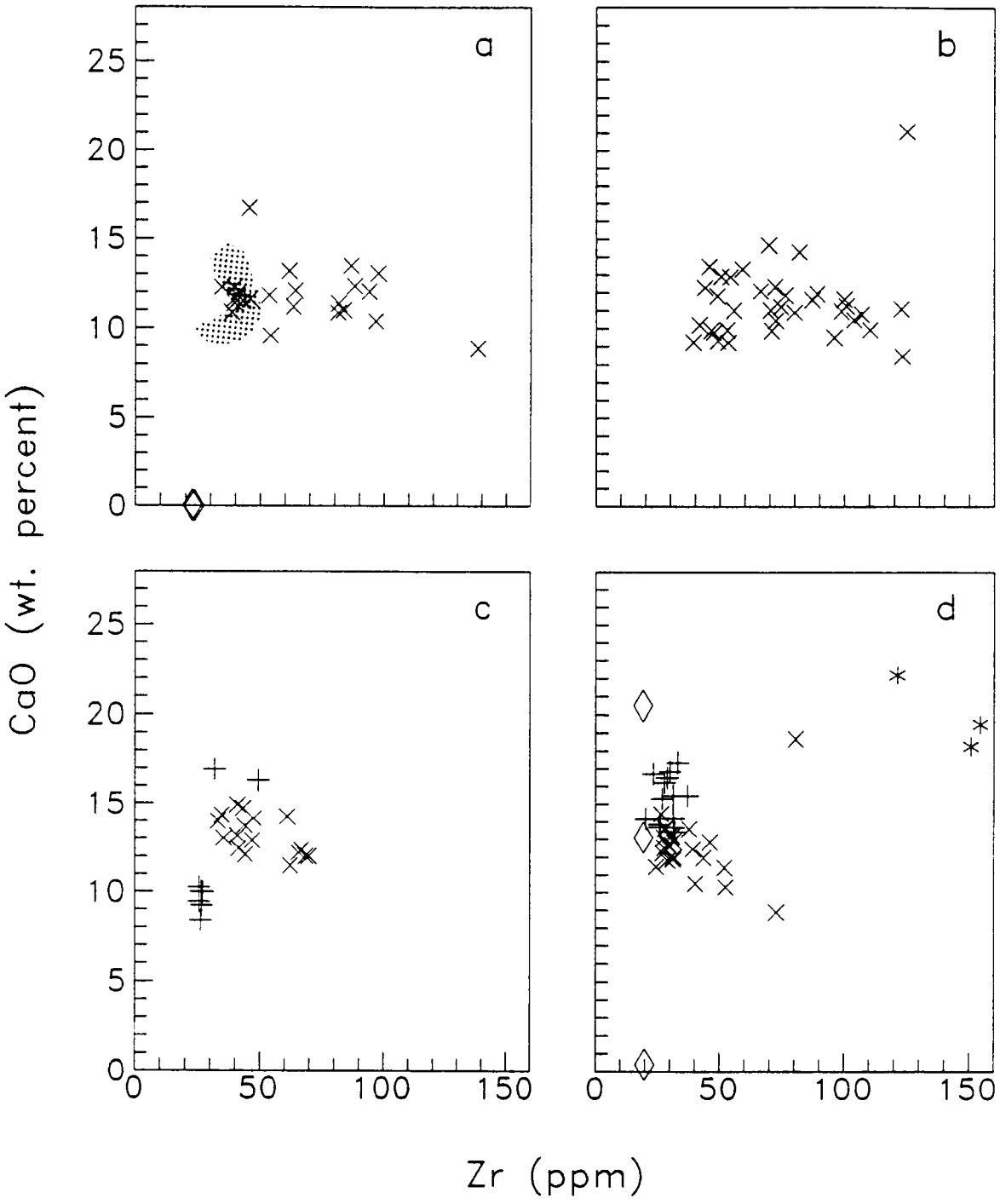

Figure 9. Plots of CaO (wt. %) versus Zr (ppm). Lithologic symbols as in previous figures. (a) Chunky Gal Mountain Complex data and Kimsey Bald amphibolite field (stippled pattern). (b) Isolated amphibolite data. (c) Lake Chatuge Complex data. (d) Carroll Knob Complex data.

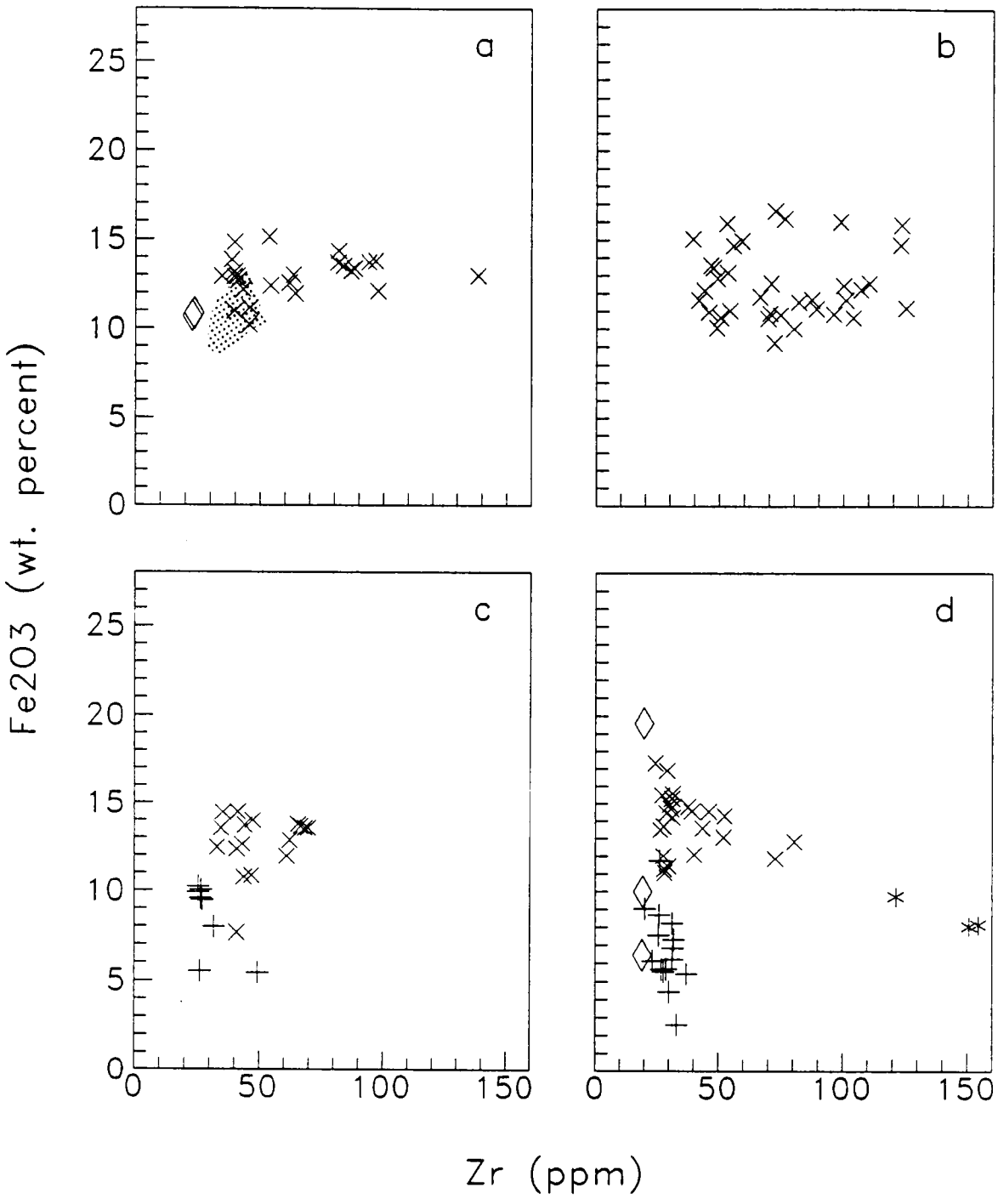

Figure 10. Plots of total iron calculated as Fe_2O_3 (wt. %) versus Zr (ppm). Lithologic symbols as in previous figures. (a) Chunky Gal Mountain Complex data and Kimsey Bald amphibolite field (stippled pattern). (b) Isolated amphibolite data. (c) Lake Chatuge Complex data. (d) Carroll Knob Complex data.

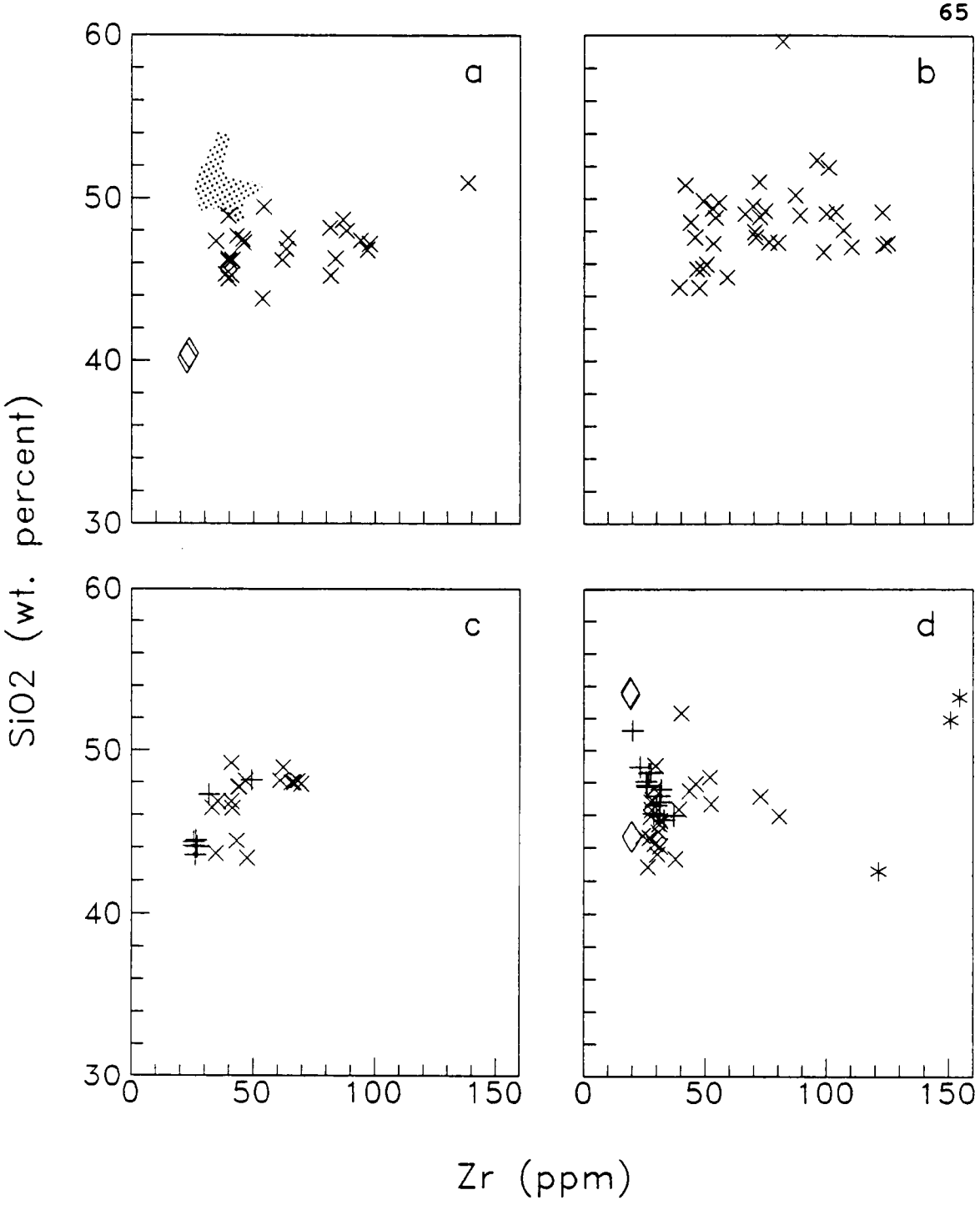

Figure 11. Plots of SiO_2 (wt. %) versus Zr (ppm). Lithologic symbols as in previous figures. (a) Chunky Gal Mountain Complex data and Kimsey Bald amphibolite field (stippled pattern). (b) Isolated amphibolite data. (c) Lake Chatuge Complex data. (d) Carroll Knob Complex data.

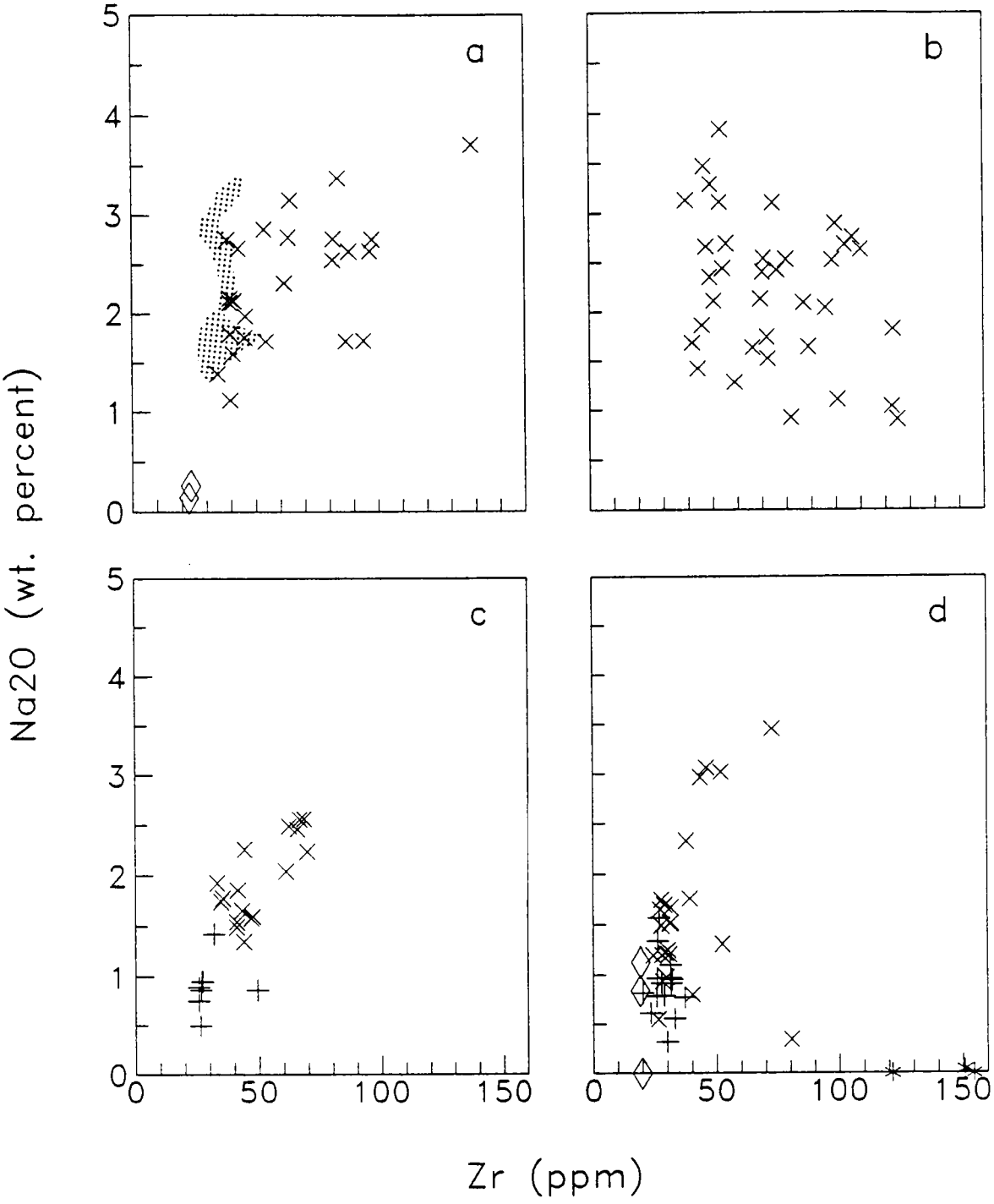

Figure 12. Plots of Na_2O (wt. %) versus Zr (ppm). Lithologic symbols as in previous figures. (a) Chunky Gal Mountain Complex data and Kimsey Bald amphibolite field (stippled pattern). (b) Isolated amphibolite data. (c) Lake Chatuge Complex data. (d) Carroll Knob Complex data.

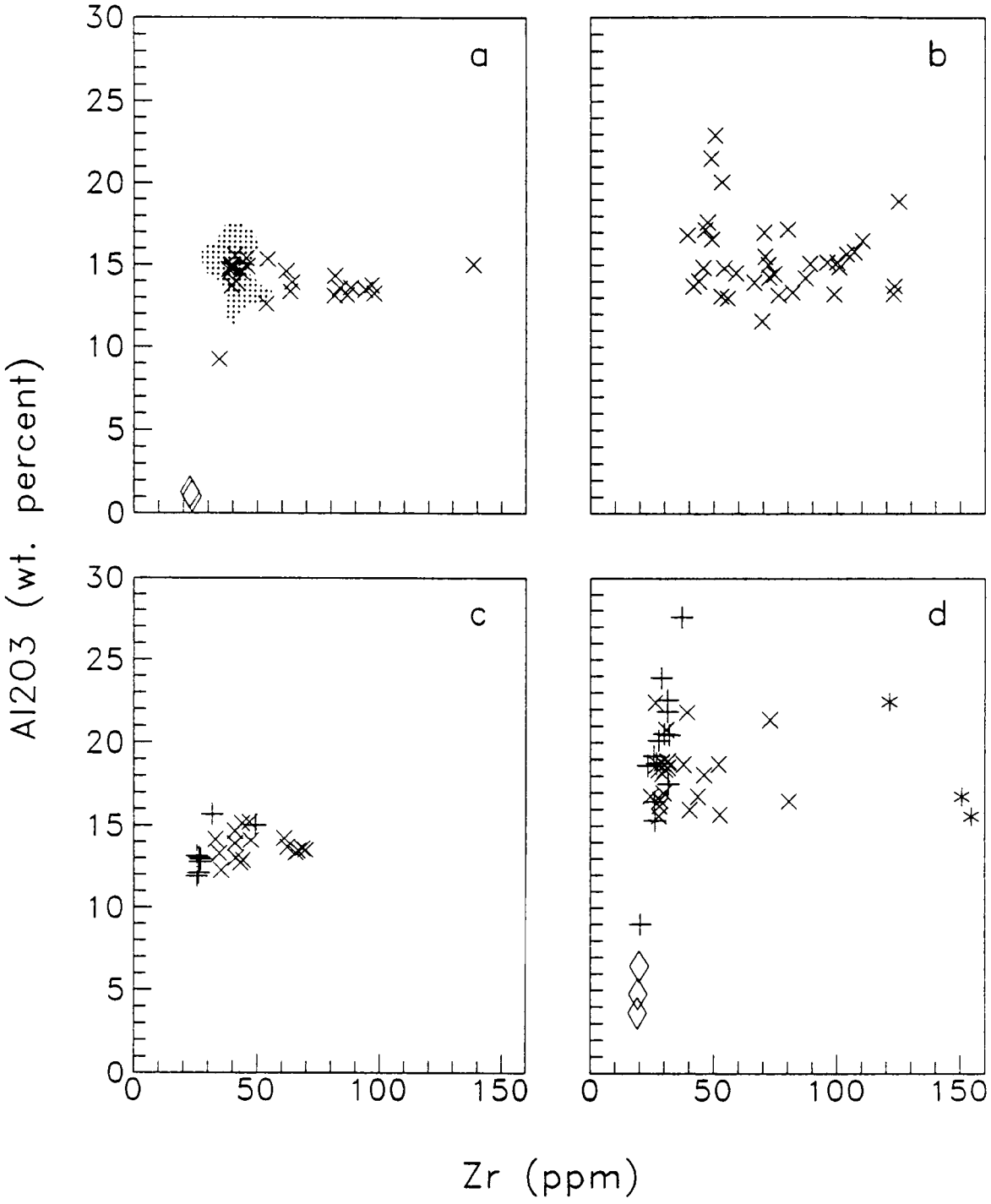

Figure 13. Plots of Al_2O_3 (wt. %) versus Zr (ppm). Lithologic symbols as in previous figures. (a) Chunky Gal Mountain Complex data and Kimsey Bald amphibolite field (stippled pattern). (b) Isolated amphibolite data. (c) Lake Chatuge Complex data. (d) Carroll Knob Complex data.

indicate that the suites are not highly differentiated with respect to major elements.

Major-element abundances for all suites fall in the same general ranges, and data for all suites are consistent with basaltic or more mafic protoliths for the rocks. For example, on the SiO_2 diagrams (Figure 11) all data (except for an anomalous isolated amphibolite sample) fall below 55 wt%, the approximate upper limit for basaltic compositions. The Carroll Knob data show the greatest variability in major-element values, with the metagabbros plotting at higher CaO and MgO and lower Fe_2O_3 than the amphibolites. One Carroll Knob sample classified as a pyroxenite plots at very high MgO and low CaO. This sample shows no relict mineralogy but consists mostly of magnesian amphibole and is interpreted as a replaced orthopyroxenite (cf. also the ACF diagram shown in Chapter IV). The Lake Chatuge olivine gabbros are readily distinguishable from the amphibolites on all diagrams. The pyroxene gabbros plot in positions closer to the amphibolites.

Trace- and Minor-Element Chemistry

Trends

Figures 14 through 19 show selected trace- and minor-element variation diagrams with Zr plotted on the abscissa. The elements and oxides chosen for plotting, Zr, Y, Nb, TiO_2, P_2O_5, Ni, and Cr, are those which are expected to be relatively

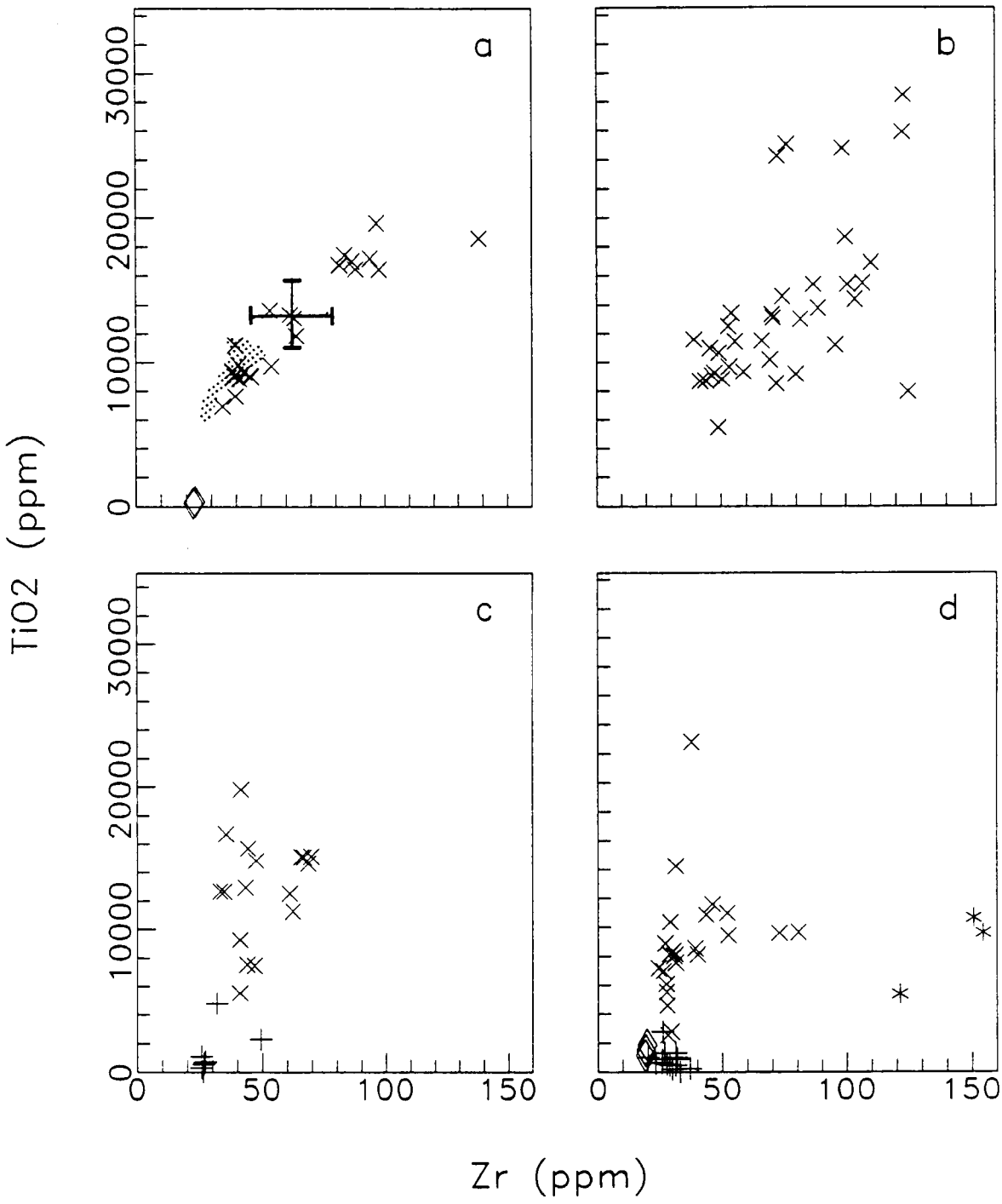

Figure 14. Plots of TiO_2 (ppm) versus Zr (ppm). Lithologic symbols as in previous figures. (a) Chunky Gal Mountain Complex data and Kimsey Bald amphibolite field (stippled pattern). (b) Isolated amphibolite data. (c) Lake Chatuge Complex data. (d) Carroll Knob Complex data. Error bars represent the standard errors of calibration in the XRF data.

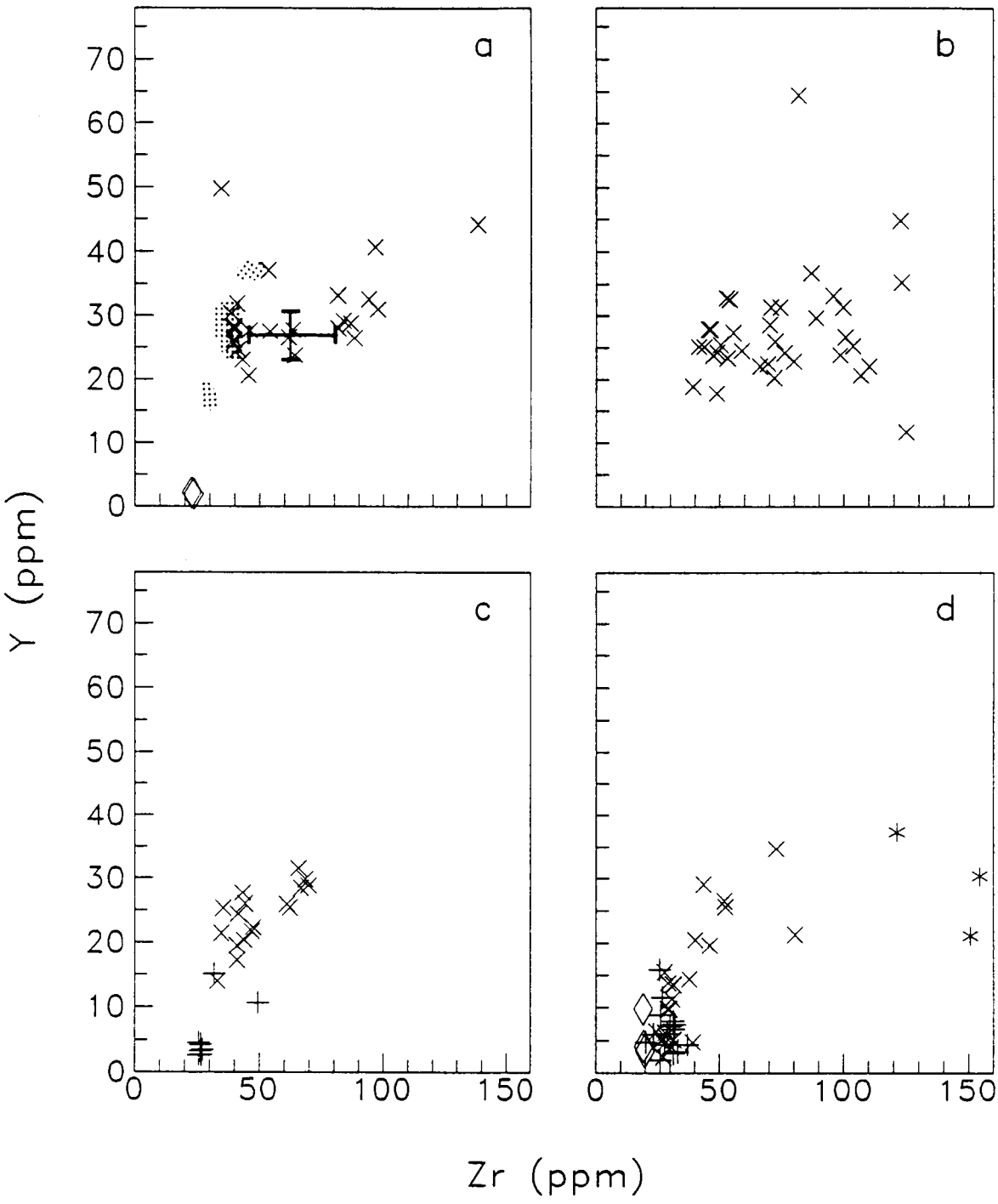

Figure 15. Plots of Y (ppm) versus Zr (ppm). Lithologic symbols as in previous figures. (a) Chunky Gal Mountain Complex data and Kimsey Bald amphibolite field (stippled pattern). (b) Isolated amphibolite data. (c) Lake Chatuge Complex data. (d) Carroll Knob Complex data. Error bars represent the standard errors of calibration in the XRF data.

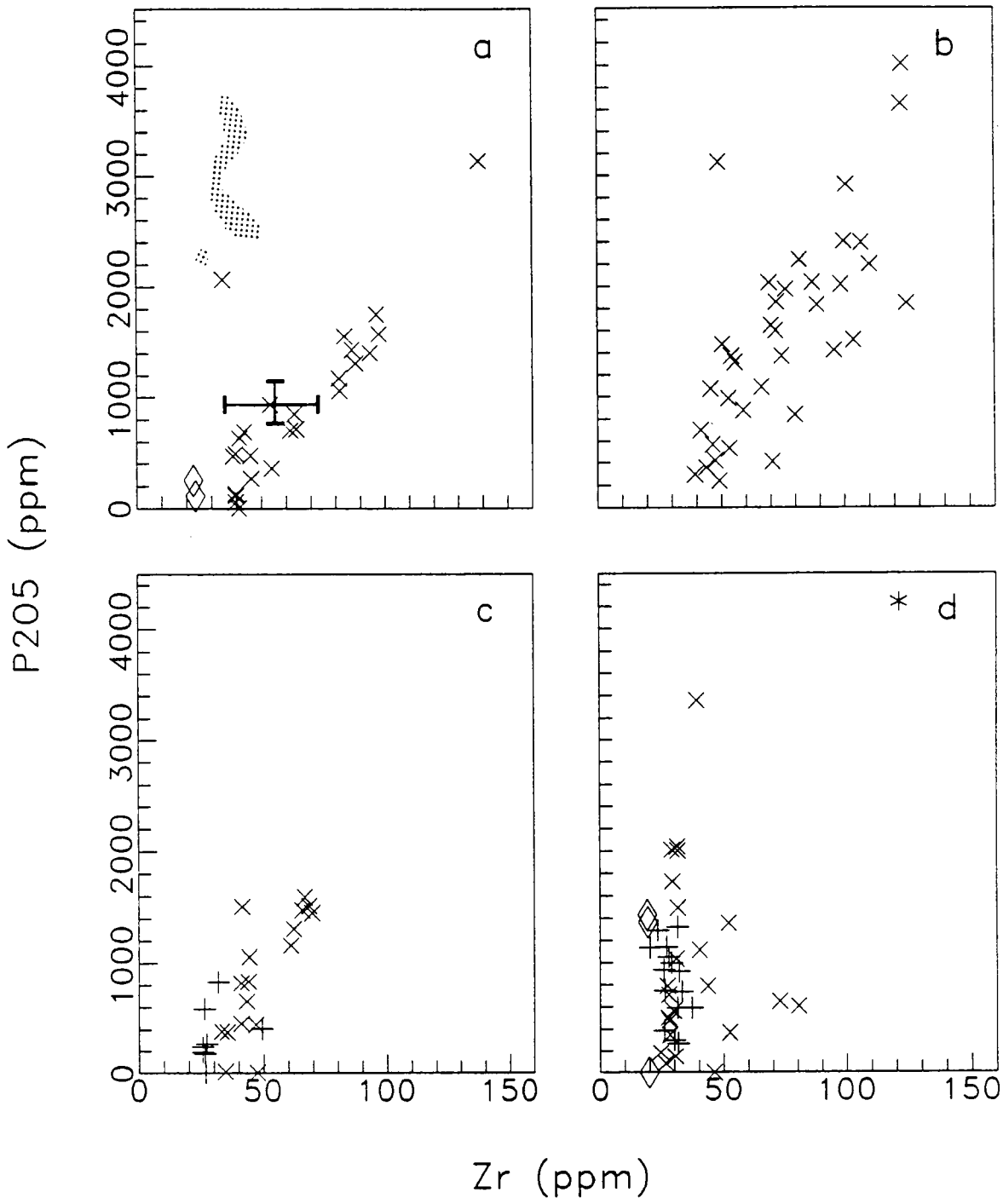

Figure 16. Plots of P_2O_5 (ppm) versus Zr (ppm). Lithologic symbols as in previous figures. (a) Chunky Gal Mountain Complex data and Kimsey Bald amphibolite field (stippled pattern). (b) Isolated amphibolite data. (c) Lake Chatuge Complex data. (d) Carroll Knob Complex data. Error bars represent the standard errors of calibration in the XRF data.

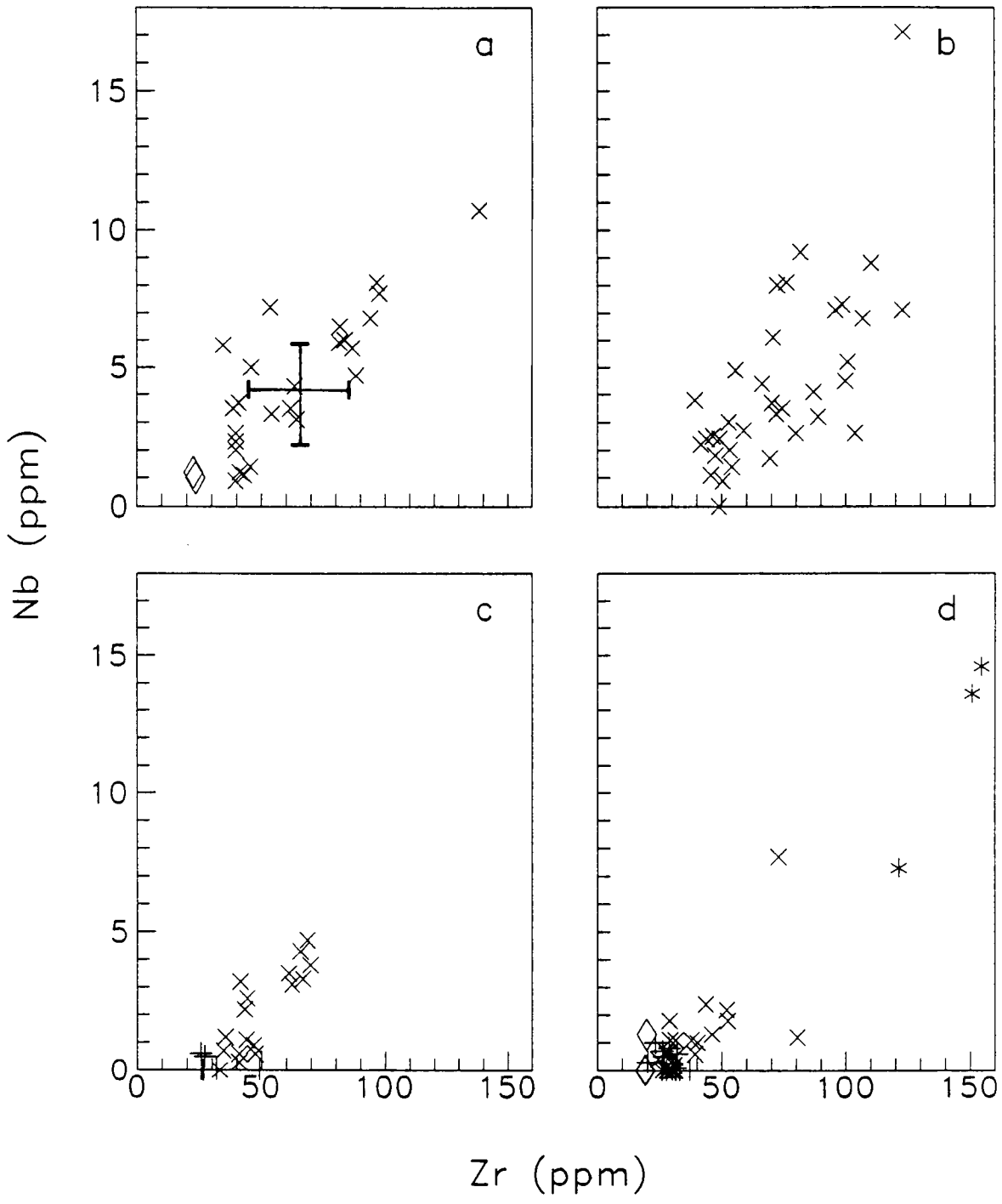

Figure 17. Plots of Nb (ppm) versus Zr (ppm). Lithologic symbols as in previous figures. (a) Chunky Gal Mountain Complex data. (b) Isolated amphibolite data. (c) Lake Chatuge Complex data. (d) Carroll Knob Complex data. Error bars represent the standard errors of calibration in the XRF data.

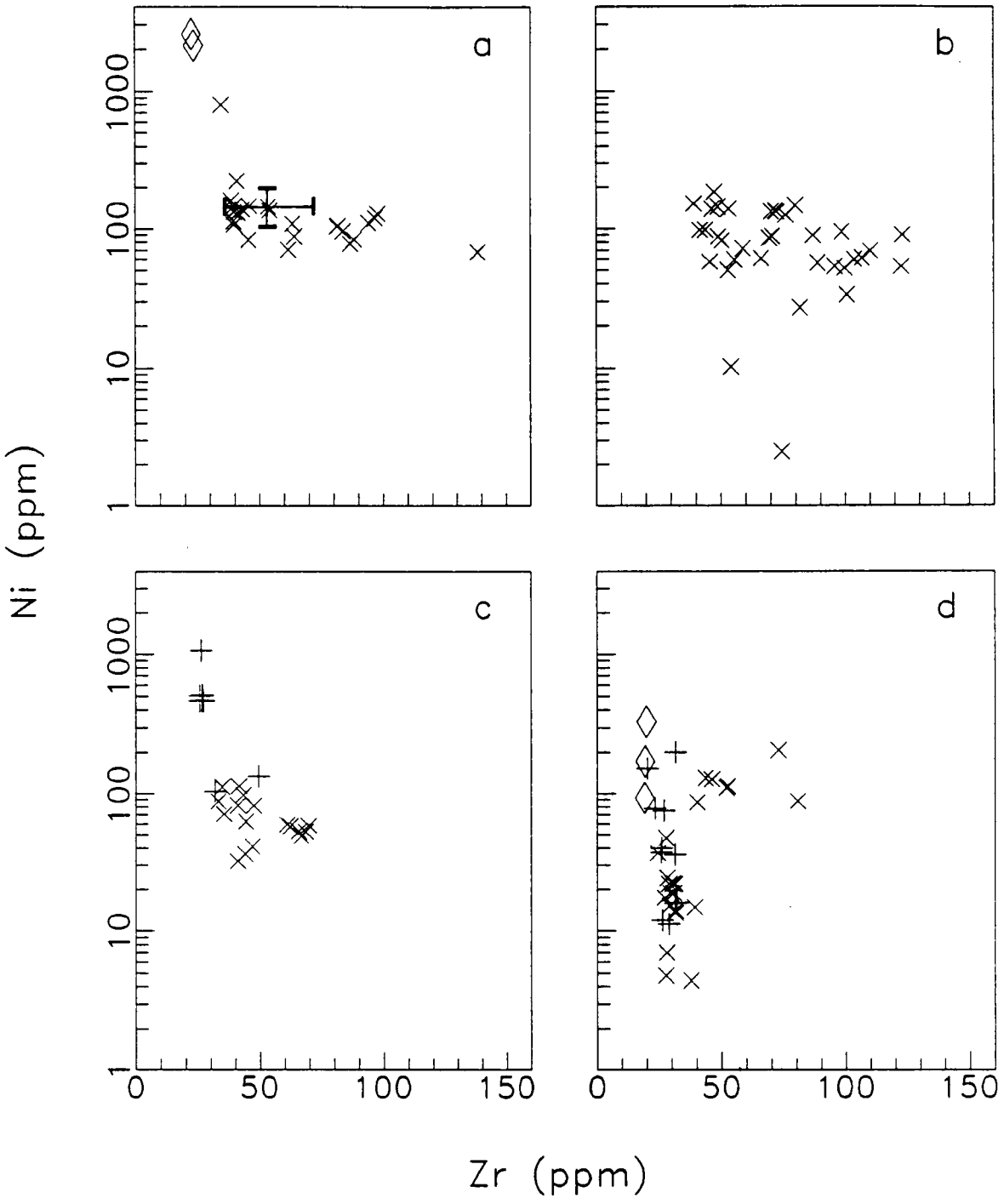

Figure 18. Plots of Ni (ppm) versus Zr (ppm). Lithologic symbols as in previous figures. (a) Chunky Gal Mountain Complex data. (b) Isolated amphibolite data. (c) Lake Chatuge Complex data. (d) Carroll Knob Complex data. Error bars represent the standard errors of calibration in the XRF data.

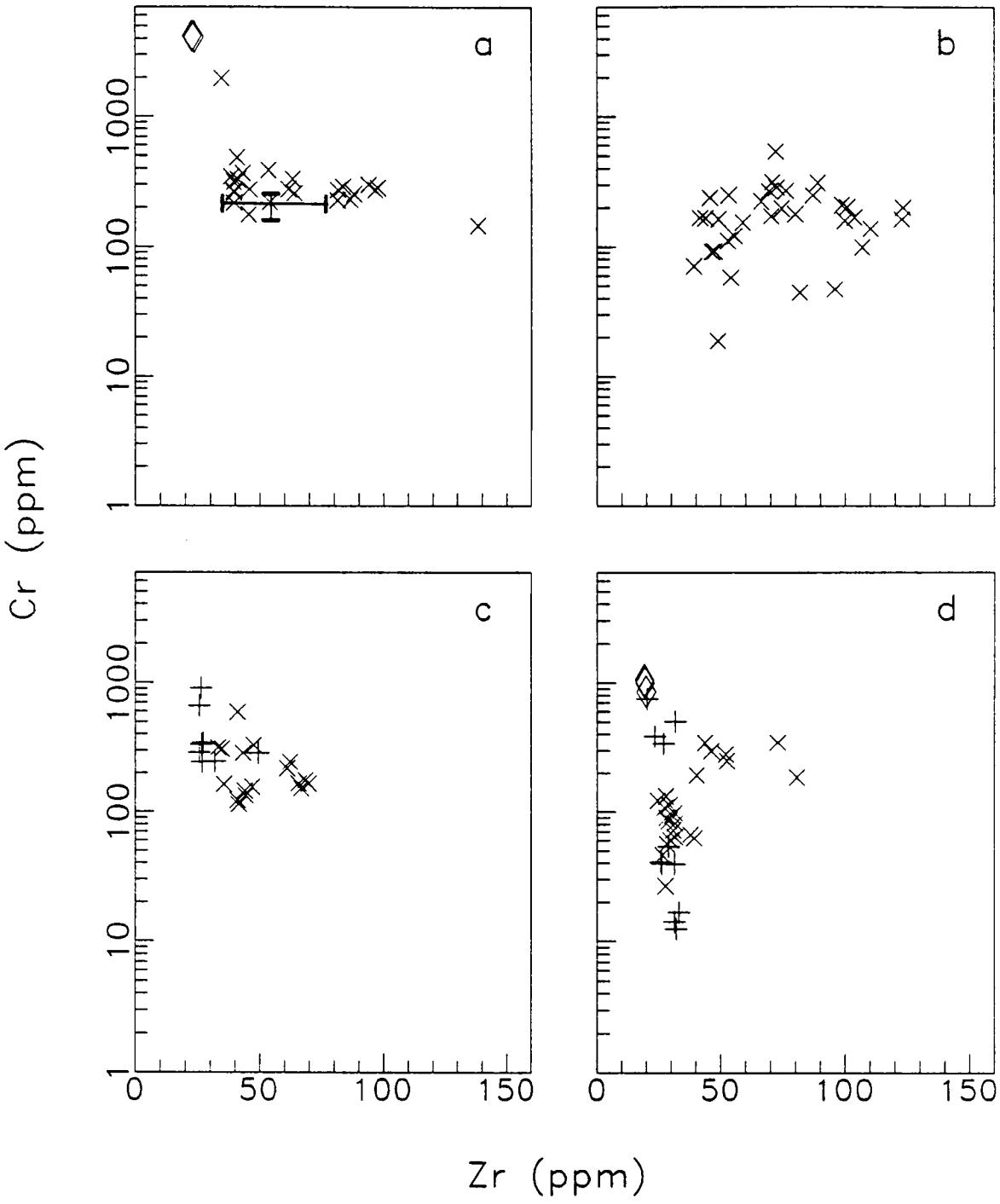

Figure 19. Plots of Cr (ppm) versus Zr (ppm). Lithologic symbols as in previous figures. (a) Chunky Gal Mountain Complex data. (b) Isolated amphibolite data. (c) Lake Chatuge Complex data. (d) Carroll Knob Complex data. Error bars represent the standard errors of calibration in the XRF data.

immobile during metamorphism because they are strongly bound in crystal lattices due to their high ionic charge to radius ratios. The data for Cr and Ni are plotted on semi-logarithmic diagrams to allow presentation of a wide range of concentrations. Trace- and minor-element distributions shown in the figures are similar to those observed in the major elements. The data from Chunky Gal Mountain and the isolated amphibolites show very similar distribution patterns, which suggest fractionation trends. The data for the isolated amphibolites are rather scattered, although Hightower Bald samples do not plot off-trend as they did in some of the major element diagrams. Correlation coefficients for linear regressions to the Chunky Gal Mountain and isolated amphibolite data are shown in Table 2, and error bars representing the standard errors of calibration are shown on the diagrams. The data from Kimsey Bald plot in clusters at the lower ends of the Chunky Gal Mountain trends, except for the P_2O_5 data which plots at anomalously high values. Nb, Ni and Cr data are not available for Kimsey Bald samples.

In contrast to the above suites, the data from Carroll Knob plot in essentially vertical patterns or clusters at low Zr. A few amphibolites fall on or near the Chunky Gal Mountain/isolated amphibolite trends. Metagabbros and amphibolites plot in clearly separate fields only on the TiO_2 diagram. As for the major elements, data for the epidosites plot in separate fields from the other lithologies.

Table 2. Correlation Coefficients for Least Squares Linear Regressions between Selected Elements and Zr

Element	Correlation Coefficient	
	Chunky Gal Mountain	Isolated Amphibolites
TiO_2	0.92	0.59
Y	0.35	0.17
P_2O_5	0.80	0.56
Nb	0.82	0.72
Ni	0.35	0.42
Cr	0.30	0.05
FeO/MgO	0.85	0.62

For the Lake Chatuge suite, the olivine gabbros are clearly separable from the amphibolites of the suite on all the diagrams. The two-pyroxene gabbro and clinopyroxene gabbro plot much closer to the amphibolite data on all diagrams. For all elements some of the amphibolites plot in a vertical pattern and some in positions which overlap with the Chunky Gal Mountain/isolated amphibolite trends.

Element Mobility

As alluded to earlier in this section, the trace- and minor-elements illustrated in Figures 14 to 19 are those which are expected to be immobile from theoretical considerations. In addition, many studies have shown these elements to be immobile during low-grade metamorphism (e.g. Coish, 1977; Smith and Smith, 1976). For a particular suite of rocks, element immobility can be inferred from the existence of good, igneous-like trace- and minor-element correlations in the data. The Chunky Gal Mountain data exhibit good, fractionation-like linear correlations with Zr for Nb, TiO_2 and P_2O_5 (Table 2). The correlations for Nb, TiO_2 and P_2O_5 are good indications that Zr and these elements have been immobile in the Chunky Gal Mountain rocks. The lack of correlation for Y, Ni and Cr is a result of flat data distributions for these elements rather than scattered data and, consequently, does not necessarily mean that these elements have been mobile. Igneous processes that can produce such flat trends are

discussed in the next chapter. Although the data for the isolated amphibolites are more scattered than those for the Chunky Gal Mountain rocks, and correlations are generally poorer (Table 2), the consistent congruence of the isolated amphibolite and the Chunky Gal Mountain trends indicates that Zr, Nb, TiO_2 and P_2O_5 (and probably Y, Ni and Cr) abundances in most of the isolated amphibolites have not been grossly altered. Similarly, the consistent association of the Kimsey Bald data for these elements (except P_2O_5) with the lower end of the Chunky Gal Mountain/isolated amphibolite trends and the lack of scatter in the data argue for immobility in the Kimsey Bald suite.

Similar arguments can be made for those amphibolites from the Carroll Knob and the Lake Chatuge suites for which the data consistently fall on or near the Chunky Gal Mountain/isolated amphibolite trends. However, because most of the data from the Carroll Knob and Lake Chatuge suites do not show fractionation-like trends, the argument against gross element mobility in these suites is somewhat tenuous. The Chunky Gal Mountain correlations, however, indicate that the elements under consideration have not been mobile in the metamorphic terrane in which all the suites are found, and all element variation patterns in the Carroll Knob and Lake Chatuge data can be explained in a consistent way by cumulate processes, without invoking element mobility.

CHAPTER IV

MODELS FOR TRACE-ELEMENT EVOLUTION IN CUMULATE ROCKS

Introduction

Approach

Although quantitative trace-element models of magma evolution are routinely used to analyze rocks representing liquid compositions, only a few attempts have been made to develop and apply equivalent models to cumulate rocks (Anderson and Greenland, 1969; Paster et al., 1974; Albarede, 1976). The purpose of this chapter is to modify and extend models of trace-element evolution in magmatic liquids to account for processes that affect trace-element evolution in cumulate rocks. These models are expressed as type curves that can be compared to the distributions of data on two-element variation diagrams.

Each process that is likely to affect trace-element concentrations in cumulate rocks is discussed and treated mathematically to the extent possible. Because the conditions for fractional crystallization are likely to exist in most magma chambers, fractional crystallization is the most widely used crystallization model (see Allegre and Minster (1978) for a review of the relevant physical parameters). The approach taken here is first to address the simplest case, fractional

crystallization in a closed system, and then incorporate other processes. Closed-system fractional crystallization (CFC) thus serves as a reference on which to build and with which to compare more realistic models. In addition, because analytical solutions are easily obtainable for CFC, its derivation is a convenient way to illustrate the principles upon which all model curves are constructed. Throughout the chapter assumptions and limitations pertaining to the mathematical formulations are examined.

The physical picture for which the models in this work are developed is that of a cumulate rock formed in magma chamber undergoing fractional crystallization. The terminology used is from Irvine (1982), who defines a cumulate as "an igneous rock characterized by a cumulus framework of touching mineral crystals or grains that were evidently formed and concentrated primarily through fractional crystallization." These crystals are called cumulus crystals; they are generally cemented together by a later generation of postcumulus material that crystallized from intercumulus liquid in the interstices of the cumulus framework. Note that this definition does not imply crystal settling or any other mode of crystal accumulation; the only requirement for a crystal to be cumulus is that it formed by fractional crystallization, i.e. it was only momentarily in equilibrium with the main body of liquid and was subsequently isolated from it.

All attempts to model liquid evolution from observed geochemical trends in volcanic rocks are predicated on the assumption that individual samples represent increments of composition along the liquid line of descent. In principle, cumulate rocks can be thought of in an analogous way: they represent increments of composition along the cumulate evolution curve. As is shown in the next section, on a two-element variation diagram the observed trend in cumulate rocks ideally should replicate the shape of the corresponding liquid trend but be displaced from it by distances which depend on the relevant bulk distribution coefficients for fractionating assemblages. In practice, however, the compositions of cumulate rocks are likely to be complicated by processes different from those affecting the main body of the magma. The cumulate trend may, therefore, differ substantially from that of the liquid to which it is related and from that predicted by simple fractionation models.

Processes which are likely to play a part in determining compositional trends in cumulate rocks are:

1) Closed-system fractional crystallization (CFC);
2) Variations in the ratio of cumulus crystals to trapped intercumulus liquid (CTL);
3) Variations in the mode due to cumulus crystal sorting (i.e. the accumulation of phases in excess of eutectic proportions);
4) Open-system fractional crystallization (OFC):

a. Recharging of the magma chamber by draughts of unfractionated magma;

b. Assimilation of material of different composition than the magma;

5) Changes in bulk distribution coefficients; and

6) Element mobility (e.g. diffusion, metasomatism, alteration and weathering).

For any suite of rocks representing the products of a magma chamber, it is probable that several of these processes have affected the observed compositional trends. Processes 1 to 4 are treated mathematically in the following sections. Changes in the bulk distribution coefficients (process 5) may be due to changes in temperature, pressure, magma composition, crystal composition or phases on the liquidus. Except for the last, these effects are difficult to evaluate and beyond the scope of this study. The bulk distribution coefficients are assumed then to be constant or to change discontinuously due to changes in liquidus phases. The distribution coefficients used are derived from generally accepted mineral/liquid partition coefficients in the literature and are discussed in detail in the next section. It is recognized that these values are only approximate, and the effect of using different values is evaluated on a case-by-case basis. Changes in composition due to weathering and alteration (process 6) were factored out by using only fresh samples which showed no evidence of late-stage alteration. The possibility of element

mobility during metamorphism was minimized by modeling only those elements which are predicted to be immobile on theoretical grounds and which appear to have been immobile based on examination of the data (Chapter III). In addition, compositional changes due to metamorphism or diffusion from the host rocks are treated as mixing processes and examined on a case-by-case basis.

Constraints

The models which are developed in the following sections have many adjustable parameters, and it is not possible to construct models for all possible combinations of these parameters. Rather, the analysis must be constrained by considering only reasonable physical conditions and ultimately by the data under consideration; i.e. the parameters explored must be chosen for specific hypotheses which are made based on chemistry, field relations and petrography. Therefore, although the development of models is treated as a separate chapter, the processes emphasized and the parameter ranges illustrated are suggested by the data presented in Chapters II and III.

Bulk Distribution Coefficients

The most basic model parameters are the bulk distribution coefficients. There are two sources of uncertainty in the bulk distribution coefficients used in this study: the first

is uncertainty in the applicability of measured mineral/liquid partition coefficients, and the second is uncertainty about the relative proportions of phases making up the bulk cumulus assemblage. Uncertainty about the applicability of measured mineral/liquid partition coefficients is due not only to possible experimental error, but also to the composition and temperature dependencies of partition coefficients. Table 3 is a compilation of crystal/liquid partition coefficients for mafic compositions found in the literature for the immobile trace- and minor-elements modeled in this study. With the exception of some of the values for Y from Fodor (1987) and some of the values for TiO_2 from Allegre et al. (1977), reported partition coefficients are reasonably consistent. For this study I use the values from Pearce and Norry (1979) for TiO_2, Y, Zr, and Nb, an average of the values from Fodor (1987) and Anderson and Greenland (1969) for P_2O_5, and values from the ranges reported in Irving (1978) for Ni and Cr. The partition coefficients for Cr and, particularly, Ni are highly temperature- and composition-dependent, and reported values cover a wide range. However, the arguments and conclusions presented later do not depend on exact values for the distribution coefficients for these elements or any other elements, but only the fact that they are within reasonable ranges.

Table 3. Mineral/Liquid Partition Coefficients

Element	Mineral							
	Ol	Pl	Cpx	Opx	Mt	Ilm	Chr	Ap
Zr[a]	0.01	0.01	0.1	0.03	0.1	0.28	-	-
Zr[b]	0.01	0.01	0.2	0.01	-	-	-	-
Zr[c]	-	-	0.12	-	-	0.27	-	-
Ti[a]	0.02	0.04	0.3	0.1	7.5	~50	-	-
Ti[b]	0.01	0.01	0.2	0.02	-	-	-	-
Ti[c]	0.024-0.07	0.045	0.14-0.82	0.11	-	-	-	-
Ti[d]	0.3	0.03	1.3	0.7	-	100	-	-
Y[a]	0.01	0.03	0.5	0.2	0.2	-	-	-
Y[b]	0.13	0.18	0.7	0.1	-	-	-	-
Y[c]	-	0.13-0.31	-	-	-	-	-	2-3*
Y[f]	-	-	-	-	-	-	-	2*
P_2O_5[b]	0.01	0.01	0.01	0.01	-	-	-	-
P_2O_5[c]	0.043	0.024	0.009	0.014	-	-	-	-
Nb[a]	0.01	0.01	0.1	0.15	0.4	0.8	-	-
Nb[c]	-	-	0.02	-	-	0.81	-	-
Ni[c]	2-33	0.04	1.2-9	1.0-10	12.2	-	-	-
Ni[d]	13	0.26	4	6.6	-	-	-	-
Cr[c]	0.5-1.5	-	1.5-1.8	1.6-10	100-620	6	-	-
Cr[d]	1.8	0.04	15	2.8	-	-	-	-

Sources: [a]Pearce and Norry (1979), [b]Fodor (1987), [c]Irving (1978), [d]Allegre et al. (1977), [e]Anderson and Greenland (1969), and [f]Watson and Green (1981). *Based on data for heavy rare-earth elements from Henderson (1984). Values used for modeling are shaded.

The second uncertainty in bulk distribution coefficients results from the lack of data about the identity and proportions of phases making up the equilibrium cumulus assemblage. For Chunky Gal Mountain, Lake Chatuge and Carroll Knob, enough relict igneous mineralogy has been preserved to allow reasonable inferences about the modal compositions of the cumulus assemblages. At Chunky Gal Mountain and Lake Chatuge, dunites, troctolites and olivine gabbros dominate the relict cumulate rocks, indicating that an appropriate model cumulus assemblage for the mafic rocks of these suites is clinopyroxene + olivine + plagioclase (Cpx + Ol + Pl). The relative proportions of these minerals crystallizing at equilibrium can be estimated from phase relations. For a first approximation the system diopside - forsterite - anorthite (Di - Fo - An) is a good analog for mafic rocks. Equilibria in this system are pressure dependent, and phase diagrams have been published for pressures of 1 atm and for 7 kbar and above (Morse, 1980; Presnall, 1978; Irvine, 1970; Libourel et al., 1989). The depth at which the rocks of this study crystallized is not known, but 7 kbar is too high to be representative of most crustal pressures, and the 1 atm diagram is probably more realistic. In addition, the phase diagram constructed by Irvine (1970) for natural systems, based on data from both synthetic and natural systems, indicates almost the same mineral proportions as those seen in the 1 atm Di - Fo - An phase diagrams. The mineral

proportions indicated by the 1 atm Di - Fo - An phase diagrams (or equivalently Irvine's diagram for natural systems), thus, appear to be appropriate for estimating model distribution coefficients for Chunky Gal Mountain and Lake Chatuge, and because of the similarity of data trends, probably for the isolated and the Kimsey Bald amphibolites also.

Figure 20a shows the Cpx - Ol - Pl phase diagram and the ternary eutectic point E1 from Irvine (1970). The point E1 can be used to approximate the relative proportions of clinopyroxene, olivine and plagioclase when all three minerals are crystallizing from a liquid. All published 1 atm phase diagrams in the Di - Fo - An system and the Irvine (1970) diagram for natural systems suggest eutectic proportions of clinopyroxene, olivine and plagioclase of approximately 50%, 8% and 42% by weight, respectively. Bulk distribution coefficients calculated using these mineral ratios and the partition coefficients from Table 3 are shown in Table 4. Note that plagioclase and olivine behave similarly with respect to the incompatible elements, and that the distribution coefficients for these elements are essentially determined by the ratio of plagioclase + olivine to clinopyroxene. The effect of increasing pressure is to shrink the plagioclase field in Figure 20a and shift the E1 composition toward An. Using phase proportions higher in plagioclase would decrease distribution coefficients for all elements in Table 4 but would not change the slopes and

Figure 20. Phase diagrams and ACF plots. (a) Cpx - Ol - Pl phase diagram showing ternary eutectic point E1 (wt. %), redrawn from Irvine (1970). (b) Chunky Gal Mountain Complex data, isolated amphibolite data, Lake Chatuge Complex data, and E1 (open circle) plotted on ACF diagram (mol. %). A = Al_2O_3 + Fe_2O_3 - K_2O - Na_2O, C = CaO - $3.3P_2O_5$ and F = FeO + MgO + MnO. Data plotted assuming Fe_2O_3 = TiO_2 + 1.5 (Irvine and Baragar, 1971). E1 plotted assuming the composition of an augite from an olivine gabbro from the Skaergaard intrusion (augite #16, Table 17, Deer, Howie and Zussman, 1963). Lithologic symbols as in previous figures. (c) Cpx - Opx - Pl phase diagram showing ternary eutectic point E2 (wt. %), redrawn from Irvine (1970). (d) Carroll Knob Complex data and E2 (open circle) plotted on ACF diagram (mol. %). A, C, F, and Fe_2O_3 calculated as above. E2 plotted assuming the composition of an augite from an augite gabbro from the Stillwater intrusion (augite #6, Table 17, Deer, Howie and Zussman, 1963).

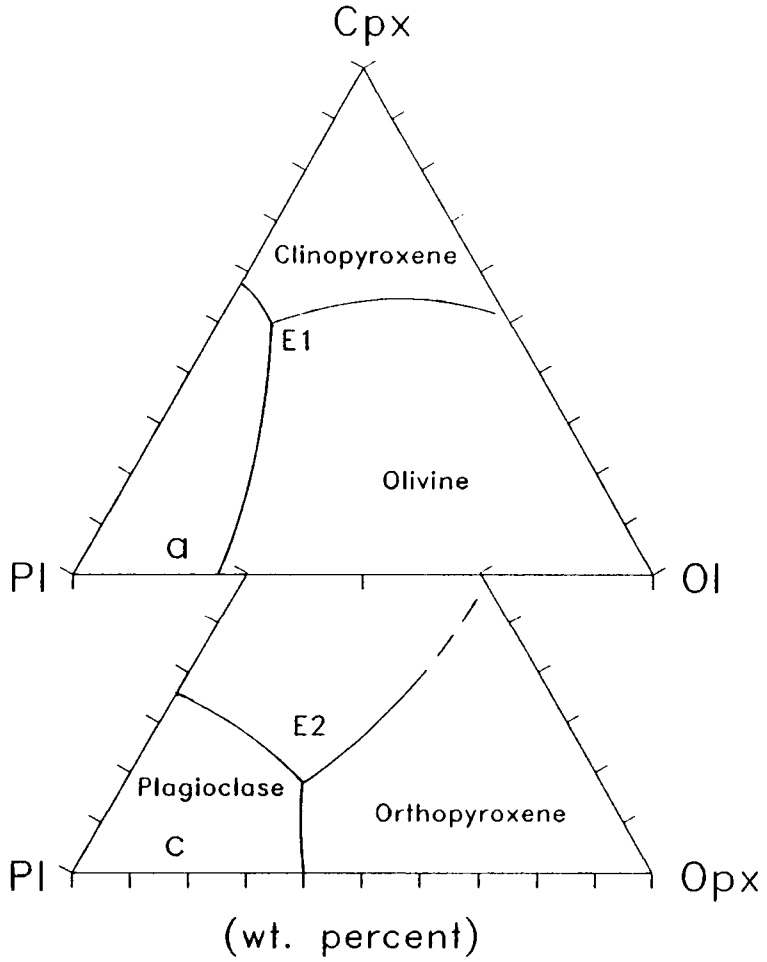

(wt. percent)

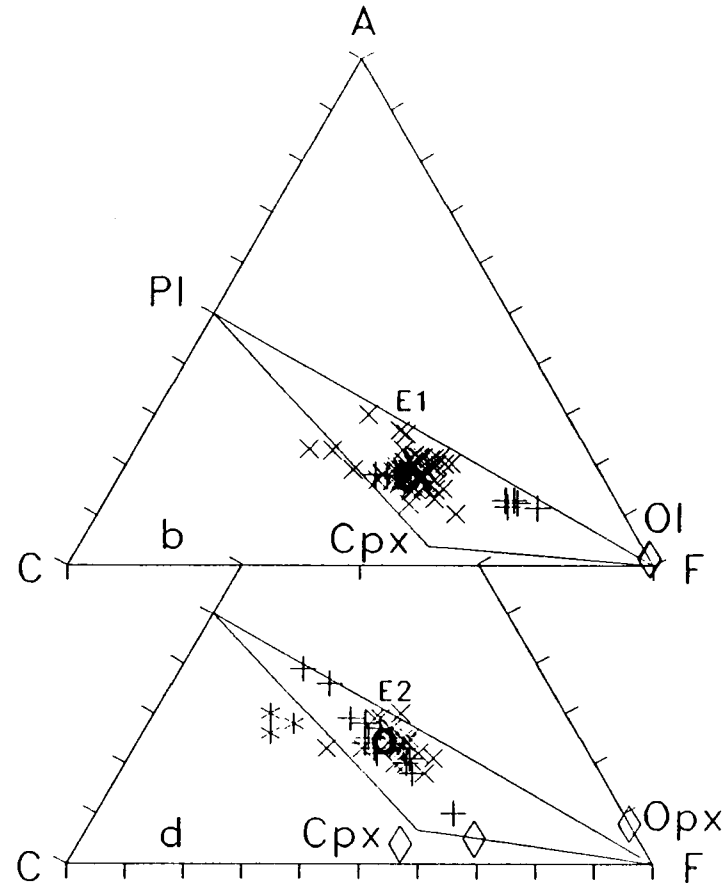

(mol. percent)

Table 4. Bulk Distribution Coefficients for Model Eutectic Assemblages

Element	Assemblage	
	$Ol_8 + Cpx_{50} + Pl_{42}$	$Opx_{20} + Cpx_{30} + Pl_{50}$
TiO_2	0.17	0.11
Zr	0.06	0.03
Y	0.26	0.18
P_2O_5	0.01	0.01
Nb	0.06	0.07
Ni	3.95	1.90
Cr	0.95	2.50

lengths of model curves enough to affect conclusions presented later. Figure 20b, which is an ACF diagram (defined in the caption) showing the point E1 and the data for Chunky Gal Mountain, Lake Chatuge and the isolated amphibolites, confirms that most of the rocks of the suites in question have bulk compositions that are consistent with eutectic (E1) proportions of clinopyroxene, olivine and plagioclase. The Kimsey Bald data, although not shown, plot on top of the data from the other suites.

Relict mineralogy at Carroll Knob suggests that a cumulus assemblage of clinopyroxene + orthopyroxene + plagioclase (Cpx + Opx + Pl) is the appropriate assemblage from which to calculate bulk distribution coefficients for this complex. Irvine (1970) also constructed a phase diagram for this system, which is based on both synthetic and natural systems (Figure 20c). The phase proportions implied by the eutectic point (E2) on this diagram for clinopyroxene, orthopyroxene and plagioclase are 20%, 30% and 50% by weight, respectively. Table 4 also shows bulk distribution coefficients calculated for these proportions. Bulk distribution coefficients for this assemblage (two-pyroxene gabbro) are somewhat lower than those for the clinopyroxene + olivine + plagioclase assemblage (olivine gabbro). However, the relevant aspects of model curves depend primarily on ratios of distribution coefficients rather than absolute values, and use of plagioclase + clinopyroxene + orthopyroxene-based distribution coefficients

rather than those for a plagioclase + olivine + clinopyroxene assemblage does not make much difference in the slopes and the shapes of model curves (see next chapter). Figure 20d shows an ACF diagram on which E2 is plotted with the Carroll Knob data. The data spread somewhat around the point, but are consistent with fractionation of a two-pyroxene gabbro assemblage modified by other cumulate processes.

Other Parameters

Two other basic model parameters which must be constrained are the degree of fractionation, expressed as the weight fraction of residual liquid, F, and the weight fraction of trapped liquid or intercumulus liquid, k. The transition from basalts to andesites is usually taken to occur at about F = 0.5. Because all major element data indicate that we are dealing with basaltic or more mafic suites, F is limited to greater than about 0.5 for this study. The upper limit on k is also about 0.5, as indicated in the literature on cumulate rocks (Albarede, 1976; Irvine, 1979; Morse, 1980). For open-system models there are three additional parameters which need to be constrained. Limitations on these parameters will be discussed in a later section after the basic model has been introduced.

Closed-System Fractional Crystallization (CFC)

CFC has been thoroughly described in the literature (e.g. Neumann et al., 1969; Allegre et al., 1977; Allegre and Minster, 1978; Albarede, 1976), and all equations presented in this section can be found in these references. However, because it provides the baseline for this study and clearly illustrates some important principles, certain aspects are reviewed here. The assumptions which apply to CFC are: the crystallizing phases are only momentarily in equilibrium with the liquid and are subsequently isolated from it; the total mass of the system does not change; and the bulk distribution coefficients for the system are constant. The basic expression for CFC is:

$$C^l = C^{l,0} F^{\bar{D}-1}, \qquad (1)$$

where

C^l = wt% of an element in the residual liquid,

$C^{l,0}$ = wt% of an element in the original liquid,

F = weight fraction of residual liquid,

$\bar{D}$ = bulk distribution coefficient for the element

$= \Sigma_p X^p D^p$,

where D^p = mineral/liquid partition coefficient for the element for phase p, and

X^p = weight fraction of phase p in the cumulus assemblage.

The equivalent equation for the instantaneous cumulate in equilibrium with the liquid (C^c) is:

$$C^c = \bar{D}C^{l,0}F^{\bar{D}-1} = \bar{D}C^l. \qquad (2)$$

Equations (1) and (2) can be written in logarithmic form:

$$\log C^l = \log C^{l,0} + (\bar{D} - 1)\log F, \qquad (1')$$

and

$$\log C^c = \log \bar{D} + \log C^{l,0} + (\bar{D} - 1)\log F \qquad (2')$$
$$= \log \bar{D} + \log C^l.$$

In this form it is evident that on plots of log C vs log F both the residual liquid and the cumulate trends are straight lines with slopes of $\bar{D} - 1$; the cumulate trend is simply displaced from the liquid trend by a distance of log $\bar{D}$ parallel to the C axis. This is an example of the more general relationship between equilibrium cumulate and liquid trends which obtains regardless of the model under consideration; the instantaneous cumulate trend is always a replica of the residual liquid trend but is displaced from it by a distance which depends on $\bar{D}$.

Two-Element Plots

When analyzing measured data, F is usually not known. Instead the variation in the concentration of an incompatible element is used as a measure of fractionation or degree of crystallization, and other elements are plotted against the chosen element on two-element variation diagrams. To compare mathematical models with measured data, the models need to be expressed in terms of two-element variation diagrams (e.g. Pearce and Norry, 1979; Allegre, 1978). For CFC an analytical expression for the concentration of an element i in terms of the concentration of an element j is easily obtained for the residual liquid by writing Equation (1') for each element, solving for F in terms of C_j^l, and substituting this expression for F into the equation for C_i^l. The result is:

$$\log C_i^l = \log C_i^{l,0} - [(\bar{D}_i - 1)/(\bar{D}_j - 1)]\log C_j^{l,0} + [(\bar{D}_i - 1)/(\bar{D}_j - 1)]\log C_j^l$$

$$= \text{constant} + [(\bar{D}_i - 1)/(\bar{D}_j - 1)]\log C_j^l \qquad (3)$$

A plot of $\log C_i^l$ against $\log C_j^l$ is also a straight line with a slope of $(\bar{D}_i - 1)/(\bar{D}_j - 1)$, which depends only on the bulk distribution coefficients for elements i and j. Interpretations based on model curves depend primarily on the slopes and lengths of the curves. $C_i^{l,0}$ and $C_j^{l,0}$ are usually not

known, but can be set to 1 without affecting the slope or the length of a curve, and the constant term is then zero.

Computer-Generated Plots

An equivalent method of solving for C_i in terms of C_j that is useful for generating log C_i vs log C_j model curves is to solve Equation (1) or (2) for C_i and C_j for several values of F, and then plot log C_i and log C_j for equal values of F against each other. By proper choice of $\bar{D}_i$ and $\bar{D}_j$ any pair of elements can be modeled. This procedure is especially useful for models that are mathematically more complex than CFC, and all model curves in this dissertation were generated this way on a personal computer using a spread sheet. $C_j^{l,0}$ and $C_i^{l,0}$ are always set to 1.

The use of logarithms is an important aspect of making these curves, because on logarithmic plots the same curves may be compared to measured concentrations at any level. Distances on logarithmic plots represent multiplicative factors rather than absolute changes in concentration, and changes in liquid concentrations are always expressed as the factor C/C^0. A change in concentration by a constant factor, then, is always the same distance on a log C_i vs log C_j plot, regardless of the actual concentrations involved (log C/C^0 = log C - log C^0). This is, of course, not the case on a C_i vs C_j plot where, for example, a factor of 10 in the ppm range represents a very different distance on the graph than a

factor of 10 in the 100 ppm range. Model plots of log C_i vs log C_j (or equivalently plots of C_i vs C_j on log - log scales) may, therefore, be compared to measured concentrations at any level (i.e. may be freely translated parallel to the i and j axes) as long as data and model curves are plotted on the same scale. All model curves in this work are plotted on standard 1x1 log scales.

CFC Model Curves

Figures 21a and 21b show model curves (lines in this special case) for both the residual liquid, C_i^l vs C_j^l, and the equilibrium cumulate, C_i^c vs C_j^c, for incompatible and compatible elements, respectively. The abscissa of these graphs is C_j (cf. Equation 3). By the proper choice of $\bar{D}_j$ the abscissa can be made to represent any element one wishes to use as a differentiation index. In Figures 21a and 21b $\bar{D}_j = 0.06$; this is the approximate bulk distribution coefficient for Zr for an eutectic cumulus assemblage of clinopyroxene + olivine + plagioclase (olivine gabbro) (Table 4), and this axis thus represents the concentration of Zr for this model assemblage. The ordinate is C_i; again this axis may be made to model any element by the appropriate choice of $\bar{D}_i$. Curves for $\bar{D}_i = 0.26$, 0.01, 0.17, 0.06, 2 and 4, appropriate for Y, P_2O_5, TiO_2, Nb, Cr and Ni, respectively, for an olivine gabbro cumulus assemblage are illustrated in the figures. The type of symbol on a curve indicates the $\bar{D}_i$ value or element for which the

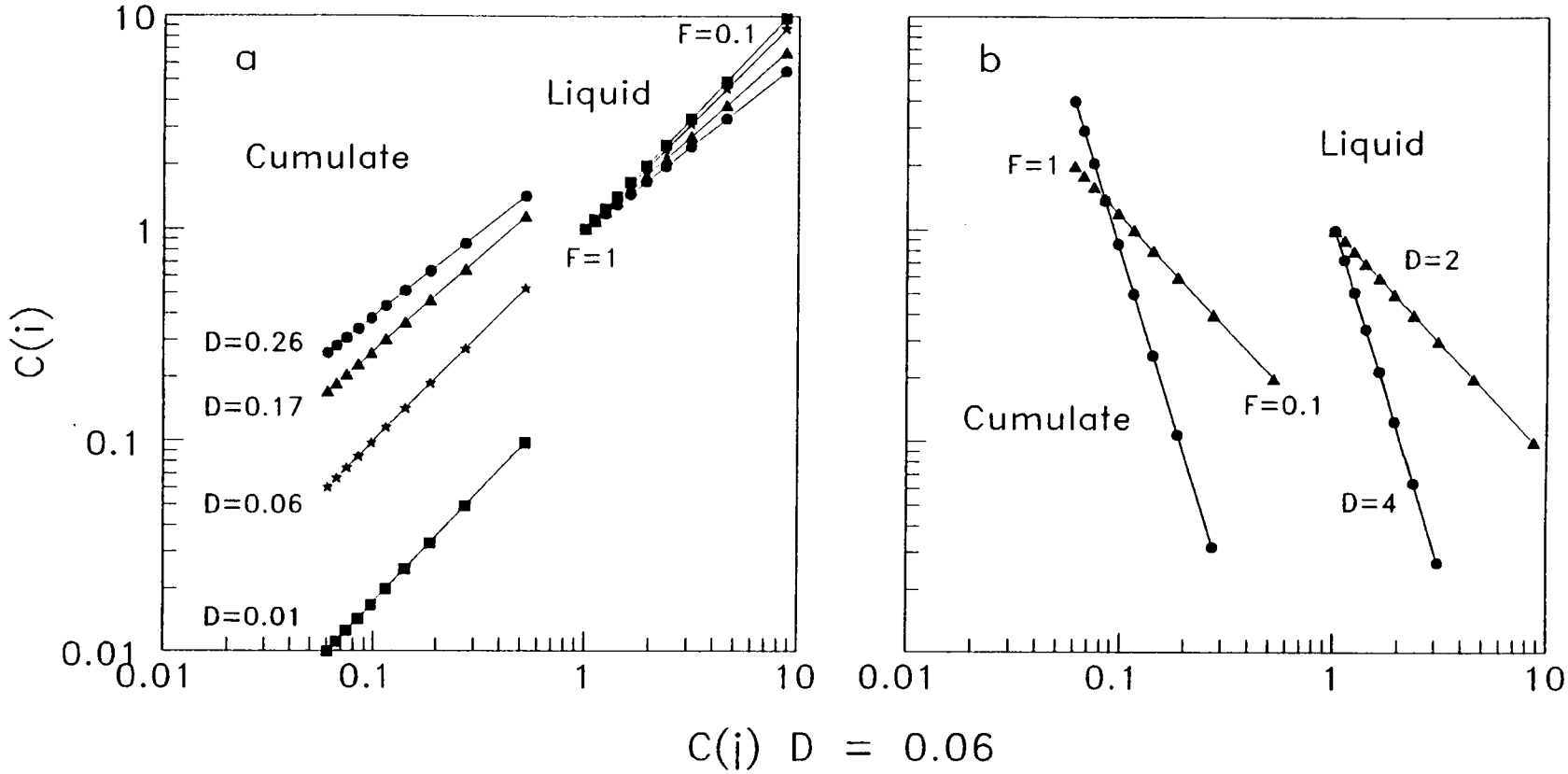

Figure 21. CFC model liquid and cumulate lines for an olivine gabbro cumulus assemblage. The abscissa represents the concentration of an element j with $\bar{D}_j$=0.06. The ordinate represents the concentration of element i. The type of symbol denotes the $\bar{D}_i$ value for which a line is drawn (cumulate lines labeled). The position of the symbol along a line denotes a value of F in increments of 0.1. Cumulate lines are at lower values of C_j, to the left of liquid lines. (a) Incompatible elements. (b) Compatible elements.

curve is drawn, and the position of the symbol along the curve denotes the value of F in increments of 0.1, beginning with 1 on the left and ending with 0.1 on the right. The cumulate trends are parallel to their respective residual liquid trends but are displaced from them by distances of log $\bar{D}_j$ and log $\bar{D}_i$ along the j and i axes, respectively, as expected from the analytical expressions given earlier. Again, this illustrates a general result and applies to curves for all models.

For incompatible elements neither the slopes nor the lengths of the CFC lines are sensitive to the exact values of $\bar{D}_i$ or $\bar{D}_j$ chosen to represent the elements. The insensitivity to $\bar{D}_i$ is evident from the near congruence of all the liquid lines in Figure 21a. Choosing a smaller $\bar{D}_j$ would slightly lengthen the curves parallel to the j axis and displace the cumulate curves farther from the liquid curves; choosing a larger value has the opposite effect. The model lines for compatible elements are more sensitive to $\bar{D}_i$ but are quite steep for any value much larger than 1. Note again that the absolute values of C_j and C_i on these log - log plots is not important. Only the lengths and the slopes of the lines and the relative positions of the liquid and cumulate curves matter, and the liquid-cumulate curve pairs can be translated anywhere in log - log space to represent concentrations at any level.

Cumulate with Trapped Intercumulus Liquid (CTL)

The effect on liquid and cumulate compositions of liquid trapped among the cumulus crystals, i.e. intercumulus liquid, has been discussed in the literature (Albarede, 1976; Allegre and Minster, 1978; Anderson and Greenland, 1969; Paster et al., 1974; Irvine, 1979). The following analysis is based primarily on aspects of the mathematical approaches of Anderson and Greenland (1969) and Albarede (1976). In the simplest model the cumulus phases in the solid are assumed to occur in the same ratios in which they crystallized from the liquid, and the trapped intercumulus liquid is treated as an additional cumulus phase with $\bar{D} = 1$; i.e. the trapped liquid is assumed to have the same composition as the residual liquid in equilibrium with the cumulus assemblage. Under these assumptions the cumulus crystal + trapped liquid assemblage has an effective bulk distribution coefficient ($\hat{D}$) of:

$$\hat{D} = (1 - k)\bar{D} + k(1), \qquad (4)$$

where k = weight fraction of trapped liquid.

Constant k

The net effect of trapped liquid is to decrease the efficiency of liquid fractionation as a function of F. For constant k, CFC curves for the residual liquid can be

constructed in the same way as outlined above using $\hat{D}$ rather than $\bar{D}$. However, it can be demonstrated that in the analytical expression for log C_i vs log C_j k divides out, and the equation is exactly the same as obtained using $\bar{D}$. Thus, liquid trapping does not change the relative concentrations of elements in the main body of liquid or in the cumulate if k is constant. This result is a special case and does not necessarily apply to models other than CFC.

Estimating Liquid Compositions

Trapped liquid does, however, significantly affect the position of the cumulate curve with respect to the liquid curve, even at constant k. Because the cumulus crystal + trapped liquid system has an effective bulk distribution coefficient of $\hat{D}$, the cumulate curve is displaced from the liquid curve by distances depending on $\hat{D}$ rather than $\bar{D}$. $\hat{D}$ is always larger than $\bar{D}$ for $\bar{D} < 1$ and smaller than $\bar{D}$ for $\bar{D} > 1$. This has important consequences for calculating liquid compositions from the composition of cumulate rocks with trapped liquid: calculating C^l by simply dividing the sample concentration by $\bar{D}$ will overestimate C^l for $\bar{D} < 1$ and underestimate C^l for $\bar{D} > 1$. The magnitude of these effects depends on both $\bar{D}$ and k; the ratio of the liquid composition calculated using $\bar{D}$ to the actual liquid concentration of an element is $\hat{D}/\bar{D}$. This ratio is largest for small $\bar{D}$ and large

k and can be very substantial, for example, 50 for $\bar{D} = 0.01$ and $k = 0.5$.

Trends Produced by Variable k (CTL Model Curves)

If k is variable, the relative concentrations of elements with different $\bar{D}$s in the cumulus crystal + trapped liquid system can be significantly different than those in the corresponding liquid. A simple way to see this is to calculate log C_i^c vs log C_j^c curves as a function of k at constant F. Variations in concentration then are due to variations in the amount of trapped intercumulus liquid, and the problem becomes one of mixing the residual liquid with a concentration of C^l with the equilibrium cumulate with a concentration of C^c. The equation describing concentrations in the cumulus crystal + trapped liquid system (C^{CTL}) is:

$$C^{CTL} = (1-k)\bar{D}C^l + kC^l,$$

which can be rearranged to:

$$C^{CTL} = [(1-k)\bar{D} + k)]C^l$$
$$= \hat{D}C^l. \qquad (5)$$

Figures 22a through 22d reproduce CFC liquid and cumulate lines shown in Figure 21 and, in addition, show the CTL mixing curves generated from Equation (5) for selected values of $\bar{D}_i$.

Figure 22. Selected CTL (filled symbols) and CFC (open symbols) model curves for an olivine gabbro cumulus assemblage. $\bar{D}_j = 0.06$. (a) $\bar{D}_i = 0.26$. (b) $\bar{D}_i = 0.01$. (c) $\bar{D}_i = 2$. (d) $\bar{D}_i = 4$.

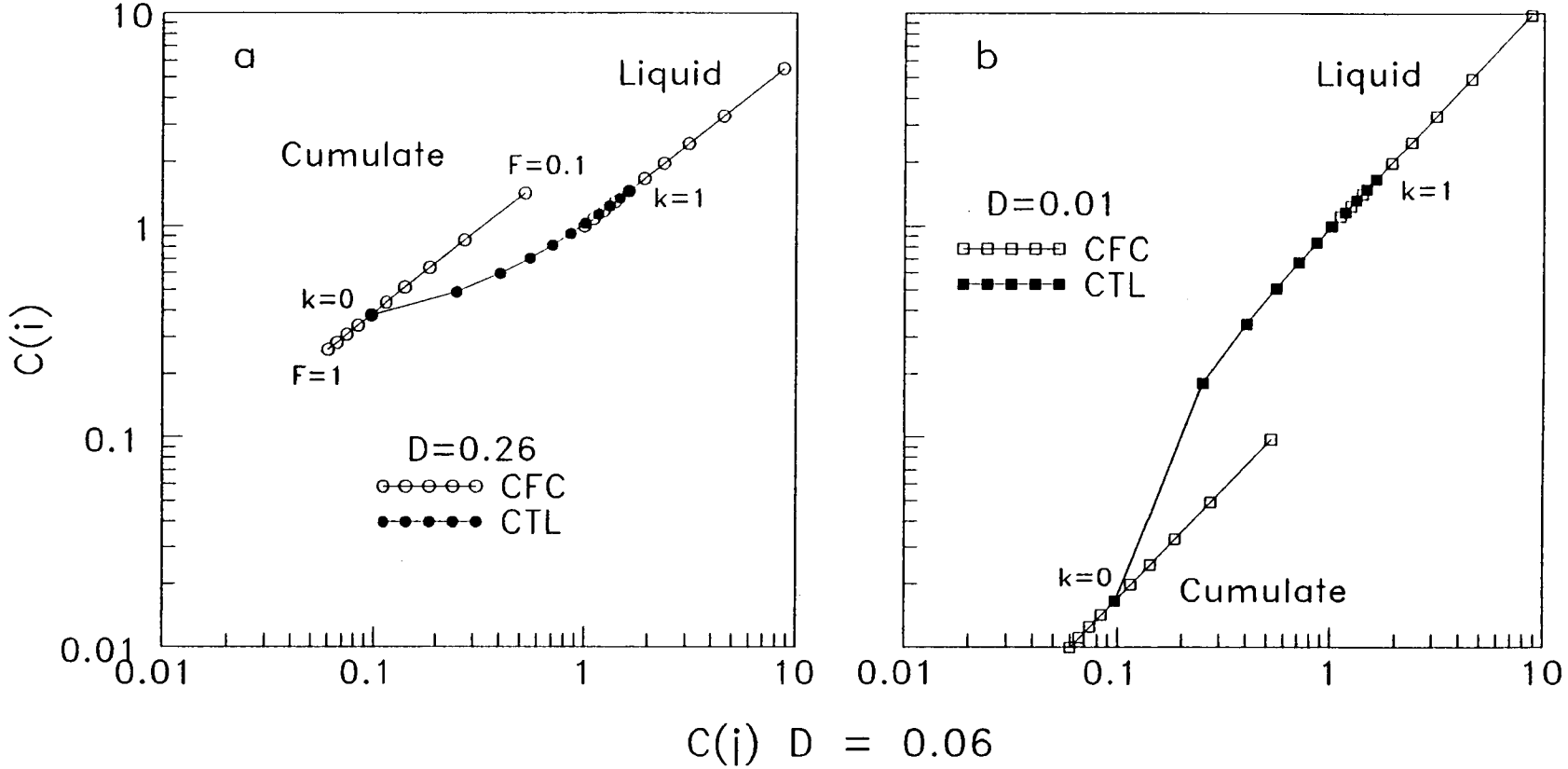
a
Liquid
Cumulate
F=0.1
k=1
k=0
F=1
D=0.26
CFC
CTL
C(i)
10
1
0.1
0.01
0.01
0.1
1
10
b
Liquid
D=0.01
CFC
CTL
k=1
k=0
Cumulate
0.01
0.1
1
10
C(j) D = 0.06

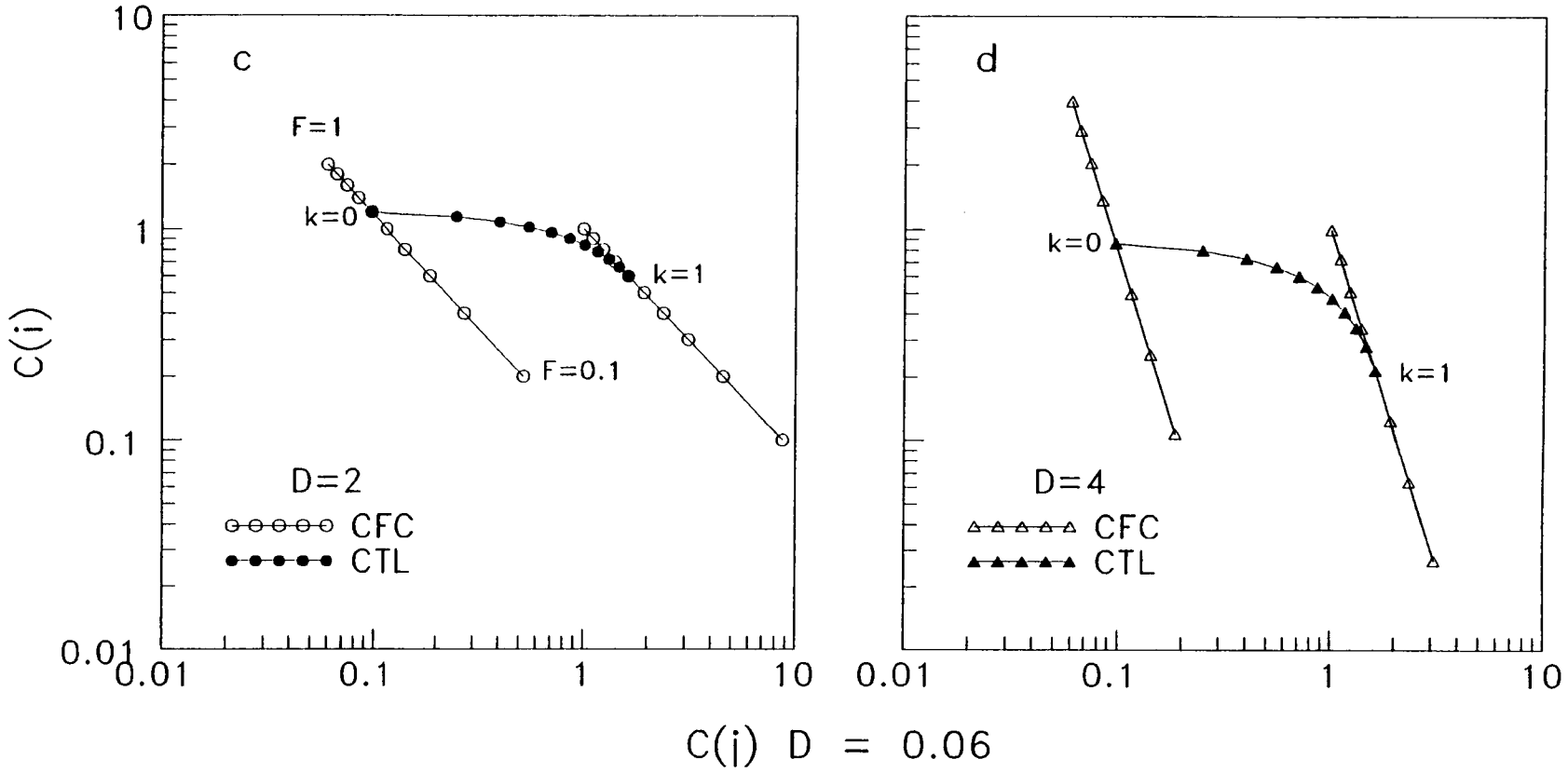
c
d
F=1
k=0
k=1
F=0.1
D=2
D=4
CFC
CTL
C(i)
C(j) D = 0.06
0.01
0.1
1
10

The CTL curves connect the cumulate lines to the liquid lines at equal values of F; the curves are drawn for F = 0.6, but they are the same for any F. The position of the symbol along the CTL curves represents a k value in increments of 0.1; k = 0 on the cumulate line, and k = 1 on the liquid line.

The CTL curves illustrate that varying amounts of trapped liquid can not only complicate the calculation of liquid compositions, but can also produce coherent trends in plutonic rocks, albeit different from CFC trends. The CTL curves for incompatible elements are less steep than the corresponding CFC lines ($k < 0.5$) for those elements with $\bar{D}_i > \bar{D}_j$ (Figure 22a) and more steep for those elements with $\bar{D}_i < \bar{D}_j$ (Figure 22b). For compatible elements the CTL curves for $k < 0.5$ are quite flat compared to the CFC lines (Figures 22c and 22d). For $\bar{D}_i = \bar{D}_j$ both CFC and CTL curves are lines with slopes of 1 (45^0). For both incompatible and compatible elements, neither the shapes nor the lengths of CTL curves are sensitive to the exact values of the distribution coefficients chosen as long as $\bar{D}_i$ and $\bar{D}_j$ are of the proper relative values.

Fractionation of Elements

The CTL process can fractionate elements with different $\bar{D}$s from each other more efficiently than CFC and can significantly alter element ratios in the cumulate from liquid values. This fractionation is evident in Figures 23a and 23b, which are plots of the ratio C_i/C_j versus C_j for incompatible

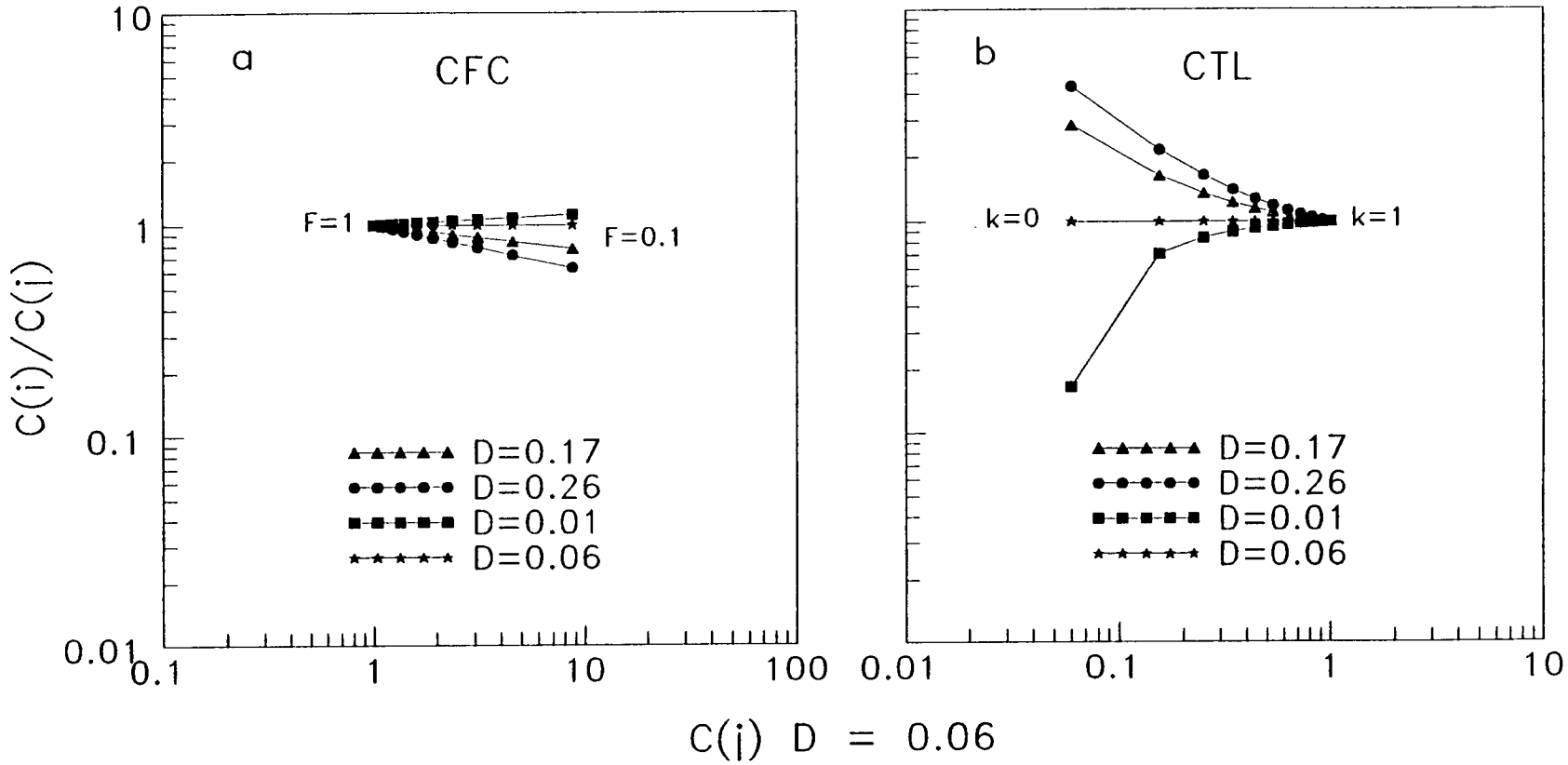

Figure 23. Model curves for the ratio C_i/C_j vs C_j for incompatible elements for an olivine gabbro cumulus assemblage. $\bar{D}_j = 0.06$, and $\bar{D}_i$s as indicated. (a) CFC curves at constant k. (b) CTL curves at constant F.

elements for CFC and CTL processes, respectively. C_i/C_j is not much different than one for any value of $\bar{D}_i$ or F for CFC, illustrating the well known fact that CFC is not a very efficient fractionator of such elements at any degree of crystallization. For CTL, however, C_i/C_j is quite large for small amounts of trapped liquid if $\bar{D}_i$ is different from $\bar{D}_j$. For CTL, increasing $\bar{D}_j$ decreases the fractionation factor for $\bar{D}_i > \bar{D}_j$, and increases the fractionation factor for $\bar{D}_i < \bar{D}_j$. Decreasing $\bar{D}_j$ has the opposite effect. Of course the curves must also change shape somewhat, although for small changes in $\bar{D}$s they retain the same general forms as shown.

Estimating k

Various ways of estimating k are discussed in the literature (Anderson and Greenland, 1969; Albarede, 1976; Paster et al., 1974). Most require texture and mineral preservation and an observable crystallization sequence. However, even in the absence of the second and with only moderately well preserved textures and mineralogy, if compositional data are available for both a relict igneous mineral with a known mineral/liquid partition coefficient and for the corresponding bulk rock, an idea of the amount of trapped liquid present can be obtained as follows. The expression for $\hat{D}$ (Equation 4) can be rearranged to give:

$$k = 1 - (\hat{D} - 1)/(\bar{D} - 1). \qquad (6)$$

$\bar{D}$ is calculated from the known or assumed modal mineralogy of the rock and published mineral/liquid partition coefficients. $\hat{D}$ is C^{CTL}/C^{l}, where C^{CTL} is the measured concentration of the element in the bulk rock, and C^{l} is the actual liquid concentration. What is needed then to calculate $\hat{D}$, and subsequently k, is an independent estimate of C^{l}. This can be obtained from microprobe data on the composition of an igneous mineral in the rock: $C^{l} = C^{p}/D^{p}$, where C^{p} and D^{p} are the concentration of the element in the mineral and the crystal/liquid partition coefficient for the mineral, respectively. In practice microprobe data are usually only available for FeO/MgO, which can be treated as an incompatible element with a partition coefficient of 0.26 (Irvine, 1979; Church and Riccio, 1977).

The implicit assumption here is that C^{l} calculated from the mineral composition is a better value than C^{l} calculated from the bulk rock. The bulk-rock data are essentially normalized to the mineral data. In addition to analytical errors in probe data, another potential problem with the above procedure is the possibility of mineral reequilibration. For example, if FeO/MgO for clinopyroxene has increased during cooling, k calculated as above should be considered a lower limit. In practice the procedure gives quite reasonable results, as will be demonstrated in Chapter V.

Combined Liquid Trapping and Fractionation

Liquid trapping and fractionation are both likely to contribute to changes in the chemical composition of plutonic rocks. To actually construct a model which treats these processes simultaneously it would be necessary to assume some relationship between the two, i.e. the percent of trapped liquid, k, increases or decreases as a function of the degree of fractionation, F. No such simple correlation seems to exist; however, it is possible to visualize some special cases. Fractionation at constant k and mixing at constant F have already been discussed. Beyond these two cases it is easy to see that if k generally increases with F, the result would be a trend with a less steep slope than expected from pure fractionation; and if k generally decreases with F, the result is a trend with a steeper slope. If k is variable but mostly uncorrelated with F, considerable scatter of the data would be expected.

Crystal Sorting

In all the models described so far, it has been assumed that the cumulus phases in the plutonic rock occur in the same proportions in which they precipitate from the liquid. In such cases, compositional data for all rocks, whether plutonic or volcanic, that are related to a given liquid trend must fall in the region defined by the CFC lines for the liquid and

the cumulate and the CTL curves for values of F between 1 and approximately 0.5. If precipitating crystals segregate from each other in the solid, i.e. one or more minerals accumulate in excess of eutectic proportions, the composition of the resultant cumulate rock is no longer constrained to fall between the cumulate and liquid curves. In addition, because the observed modal mineralogy of such a rock does not represent the assemblage which was in equilibrium with the liquid at the time of crystallization, it is not possible to calculate a valid $\bar{D}$ for elements affected by the process from the observed mode.

Early work on layered mafic intrusions suggested that crystal sorting by gravitational settling, flotation or, in some cases, deposition by convection currents was an important process in the formation of cumulate rocks (e.g. Wager and Brown, 1967). However, more recent studies (e.g. Irvine, 1979) proposed that many cumulate rocks, especially in smaller intrusions, are formed by in-situ crystallization, suggesting that considering cumulate rocks as equilibrium assemblages may often be a valid supposition. Unfortunately, unless primary textures are well preserved it is difficult to confirm the presence or absence of crystal sorting petrographically.

However, crystal sorting can sometimes be inferred from bulk-rock compositional data. For example, ranges in rock compositions that are uncorrelatable with fractionation or liquid trapping but are consistent with the addition of

particular phases to an equilibrium assemblage would suggest the influence of crystal sorting. Patterns of element correlations can be used as additional evidence for crystal sorting, e.g. positive FeO/MgO - TiO_2 correlations without corresponding Zr correlations.

Limits can be placed on the distances by which samples affected by crystal sorting can be expected to fall outside of the fractionation curves. At constant F, the problem is equivalent to contamination with the phase in question and involves only a simple mixing calculation of the phase p with the equilibrium cumulus assemblage (with or without trapped liquid). The concentration of an element in a rock consisting of an equilibrium cumulus assemblage plus an excess weight fraction, α, of phase p (C^{c+p}) is:

$$C^{c+p} = (1 - \alpha)C^c + \alpha C^p.$$

If this equation is rearranged to express C^{c+p} in terms of C^c we obtain:

$$C^{c+p}/C^c = (1 - \alpha) + \alpha C^p/C^c. \qquad (7)$$

Figure 24 shows an example of a mixing curve generated from Equation (7) superimposed on the CFC and CTL curves appropriate for a plot of TiO_2 versus Zr. The positions of

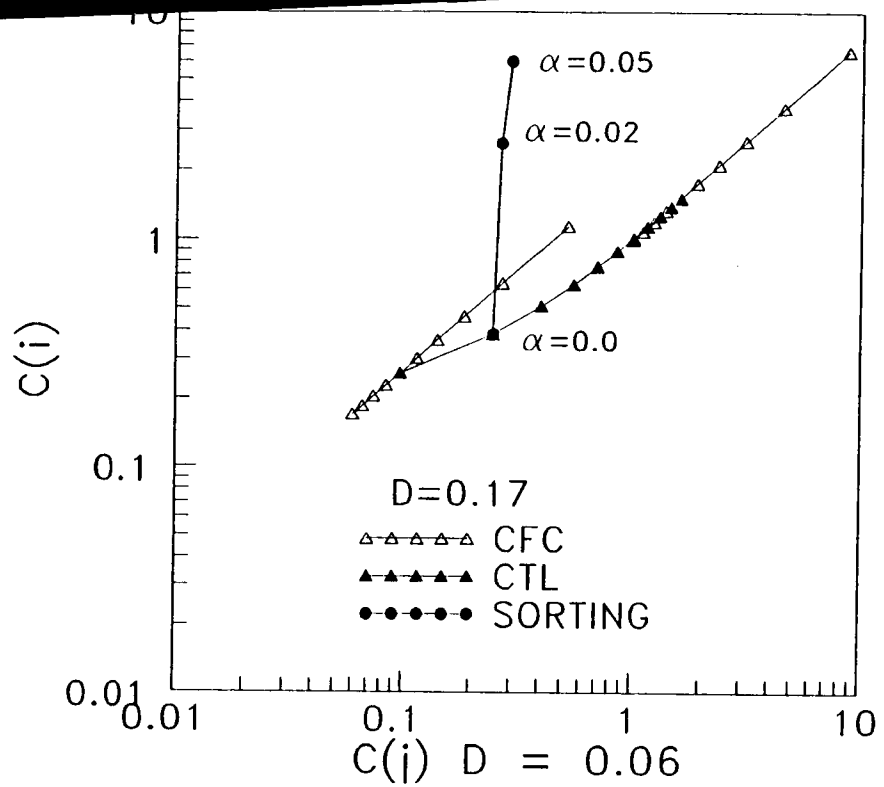

Figure 24. Crystal sorting curve (filled circles) superimposed on CTL and CFC curves for $\bar{D}_j = 0.06$ and $\bar{D}_i = 0.17$. $D_i^p = 50$, and $D_j^p = 0.28$. Positions of filled circles represent values of α: $\alpha = 0$ on CTL curve, 0.02 and 0.05.

the symbols represent $\alpha = 0$, on the CTL curve, $\alpha = 0.02$ and $\alpha = 0.05$. In this example C_i^p/C_i^c (50) is much larger than C_j^p/C_j^c (1.6), and a near vertical curve results. This case could represent the accumulation of a TiO_2-rich phase such as ilmenite. The situation is symmetrical, and if C_i^p/C_i^c is much smaller than C_j^p/C_j^c, a near horizontal curve results. Note that any case of contamination of a cumulate, e.g. diffusion from the country rock or metasomatism, can be treated as above.

If the composition of the phase in excess is known or can be estimated, the mixing calculation gives the weight percent of the phase which must be added to reproduce the observed data at constant F. This result can be checked petrographically. Conversely, the composition of the phase in excess can be estimated from the data and compared to expected mineral compositions.

Usually the trace element composition of a mineral is not known; however, the ratio of C^p to C^c can be estimated from the D^ps of the phases involved using the following relationships:

$$\bar{D} = C^c/C^l,$$

$$D^p = C^p/C^l, \text{ and}$$

$$C^p/C^c = D^p/\bar{D}.$$

Thus a sample containing all phase p rather than the eutectic percentage of phase p will have a weight percent of element i which is $D_i^p/\bar{D}_i$ times that of the equilibrium assemblage at the

same degree of crystallization. This places an upper or a lower limit on the permissible composition, with respect to the assumed equilibrium cumulate composition, of a rock whose composition is controlled by crystal sorting. This ratio can also be used in Equation (7) to generate curves on two-element variation diagrams. However, estimating C^p/C^c in this way requires the division of two distribution coefficients, each with a large uncertainty, so the estimate must be regarded as quite crude. The results can be checked for rough consistency with petrography. Ideally, if trapped liquid is present, $\hat{D}$ should replace $\bar{D}$.

Combined Crystal Sorting and Fractionation

This situation is analogous to the one encountered in liquid trapping: to construct a model for simultaneous crystal sorting and fractionation it is necessary to assume a functional relationship between the two when there is little justification for doing so. It is again, however, possible to visualize some special cases. The case for variable α and constant F has already been discussed. Trends for fractionation accompanied by crystal sorting at constant α (constant α, variable F) are simply displaced from CFC trends by distances proportional to α and C^p/C^c. By iterative methods it would be possible to construct any number of other special cases and a great variety of curves by varying both α and F in definite ways. However, given the usual paucity of

constraints in any data set, it is probably sufficient to view the resultant curves as approximate vector sums of the sorting and fractionation trends.

Open-System Fractional Crystallization (OFC)

Many magma chambers are in reality likely to be open systems at some point in their evolution, with possible mass inputs from assimilation of the country rocks and from replenishment of liquid to the chamber, and mass losses from eruption of liquid. O'Hara (1977) first outlined the effects to be expected in open systems undergoing fractional crystallization, and O'Hara and Mathews (1981) derived iterative equations describing such systems and examined several special cases. DePaolo (1981) derived a continuous expression for fractional crystallization with the simultaneous addition of material. The problems which he specifically addressed are the assimilation of wall rock or the recharging of a magma chamber during crystallization; the discussion which follows applies to either. Because it is much easier to handle than iterative equations in the spreadsheet approach adopted here, DePaolo's formulation, which is usually referred to as the AFC model, is used in this work. The assumptions which apply to AFC are: the cumulus crystals are only momentarily in equilibrium with the liquid and is subsequently isolated from it; $\bar{D}$ for the system is

constant; and the mass per unit time of the mass added is a constant factor of the mass per unit time of the mass crystallized. This last constraint is necessary to obtain a closed-form solution of the basic mass-balance equation. DePaolo shows that the equation describing the liquid evolution curve is then:

$$C^l/C^{l,0} = F^{-z} + (r/r - 1)(C^a/C^{l,0}z)(1 - F^{-z}), \qquad (8)$$

where

C^l = wt% of an element in the residual liquid,

$C^{l,0}$ = wt% of an element in the original liquid,

C^a = wt% of an element in the added material,

F = weight fraction of residual liquid, and

$z = (r + \bar{D} - 1)/(r - 1)$,

in which

$\bar{D}$ = bulk distribution coefficient, and

r = mass per unit time of material added/mass per unit time of material crystallized.

By definition, the instantaneous cumulate evolution curve is still given by $C^c = \bar{D}C^l$, and even in this more complex model the cumulate curve is a replica of the liquid curve but is displaced from it by a distance of $\bar{D}$ on a log - log plot. In the following paragraphs then, the model curves described can be taken to represent either the liquid evolution curve or the instantaneous cumulate evolution curve.

If either r or C^a is zero in Equation (8), the expression reduces to Equation (1) for closed-system fractional crystallization. Not much more about the behavior of C^l (or C^c) is apparent from inspection of Equation (8), and mappings onto log C_i vs log C_j graphs are virtually impossible to visualize. Therefore, examples of computer-generated log C_i vs log C_j curves are presented for selected combinations of the parameters $C_i^a/C_i^{l,0}$, $C_j^a/C_j^{l,0}$, $\bar{D}_i$, $\bar{D}_j$ and r to gain some insight into how these parameters affect concentration levels and ratios. There are obviously very many possible combinations of parameters for AFC models. Thus choices of parameters need to be limited either by physical arguments or by comparisons with the actual data that are being analyzed.

For assimilation models three parameters, in addition to F and k, need to be constrained: r, $C_i^a/C_i^{l,0}$, and $C_j^a/C_j^{l,0}$. Reasonable values of r are limited by the initial temperature, the melting point, the latent heat and the specific heat of the rock being assimilated, and the latent heat of the cumulus assemblage. Using these variables, Taylor (1980) showed that for cold country rock r would have to be approximately 0.3 or less. However, if the temperature of rock being assimilated is near its melting temperature, e.g. in the deep continental crust, r can be close to 1. If AFC is to be considered a possible process, curves using the same r must, of course, explain the observed trends for all elements. While there is, in principle, no limit on the value of r in the liquid

recharge case, Equation (8) behaves erratically for r greater than 1, giving negative concentrations in some cases.

There is a wide variety of possible compositions of assimilated or recharge material as represented by the $C^a/C^{l,0}$s. However, some limits can be placed on reasonable compositions from known ranges of concentrations of elements in crustal rocks and magmas. Again, if AFC is to be considered a convincing explanation for the data, compositions of assimilated material must be consistent for all elements.

Figures 25a, 25b and 25c illustrate a basis for further constraining the values of $C_i^a/C_i^{l,0}$ and $C_j^a/C_j^{l,0}$. These figures show model curves constructed for several values of $\bar{D}_i < 1$ at constant $\bar{D}_j$ and constant r for possible relative values of $C_i^a/C_i^{l,0}$ and $C_j^a/C_j^{l,0}$. Selected CFC lines are also plotted for comparison. All the curves illustrate the main effects of open-system fractional crystallization: incompatible elements can be enriched in the residual liquid and elements with different $\bar{D}$s can be fractionated to extents beyond those possible in closed systems (cf. Figure 2 and the discussion in DePaolo, 1981).

The focus here, however, is on the shapes of the curves in log C_i - log C_j space. There are two things to notice from the three figures. First, for small $\bar{D}_i$, $C_i^a/C_i^{l,0}$ must be significantly different from $C_j^a/C_j^{l,0}$ to make the slopes of AFC curves deviate substantially from CFC curves. This fact remains true for other choices of r and the $C^a/C^{l,0}$s. Second,

Figure 25. AFC model cumulate or liquid curves for an olivine gabbro cumulus assemblage (filled symbols) and selected CFC lines (open symbols) for comparison. $r = 0.2$, $\bar{D}_j = 0.06$, and symbols for $\bar{D}_i$s as in previous figures (selected curves labeled). (a) $C_i^a/C_i^{l,0} = 10$ and $C_j^a/C_j^{l,0} = 10$. (b) $C_i^a/C_i^{l,0} = 1$ and $C_j^a/C_j^{l,0} = 10$. (c) $C_i^a/C_i^{l,0} = 10$ and $C_j^a/C_j^{l,0} = 1$. (d) $C_i^a/C_i^{l,0} = 10$ and $C_j^a/C_j^{l,0} = 1$.

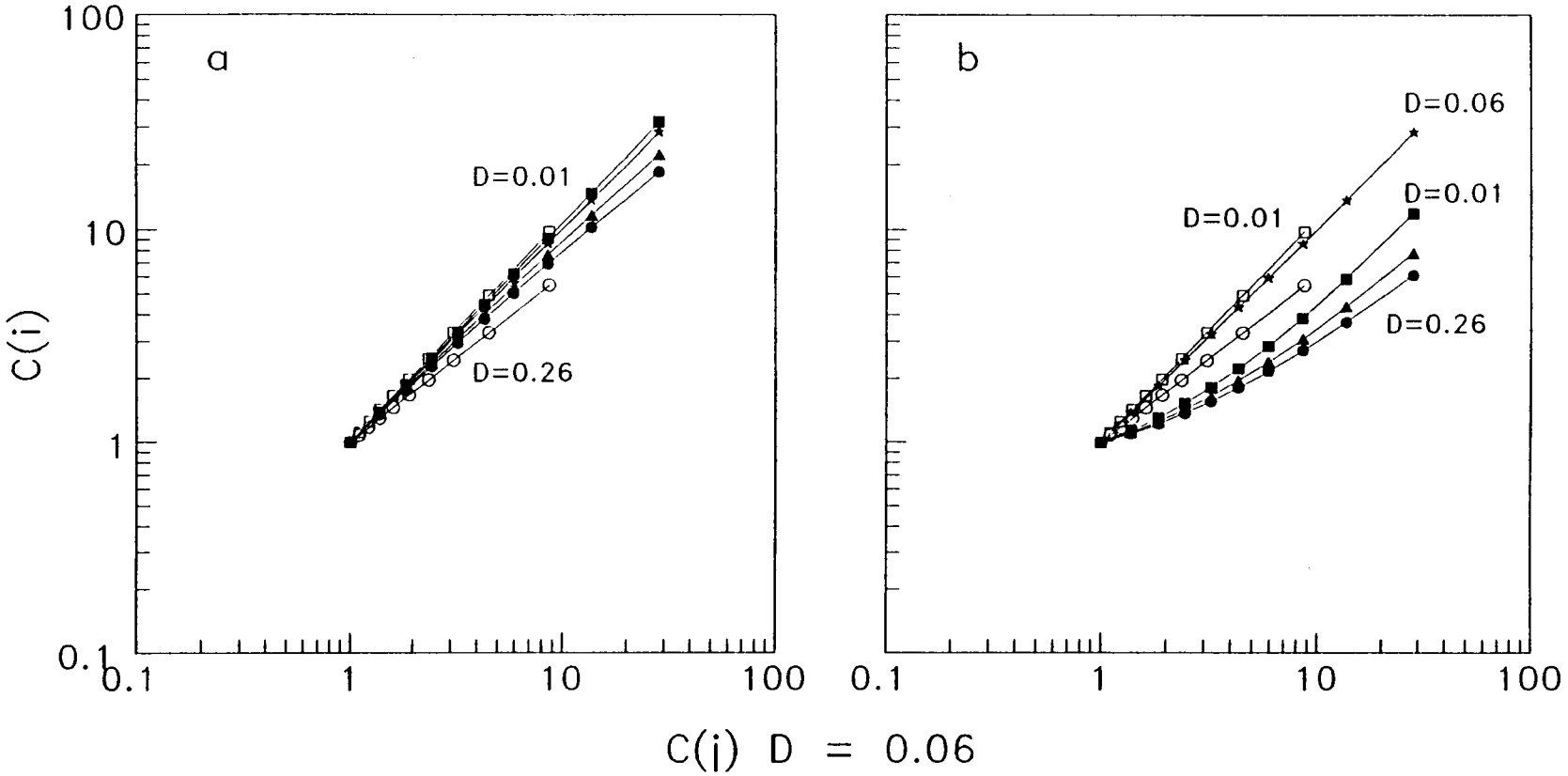
a
b
C(i)
C(j) D = 0.06
D=0.01
D=0.26
D=0.06
D=0.01
D=0.01
D=0.26
100
10
1
0.1
0.1
1
10
100

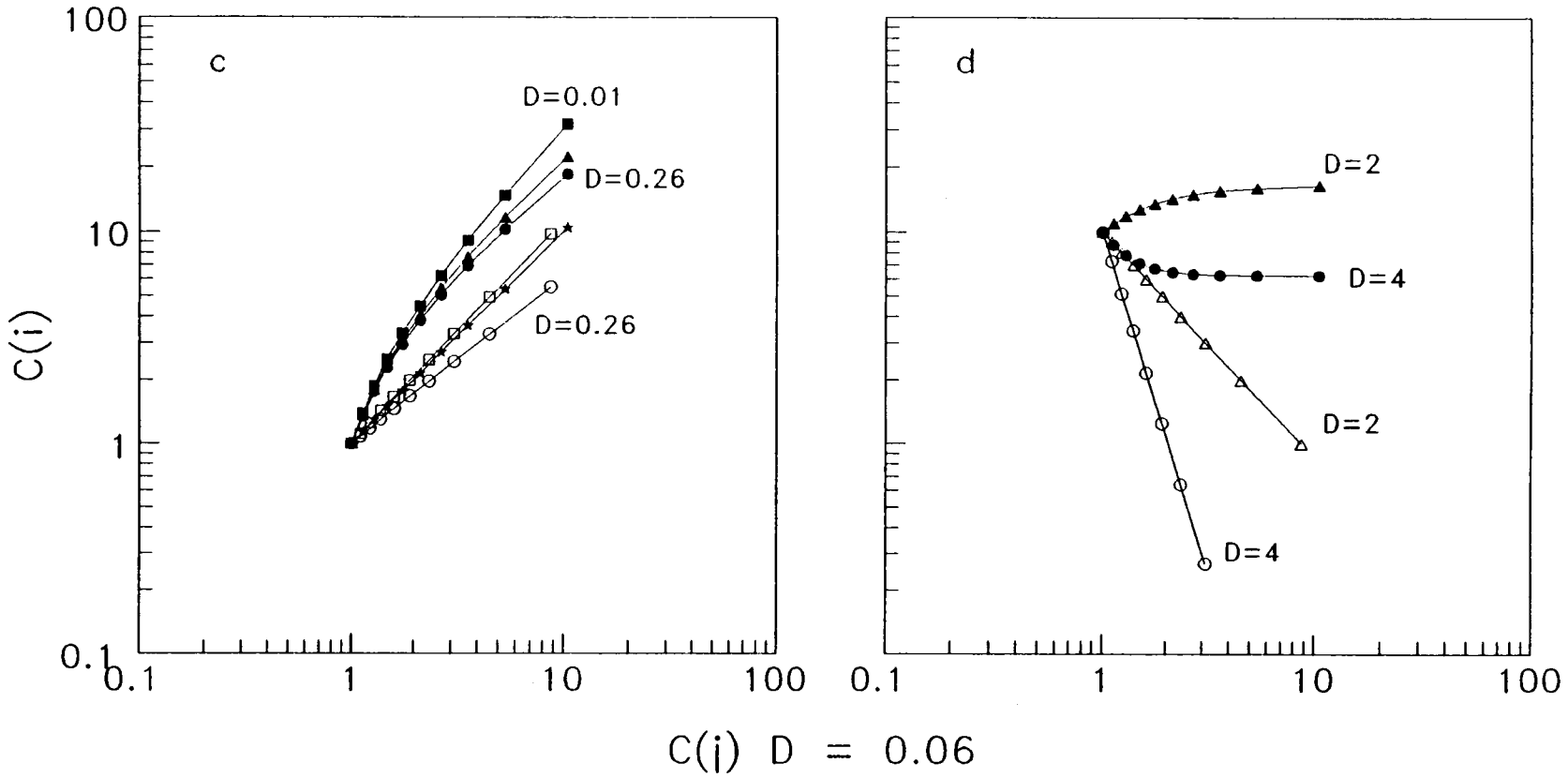
c
d
C(i)
D=0.01
D=0.26
D=0.26
D=2
D=4
D=2
D=4
100
10
1
0.1
0.1
1
10
100
C(j) D = 0.06

the shapes of the curves depend on the relative magnitudes of $C_i^a/C_i^{l,0}$ and $C_j^a/C_j^{l,0}$: for $C_i^a/C_i^{l,0} < C_j^a/C_j^{l,0}$ the model curves for all $\bar{D}_i < 1$ are concave upward (Figure 25b); and for $C_i^a/C_i^{l,0} > C_j^a/C_j^{l,0}$ they are concave downward (Figure 25c). The curve for $\bar{D}_i = \bar{D}_j$ is always a line at 45^0. The sense of curvature of the observed trend to be explained can, therefore, guide one to the choice of model curves with a given type of curvature and relative $C^a/C^{l,0}$s. The following paragraphs discuss some other properties of AFC model curves with reference to the concave-down subset of curves.

Figure 25d shows AFC curves constructed for selected values of $\bar{D} > 1$. These curves are very different than CFC lines and reach steady state values at small F. Some AFC curves for compatible elements are rather surprising in that they show positive trends for even highly compatible elements at large F for certain choices of $\bar{D}_i$, r and $C_i^a/_i^{l,0}$.

The ratio of the concentration of an element in the assimilated material to that in the original liquid and r are the dominant factors in determining the shapes and lengths of AFC curves. For example, for curves that are concave down, the general tendency is for the slopes of the curves to increase with either increasing $C_i^a/C_i^{l,0}$ or r, but the exact shape of the curve depends on the actual parameters chosen. If $C_i^a/C_i^{l,0}$ is increased, the lengths of the curves are increased in the i direction only, and the net effect is a pronounced steepening of the curves. If r is increased, the lengths of

the curves are increased in both the i and the j directions. The result is still a steepening of the curves, but these curves have more curvature at large F. The curves for $\bar{D}_i > 1$ behave basically the same way as the curves for $\bar{D}_i < 1$: they tend to steepen with increases in either r or $C_i^s/C_i^{l,0}$, turning over more quickly with r than with $C_i^s/C_i^{l,0}$.

As long as $C_j^s/C_j^{l,0}$ is much smaller than $C_i^s/C_i^{l,0}$ and the range of $\bar{D}_j$ is not too great, the actual choice of these parameters does not significantly affect the lengths or shapes of the model curves. The effects of changes in $\bar{D}_j$ and $C_j^s/C_j^{l,0}$ can be summarized as follows: an increase or decrease in the value of $\bar{D}_j$, respectively, decreases or increases the length of the curves in the j direction, and small increases or decreases in $C_j^s/C_j^{l,0}$ produce correspondingly small increases or decreases in the length of the curves in the j direction. These changes in length, of course, affect the shapes of the curves. The size of these effects can be evaluated for individual cases.

Additional Processes

As discussed in an earlier section, in closed-system models a constant percentage of trapped liquid does not change the slope or the lengths of either the liquid or the cumulate trend on log C_i vs log C_j plots. This conclusion is not true for AFC models. The net effect of trapped liquid in the system is to decrease the efficiency of fractionation of both elements i and j, shortening the curves in both directions.

However, an element that is enriched in the assimilated material is not affected as strongly as an element that is not enriched, and the curves tend to change shape as well as shorten. These effects are negligible for small k (~ 0.1) but are more pronounced as k approaches 0.5.

Liquid trapping at constant F and variable k is handled the same way it is in the CFC case, but with C^l and C^c calculated from Equation (8). Likewise, crystal sorting or diffusion from the country rock are modeled with mixing calculations as shown earlier.

CHAPTER V

PETROGENETIC MODELS FOR THE MAFIC SUITES

Introduction

In this chapter the results from the analyses of immobile trace- and minor-element data from the five suites of rocks described in Chapters II and III, using the model curves and parameter estimation methods developed in Chapter IV, are presented. The results of these analyses allow one to understand the processes responsible for the compositional trends observed in the data and to deduce relationships among the five suites. In addition, in some cases approximate liquid compositions can be inferred from the analyses, and judgments made on probable provenances for the suites.

Observed trends in the suites were compared to model curves and a judgement made on the process or processes most likely to have been responsible for the trends. Because the association in the field of the amphibolites with cumulate lithologies, relict igneous textures and major-element chemistries indicate that the element distribution patterns observed in the five suites are almost certainly a result of processes associated with crystal fractionation rather than partial melting, the types of trends resulting from partial melting processes were not considered. Processes that were

considered are: closed-system fractional crystallization (CFC), open-system fractional crystallization as represented by DePaolo's model (AFC), liquid trapping (CTL), and crystal sorting. The possible effects of secondary processes such as metamorphic differentiation and diffusion from the country rock are also discussed.

Models for the Chunky Gal Mountain, Isolated and Kimsey Bald Amphibolites

Introduction

Because they exhibit good correlations and little scatter, the Chunky Gal Mountain trace- and minor-element data best lend themselves to quantitative treatment. The approach taken in this section is to find the model curves that explain the Chunky Gal Mountain data and then argue that, because of the similarity of their compositions and trends, the majority of the isolated amphibolites and Kimsey Bald amphibolites are genetically related to the Chunky Gal Mountain rocks and were affected by the same processes. In particular, it is shown in this section that closed-system fractional crystallization alone cannot explain many observed element correlations, but that cumulate plus trapped liquid curves are consistent with the data and imply reasonable and consistent values for the relevant parameters.

It was also possible to reproduce the data trends with the AFC model assuming a shale-like composition for the assimilated material, but only for values of r in the range of 0.7 to 0.8, which implies fractionation at great depth. There are two lines of evidence which strongly argue against an AFC process being responsible for the observed trends. First, the AFC fits imply that the trends represent liquid compositions (see below); this fact is not consistent with slow cooling at depth as implied by the large value of r required to fit the data, nor is it consistent with the fact that major-element chemistry implies many of the rocks are cumulates. Second, the limited available isotope data for these rocks (Shaw and Wasserburg, 1984; Jones et al., 1973) show no evidence of crustal assimilation.

Chunky Gal Mountain

Closed-System Fractional Crystallization (CFC)

Before the Chunky Gal Mountain amphibolite data are compared to the CFC curves, it should be noted that the observed trends cannot represent the evolution of an eutectic cumulate (including an AFC cumulate). Calculating the composition of the liquid that would be in equilibrium with such a cumulate proves this point. For example, the highest measured Zr and P_2O_5 concentrations are 138 ppm and 0.3%, respectively. For an equilibrium olivine + clinopyroxene +

plagioclase assemblage, $\bar{D}_{Zr}$= 0.06 and $\bar{D}_{P2O5}$ = 0.01 (Table 4). By definition, the liquid in equilibrium with these samples would have had a Zr concentration of 2300 ppm and a P_2O_5 concentration of 30%, clearly unreasonable results. If CFC is to be used as an explanation of the Chunky Gal Mountain trends, the trends must represent primarily liquid compositions, which, as has been argued earlier, seems unlikely based on major-element chemistry and field relations.

Furthermore, origin from a liquid undergoing closed-system fractional crystallization can be ruled out as an explanation for the Chunky Gal Mountain amphibolite data both on the basis of the overall lengths of the trends and because of the slopes of the trends for several elements. These points can be seen by comparison of the data with CFC model curves (Figure 26). The CFC curves are drawn for $\bar{D}$s appropriate for an eutectic olivine gabbro cumulus assemblage, but the conclusions discussed in the following paragraphs do not depend on the exact values of the $\bar{D}$s chosen. First, the lengths of the trends imply between 70% and 80% fractionation (F = 0.3 to 0.2); this small a value for F is not consistent with the mafic nature of the Chunky Gal Mountain suite. Even if this small a value for F were permissible, the slopes of the trends for several elements are not consistent with CFC. The most obvious cases are shown in Figure 26 and discussed in the following paragraphs: these are Y, for which the slope of the data trend is much too shallow compared to CFC curves;

Figure 26. Chunky Gal Mountain Complex data for selected elements plotted against Zr with linear regression lines fit to the amphibolite data. CFC model lines for an olivine gabbro cumulus assemblage are superimposed on the data for comparison (filled symbols). Lithologic symbols as in previous figures, and D_is as indicated. (a) Y. (b) P_2O_5. (c) Ni.

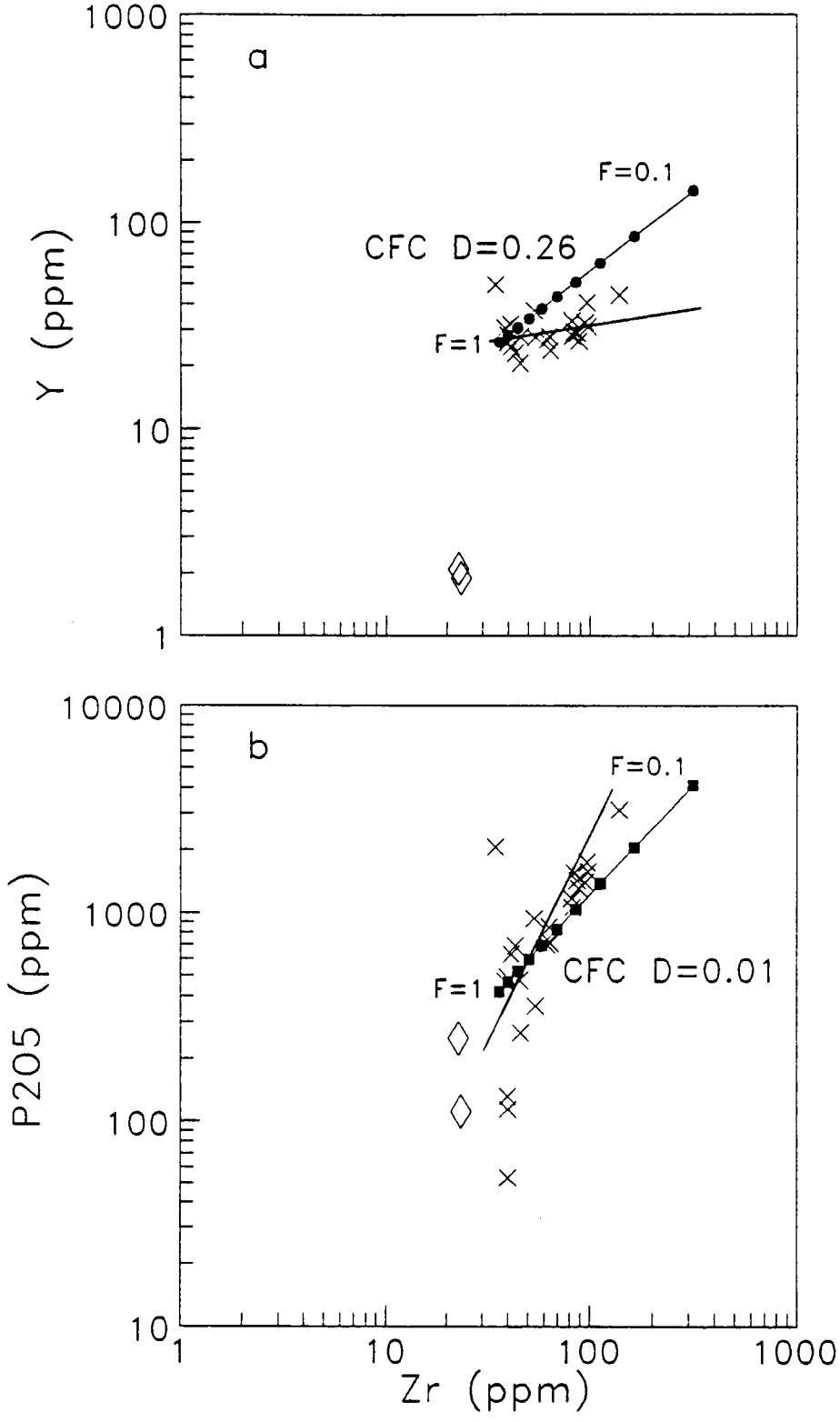
a
1000
100
10
1
Y (ppm)
F=0.1
CFC D=0.26
F=1
b
10000
1000
100
10
P205 (ppm)
F=0.1
F=1
CFC D=0.01
1
10
100
1000
Zr (ppm)

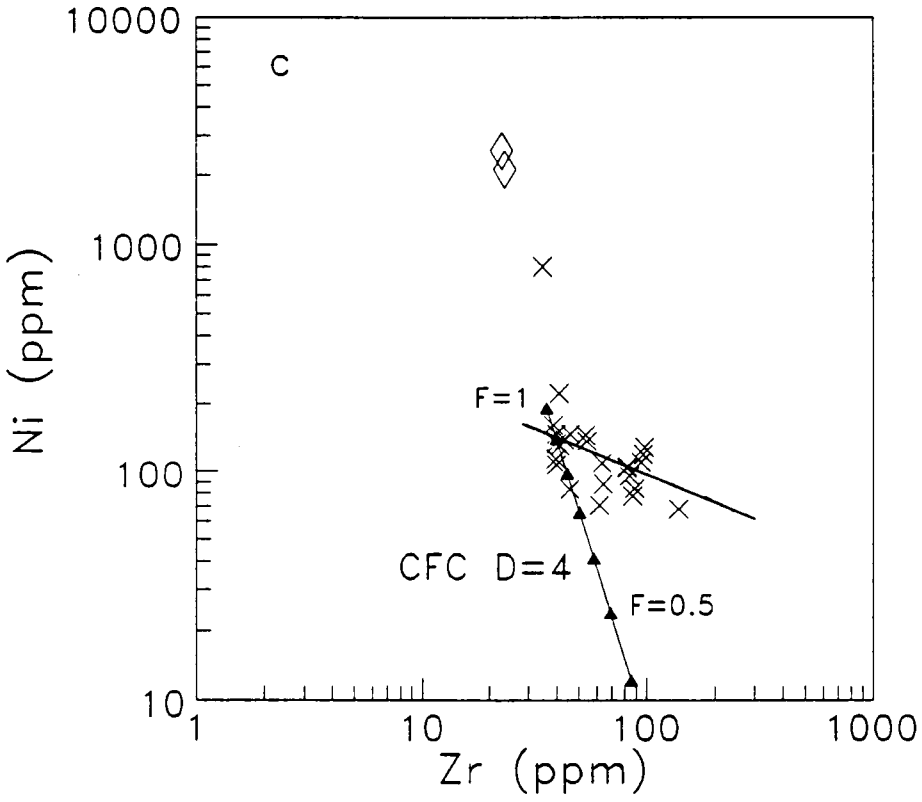
10000
1000
100
10
Ni (ppm)
c
F=1
CFC D=4
F=0.5
1
10
100
1000
Zr (ppm)

P_2O_5, for which the slope is too steep; and Ni, for which the slope also appears to be too shallow.

For Y, the plot of log Y against log Zr (Figure 26a) is essentially flat with a suggestion of negative curvature. Although the correlation coefficient is not significant, a regression line gives a slope of 0.15 or 9 degrees. The CFC line for eutectic proportions of clinopyroxene + olivine + plagioclase shown superimposed on the data is much too steep to fit the Y data (regression line slope = 0.79 or 38^0). Nor could the data trend be reproduced by any combination of major elements commonly on the liquidus of a mafic magma. The flattest trend that could be produced by a CFC process involving only major elements would result from the fractionation of clinopyroxene alone. Bulk distribution coefficients for Zr and Y would then be about 0.1 and 0.5, respectively (Table 3), and the slope of the trend would be 0.56 or 30^0 (Equation 3), which is still much greater than the observed slope. In the concentration range of the amphibolite data error bars for Y are about the same size as to less than the size of the data symbols on this log - log plot (standard error of calibration = 4 ppm). For Zr the standard error of calibration is 20 ppm, giving minimum error bars about 2 to 3 times the size of the symbols at low Zr values and smaller than the size of the symbols at high Zr values. Probable errors are thus much less than would account for the discrepancy between the CFC model lines and the data trend.

Crystallization of accessory minerals could possibly reduce the slope of the model CFC Y-Zr curve by the amount required to fit the data. The only accessory with a significant affinity for Y in basic liquids at crustal pressures is apatite. No data for apatite/liquid partition coefficients for Y were found in the literature; however, Y behaves geochemically like a heavy rare earth element (Cox, Bell and Pankhurst, 1979; Henderson, 1984), and its partitioning behavior can be predicted by available data for rare earths. These data suggest that apatite/liquid partition coefficients for Y are in the range of 2 to 3 (Irving, 1978; Watson and Green, 1981). A simple calculation can be performed to assess the minimum weight fraction of the cumulus assemblage which must be apatite if closed-system fractional crystallization is responsible for the observed Y-Zr pattern. From Equation (3) in Chapter IV, the $\bar{D}_Y$ which gives the observed slope m is:

$$\bar{D}_Y = m(\bar{D}_{Zr} - 1) + 1.$$

From this equation, using $m = 0.15$ and $\bar{D}_{Zr} = 0.06$, D_Y must be equal to approximately 0.86. Using an apatite/liquid partition coefficient of 3, to minimize calculated apatite, and the primary phase bulk distribution coefficient for Y from Table 4, the weight fraction of apatite (F_{ap}) necessary to

reproduce the observed slope is approximately:

$$3(F_{ap}) + 0.26(1 - F_{ap}) = 0.86$$

or

$$F_{ap} = 0.22.$$

Even this lower limit is a rather implausible amount of apatite for a mafic rock, implying that crystallization of apatite cannot explain the flat Y trend. The Chunky Gal Mountain data for Y thus cannot be explained by CFC alone.

The argument which proves that CFC is not an valid explanation for the P_2O_5 trend is quite simple. From the equation for CFC (Equation 3) it can be seen that the maximum slope of the linear trend for even a highly incompatible element for CFC is about 45^0. The trend for P_2O_5 (Figure 26b) is much steeper than this (regression line slope = 2.4 or 67^0) and shows a pronounced positive curvature; it is clearly inconsistent with CFC. Exclusion of the five samples with the lowest concentrations of P_2O_5 from the analysis does not significantly affect the linear regression fit to the data. Error bars in the concentration range of the remaining amphibolite data are larger than the size of the data symbols only at the lower end of the trend (standard error of calibration = 300 ppm).

The slope of the Chunky Gal Mountain data trend for the compatible element Ni also appears to be much too shallow to

be consistent with CFC. Figure 26c shows a comparison with CFC curves using $\bar{D}_{Ni}$ of 4 calculated from the average olivine and pyroxene partition coefficients. Because the Ni partition coefficients for clinopyroxene and, especially, for olivine are strongly temperature- and composition-dependent, and reported values span a broad range (Table 3), it is not possible to "prove" that CFC could not be an explanation for the Ni data. However, the slope of the data trend is only 0.43, and a calculation like that shown above for Y indicates that to reproduce the Ni data with a CFC model curve would require a combined clinopyroxene-olivine partition coefficient of about 2, which implies partition coefficients at the lower limits of the ranges for both phases. These lower limits are associated with very high temperatures and unusually magnesian compositions (Irvine, 1978), and it would, therefore, be necessary to assume very special conditions to fit the data. In summary then, both the extent of crystallization implied by the lengths of the data trends and the slopes of the trends of some elements rule out simple CFC as an explanation for the Chunky Gal Mountain data.

Cumulate plus Trapped Liquid Model (CTL)

The CTL curves derived in Chapter IV show that mixing varying amounts of residual liquid with an equilibrium cumulus assemblage produces exactly the kinds of effects described above. Permissible ranges of element concentrations, as

represented by the lengths of the curves, are greater than those for CFC, and fractionation of elements with different $\bar{D}$s, as indicated by the slopes of the curves (in the relevant range of $k < 0.5$), is larger than for CFC. On two-element diagrams with Zr as the abscissa, the slopes of curves for incompatible elements with $\bar{D}$s larger than $\bar{D}_{Zr}$ (e.g. Y) are depressed with respect to CFC lines, and the slopes of curves for those with $\bar{D}$s smaller than $\bar{D}_{Zr}$ (e.g. P_2O_5) are elevated with respect to CFC. The trends for even highly compatible elements (e.g. Ni) are much flatter than for CFC. (The CTL model of course generates curves on log - log plots, and the term "slope" is used rather loosely in this discussion.)

In Figure 27 CTL curves and the corresponding CFC liquid and cumulate paths for $\bar{D}$s corresponding to a eutectic clinopyroxene + olivine + plagioclase assemblage are superimposed over the Chunky Gal Mountain data. The placement of the curves is constrained by the requirement of reproducing the data trends for the same range of k values for all elements, which fixes the range of Zr values. The curves are drawn so that the CTL curve joins the CFC lines at $F = 0.6$ or 40% fractionation. The choice of $F = 0.6$ is arbitrary; the value of F used does not affect the lengths or slopes of any of the curves, nor does it affect the liquid composition implied by the CTL fits. Examination of the figures demonstrates that the CTL curves are consistent with trace- and minor-element trends for the amphibolites over a

Figure 27. Chunky Gal Mountain Complex data for selected elements plotted against Zr with CTL model curves and corresponding CFC model cumulate and liquid lines superimposed. Placement of the model curves is chosen to qualitatively best correspond to the data, with the constraint that curves for all elements must correspond to the same range of Zr values. Lithologic symbols as in previous figures, and $\bar{D}_i$s as indicated. (a) Y. (b) P_2O_5. (c) TiO_2. (d) Nb. (e) Cr. (f) Ni. (g) FeO/MgO. (h) TiO_2 data, also showing model curves for olivine CFC (filled squares) and sorting (filled circles) superimposed.

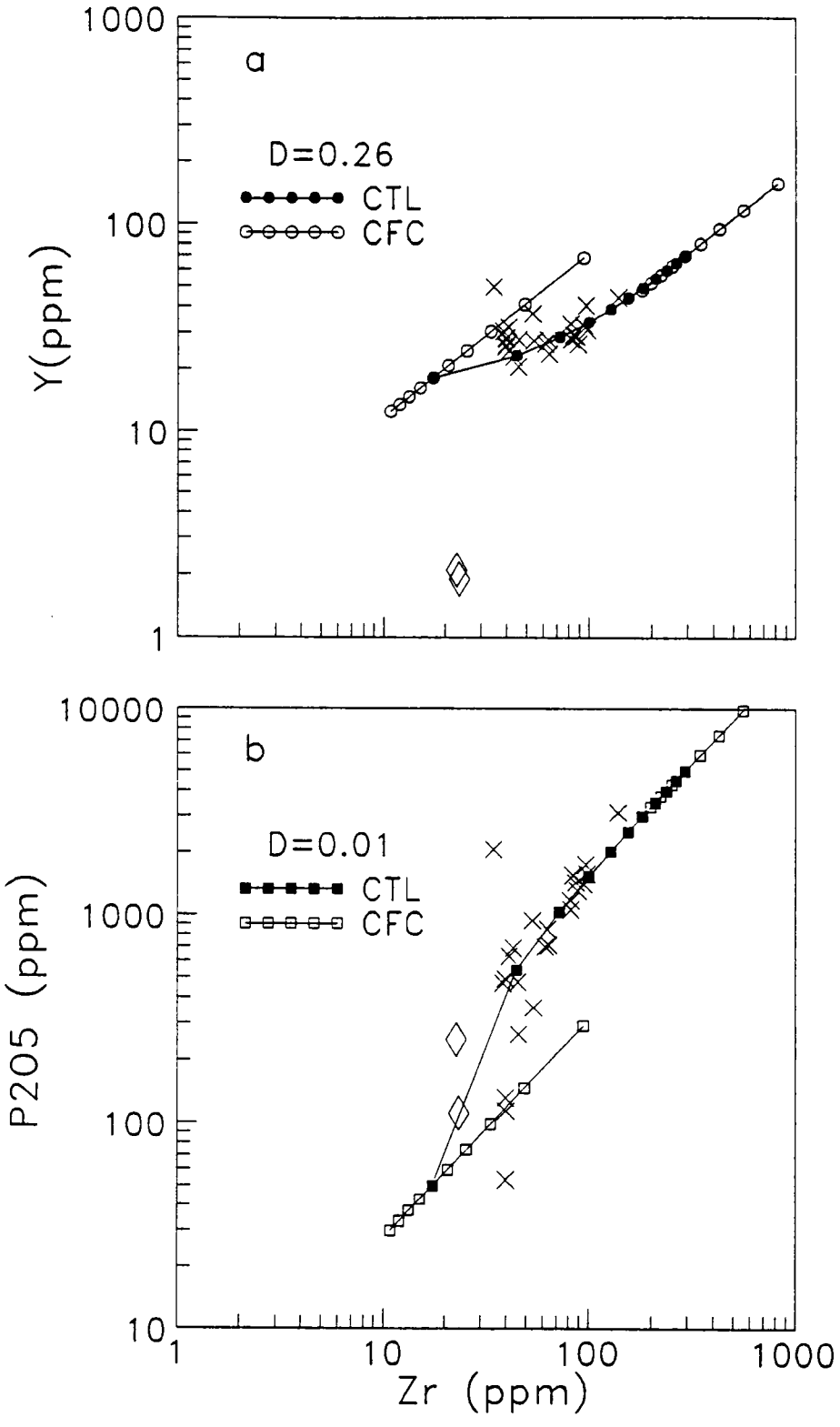
a
D=0.26
CTL
CFC
Y(ppm)
1000
100
10
1
b
D=0.01
CTL
CFC
P205 (ppm)
10000
1000
100
10
1
10
100
1000
Zr (ppm)

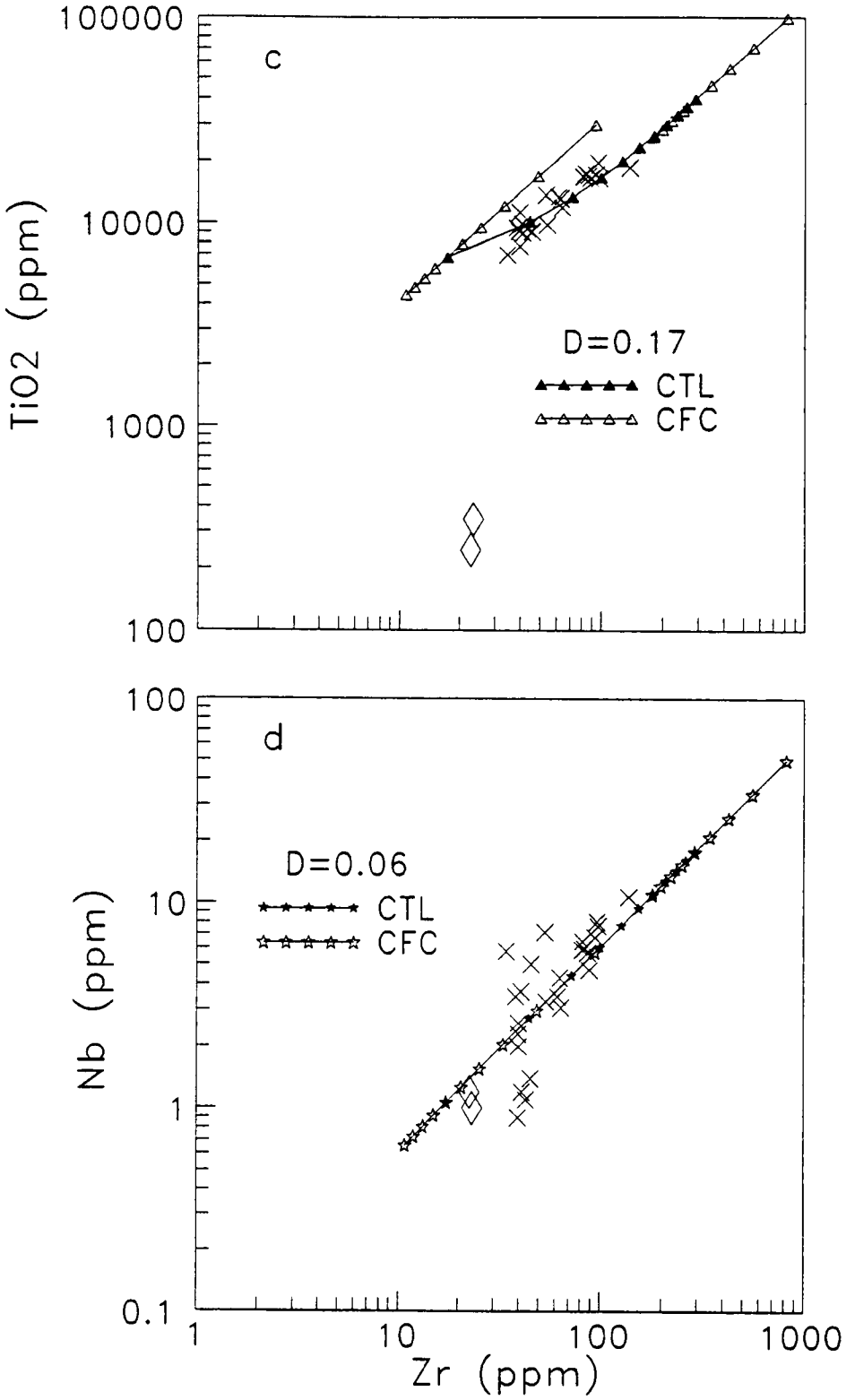
c
TiO2 (ppm)
100000
10000
1000
100
D=0.17
CTL
CFC
d
Nb (ppm)
100
10
1
0.1
D=0.06
CTL
CFC
1
10
100
1000
Zr (ppm)

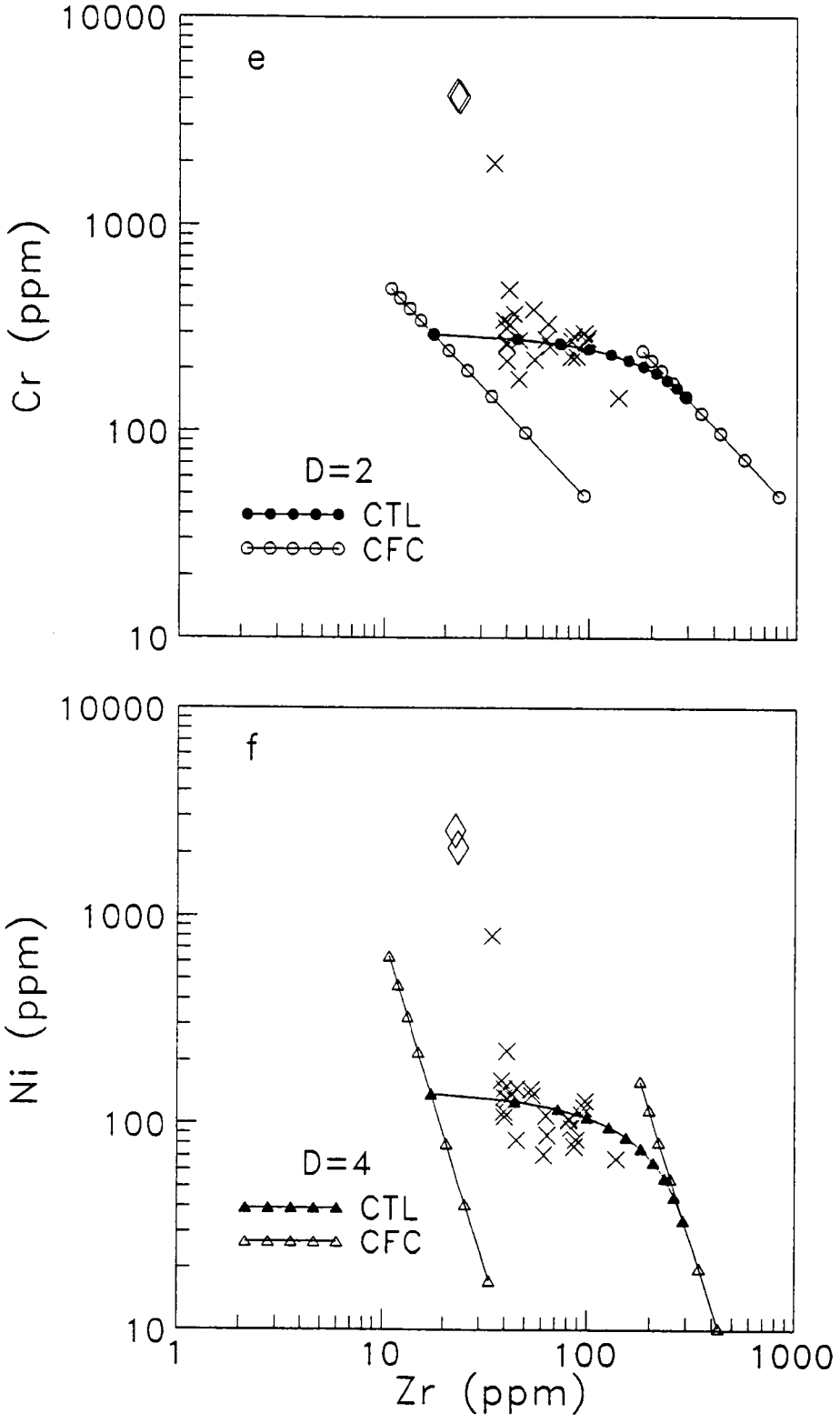
e
10000
1000
100
10
Cr (ppm)
D=2
CTL
CFC
f
10000
1000
100
10
Ni (ppm)
D=4
CTL
CFC
1
10
100
1000
Zr (ppm)

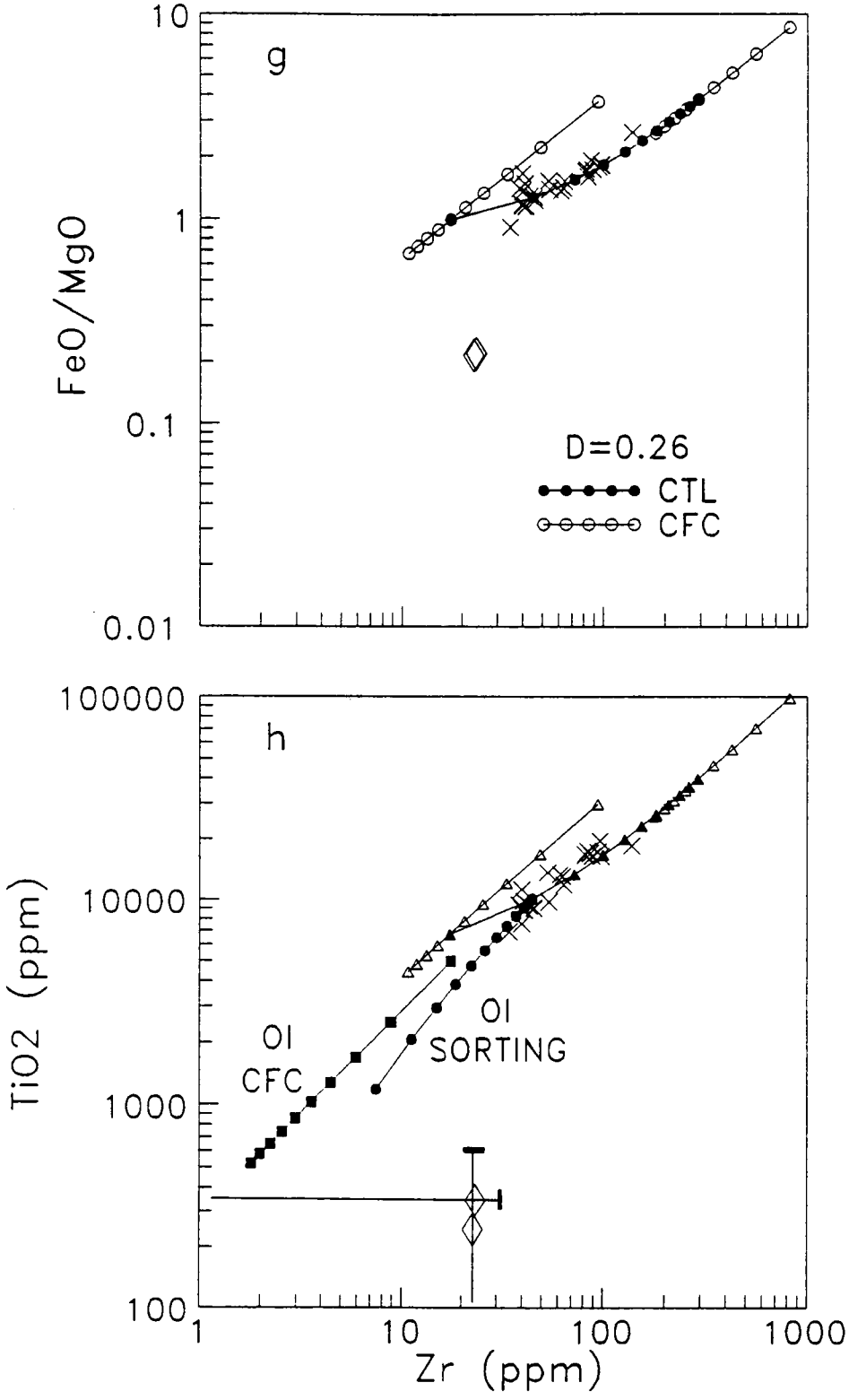
g
10
1
0.1
0.01
FeO/MgO
D=0.26
CTL
CFC
h
100000
10000
1000
100
TiO2 (ppm)
OI
CFC
OI
SORTING
1
10
100
1000
Zr (ppm)

reasonable and consistent range of k values, between 0.0 to 0.5 in all cases. The CTL curves reproduce not only the slopes of the curves for Y and P_2O_5 (Figures 27a and b) but also the sense of curvature seen in the data. The CTL curve for TiO_2 (Figure 27c) is slightly less steep than the corresponding CFC line and is consistent with the regression line for the data, which has a slope somewhat less than that expected for CFC. The CTL curve for Nb (Figure 27d) is a line at 45^0 and fits the data well except for some scatter above and below the line for Type I amphibolites at low Zr concentrations. This scatter can plausibly be attributed to crystal sorting of clinopyroxene or of oxide phases to which Nb would be sensitive. Analytical error may also be responsible for some of the scatter since values of Nb at the lower end of the trend are less than the standard error of calibration (2 ppm). Standard errors of calibration for TiO_2, Cr and Ni are 300 ppm, 50 ppm and 21 ppm, respectively, giving error bars about the size of the data symbols or less.

The fits to the compatible elements Cr and Ni (Figures 27e and f) are somewhat equivocal, both because of the large uncertainties in the appropriate partition coefficients for these elements, and because in the relevant k range CTL curves for compatible elements look essentially the same for a broad range of $\bar{D}$s. CTL curves do, however, produce the depression of the slope with respect to CFC lines that is seen in the data, and fits can be made for quite reasonable ranges of $\bar{D}$.

The fit for Cr appears to be somewhat better if a $\bar{D}_{Cr}$ larger than that obtainable from crystallization of only primary minerals using the average distribution coefficient is used; larger olivine or clinopyroxene partition coefficients or a very small amount of an oxide phase on the liquidus could easily account for the Cr trend, and either is certainly plausible.

Figure 27g shows CFC and CTL curves superimposed over the data for FeO/MgO ($\bar{D}_{FeO/MgO}$ = 0.26). The CTL fit to FeO/MgO is quite good. This good fit implies that if FeO/MgO were used as a differentiation index rather than Zr, CTL curves would still fit the data for all the modeled elements well. This fact provides an independent check on the model fits.

For the CFC model discussed in the previous section, the model lines could not be made to reproduce the data trends by any reasonable choice of proportions of primary or secondary cumulus phases. In contrast for the CTL model, the curves are consistent with the data for a wide range of modes of cumulus phases and corresponding $\bar{D}$s. For the incompatible elements, the slopes and lengths of the CTL model curves depend on the ratio of clinopyroxene to olivine + plagioclase in the cumulus assemblage (Table 3). If a ratio smaller than the eutectic proportions used in constructing the curves shown in Figure 27 were assumed (i.e. smaller $\bar{D}$s), the curves would be somewhat steeper for TiO_2 and Y, somewhat shallower for P_2O_5 and longer for all than those shown but would still reproduce the data

trends, although for small amounts of clinopyroxene (~ 20%) the fits become poor. For higher ratios of clinopyroxene to plagioclase + olivine than illustrated in Figure 27 (i.e. larger $\bar{D}s$), the behavior of the curves is the opposite of just described. The correspondence of the curves to the data is quite good even for very high modal clinopyroxene. As discussed earlier, CTL curves for compatible elements are quite insensitive to the choice of $\bar{D}s$ in the relevant range of $k < 0.5$.

One amphibolite plots noticeably off-trend on most plots, and has particularly high Cr and Ni; its composition is most likely influenced by the sorting of olivine (this sample also has very high MgO), perhaps accompanied by a spinel phase such as chromite. In addition to the vertical scatter on the Nb diagram discussed above, there also tends to be some vertical scatter at the lower ends of the trends on most other diagrams. That seen in the Y, P_2O_5 and FeO/MgO plots is suggestive of some of the amphibolites being the products of larger degrees of fractionation; for example a CTL curve drawn for an F 0.3 larger than originally assumed would encompass almost all the scatter for these elements. The distributions for other elements, however, are not entirely consistent with this picture, and minor crystal sorting probably also contributes to the scatter.

The two dunites which are included among the Chunky Gal Mountain samples plot well above the amphibolite trends for

the compatible elements and well below or off the amphibolite trends for the incompatible elements. These distributions are qualitatively consistent with three possible relationships between these dunites and the Chunky Gal Mountain amphibolites: 1) the dunites are an earlier product of the fractional crystallization of the same parent liquid; 2) they are the products of crystal sorting of olivine from the same liquid; or 3) they are not genetically related to the amphibolites but were intruded into them or juxtaposed against them in some other way. Unfortunately, it is not possible to rule out unequivocally any of these possibilities because of two reasons. First, because of the very low values of trace-element concentrations in the dunites, analytical uncertainties in the data for many of the elements are of the same order as the concentrations. Second, because of the very small distribution coefficients involved in modeling olivine fractionation or mixing, the shapes and locations of model curves and interpretations based on them are very dependent on the exact values of distribution coefficients chosen in this case. Both of these effects are magnified at low concentrations on log - log plots.

Figure 27h illustrates both a CFC cumulate curve for the crystallization of olivine alone and an olivine sorting curve (Equation 7) on a TiO_2 diagram. These curves were constructed using model values for olivine partition coefficients for TiO_2 and Zr. The data for the dunites are qualitatively consistent

with either model, but neither model fits the data well. As the error bars show, analytical uncertainties in the dunite data do not allow one to reject either of the alternatives. In addition only slightly different choices of the D^{Ol}s can produce model curves that fit the data much better. Although the large percentage uncertainties in element concentrations and the strong $\bar{D}$ dependence do not allow one to either chose or rule out CFC or sorting models, it is clearly not necessary to postulate origins from different liquids for the dunites and the amphibolites of Chunky Gal Mountain.

Metamorphic Processes

Mixing models, similar to CTL and crystal sorting models, can be used to rule out the possibility that the Chunky Gal Mountain trends were produced by metamorphic differentiation or compositional changes due to mixing of metamorphic fluids or diffusion from the metasedimentary rocks. Because plagioclase and olivine have similar affinities for TiO_2, a metamorphic differentiation model curve for plagioclase/mafic-mineral sorting would look much like the olivine sorting curve already examined in Figure 27h. Comparison of the length of the sorting curve with the length of the amphibolite data trend implies that, if metamorphic differentiation were responsible for the trend, the Chunky Gal Mountain amphibolites should exhibit a very wide range of modal plagioclase, i.e. from about 10% to 80%, which is inconsistent

with observed amphibolite assemblages. Furthermore, metamorphic differentiation cannot account for the trends in the compatible element data; mafic minerals have much larger affinities for Ni and Cr than does plagioclase, and crystal sorting or mixing curves for plagioclase/mafic-mineral separation would be quite steep rather than flat as observed. That compositional changes due to mixing of metamorphic fluids or diffusion from the metasediments are highly unlikely explanations for the Chunky Gal Mountain data can be seen from the CTL model fits already examined. These curves could represent a metamorphic mixing or diffusion process; however, fits to the data imply an unrealistic amount of mixing (more than 40%) for metamorphic processes. In addition, this amount of mixing of disparate materials should produce major-element trends, which are not seen in the data.

Liquid Composition

The relationship of the CTL model curves to the Chunky Gal Mountain data implies an approximate trace-element composition for the liquid with which the cumulus assemblage was in equilibrium (Table 5). This composition is represented by the points at which the CTL curves join the CFC liquid curves. The trace-element values implied by the curves are, of course, very approximate and could be changed substantially by shifting the curves slightly or by minor changes in the $\bar{D}$s used to construct the curves. All implied liquid

Table 5. Estimated Liquid Compositions

Element	Composition (ppm)	
	Chunky Gal Mountain	Carroll Knob
Zr	291	110 - 160
Y	70	12 - 35
P_2O_5	5000	1200 - 8000
TiO_2	40000	1800 - 8000
Nb	18	1 - 3
Cr	147	<10 - 28
Ni	35	<10 - 20
FeO/MgO	3.8	1 - 1.8
Zr/TiO_2	0.01	0.02 - 0.07*
Zr/Y	4.2	4.3 - 8.7*
Y/Nb	3.9	12 - 13*
Zr/Nb	16.0	100 - 46*

*Range normalized to Zr = 130 ppm.

concentration values are, however, roughly consistent with a basaltic liquid, probably relatively evolved as indicated by high concentrations of incompatible elements, low concentrations of compatible elements and the high FeO/MgO ratio.

Pearce and Norry (1979) present data, which have been screened both for analytical quality and to exclude samples with cumulus components, for a large number of basalt samples from island arc, ocean floor and within plate settings plotted on two-element variation diagrams. Figures 28a and 28b show the Chunky Gal Mountain data and the model liquid composition plotted on three of their diagrams. These plots are often used as tectonic discriminant diagrams. The validity of discriminant diagrams, however, rests on statistical arguments requiring data from many samples, and the figures cannot be used to infer the provenance of the Chunky Gal Mountain rocks from the model liquid composition with certainty. However, these figures do illustrate: 1) that the approximate Chunky Gal Mountain liquid composition is reasonable, and 2) that deducing provenance directly from trace-element compositions in cumulate rocks will most likely give spurious results; the Chunky Gal Mountain rocks are much more likely to be related to an ocean floor or continental setting, as implied by the model liquid composition shown in the figures, than an island arc setting, as might be concluded directly from the amphibolite data. The model-derived Zr/Nb liquid ratios

Figure 28. Model-derived liquid composition (large lined symbol) and Chunky Gal Mountain Complex amphibolite data plotted on diagrams showing basalt fields. (a) Zr/Y vs Zr and (b) TiO_2 vs Zr, from Pearce and Norry (1979). ARC = island arc basalt, OFB = ocean floor basalt, and WPB = within plate basalt. (c) Zr/Y - Zr/Nb - Y/Nb and (d) TiO_2 vs FeO/MgO (FeO = total iron calculated as FeO), from Fodor and Vetter (1984). N = normal mid-ocean ridge basalt, T = transitional mid-ocean ridge basalt, and CFB = continental flood basalt.

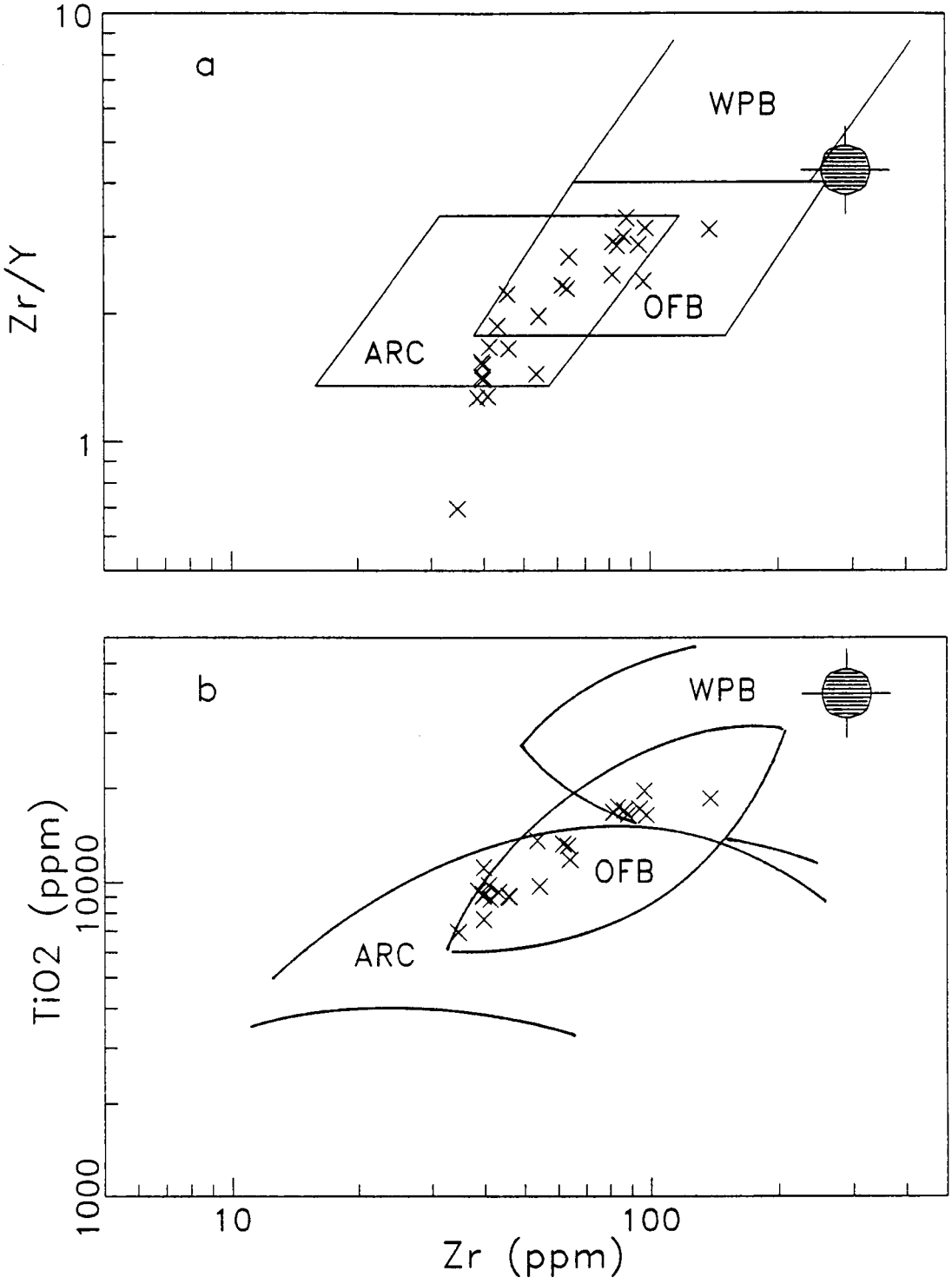
a
WPB
OFB
ARC
Zr/Y
10
1
b
WPB
OFB
ARC
TiO2 (ppm)
10000
1000
10
100
Zr (ppm)

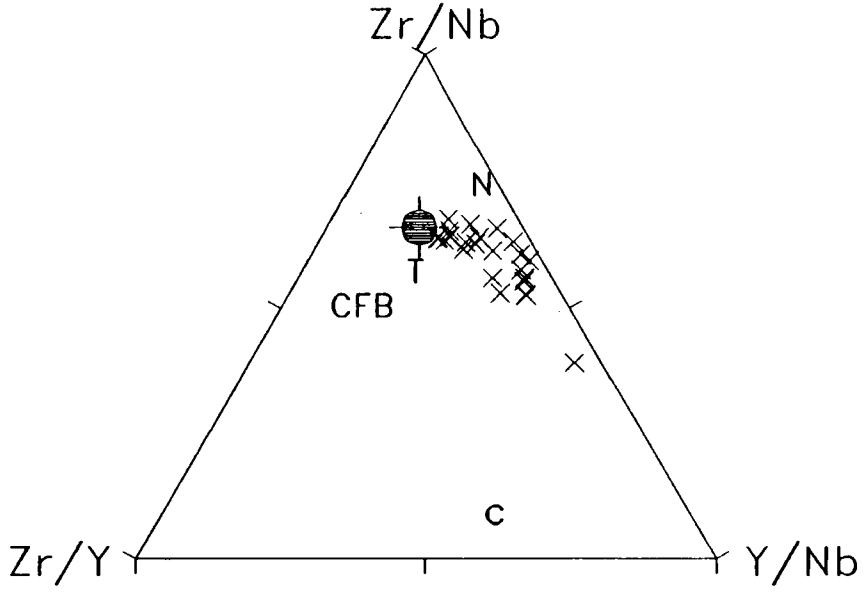
Zr/Nb
N
T
CFB
c
Zr/Y
Y/Nb

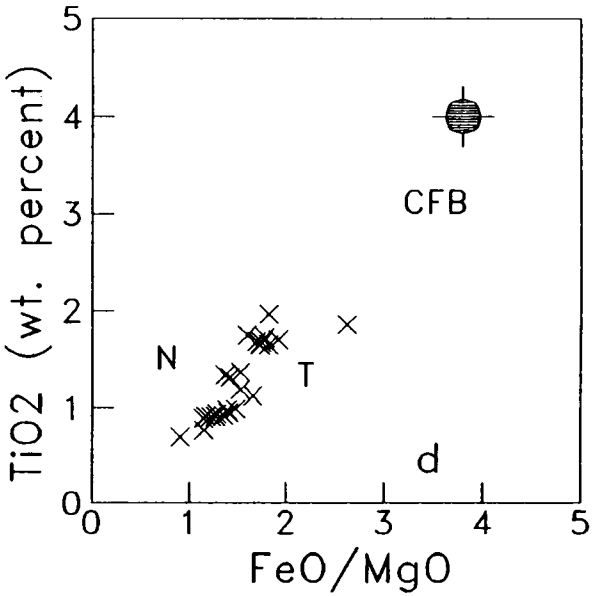
TiO2 (wt. percent)
5
4
3
2
1
0
CFB
N
T
d
0
1
2
3
4
5
FeO/MgO

(Table 5) is consistent with either ocean floor or within-plate settings but is somewhat too low for an island arc setting (Pearce and Norry, 1979).

The Y/Nb value clearly implies a tholeiitic rather than a alkaline or calc-alkaline character (Pearce and Cann, 1973), which is consistent with the major-element data.

Although the Chunky Gal Mountain liquid composition plots in or near the within plate field in the above diagrams, the many uncertainties in the analysis preclude choosing between the two settings based on the diagrams alone. Figures 28c and 28d are discriminant diagrams from Fodor and Vetter (1984), which distinguish continental flood basalts from ocean floor basalts in terms of Zr/y, Y/Nb and Zr/Nb and typical TiO_2 and FeO/MgO concentrations, respectively. Magma provenance is also equivocal on these diagrams. In Figure 28c the liquid composition plots in the transitional mid-ocean ridge field, but the high values of both TiO_2 and FeO/MgO (Figure 28d) are suggestive of continental flood basalts. Again, because of the uncertainties in the analysis, it is difficult to draw a firm conclusion from the above diagrams; however, the inability to clearly assign the Chunky Gal Mountain model-derived liquid composition to either a continental or ocean floor setting suggests that the liquid could have originated in a transitional continental rift - to - ocean floor setting.

Isolated Amphibolites and Kimsey Bald Amphibolites

The overall congruence of the isolated amphibolite and the Chunky Gal Mountain data trends implies that the Chunky Gal Mountain-derived CTL curves will reproduce element abundances and the natures of the isolated amphibolite trends. The curves mimic the relatively flat Y, TiO_2, Ni, Cr and FeO/MgO trends, the elevated P_2O_5 trend and the Nb trend at approximately 45^0 seen in the isolated amphibolite data. For example, Figures 29a and 29b show the isolated amphibolite data for Y and Ni, respectively, overlain by the appropriate Chunky Gal Mountain CTL curves. The considerable scatter in the isolated amphibolite data can be attributed to several sources, including element mobility, crystal sorting and variations in the degree of fractionation, although it is difficult to document the effects of any one of these processes alone. Even given the scatter in the isolated amphibolite data and the probability of several extraneous processes having affected these rocks, the overall congruence of data with the Chunky Gal Mountain trends implies that most of the isolated amphibolites are genetically related to the Chunky Gal Mountain amphibolites, and that their compositional trends are dominated by the mixing of cumulus minerals with intercumulus liquid. The protoliths of these rocks were thus primarily plutonic rather than volcanic, as previously assumed.

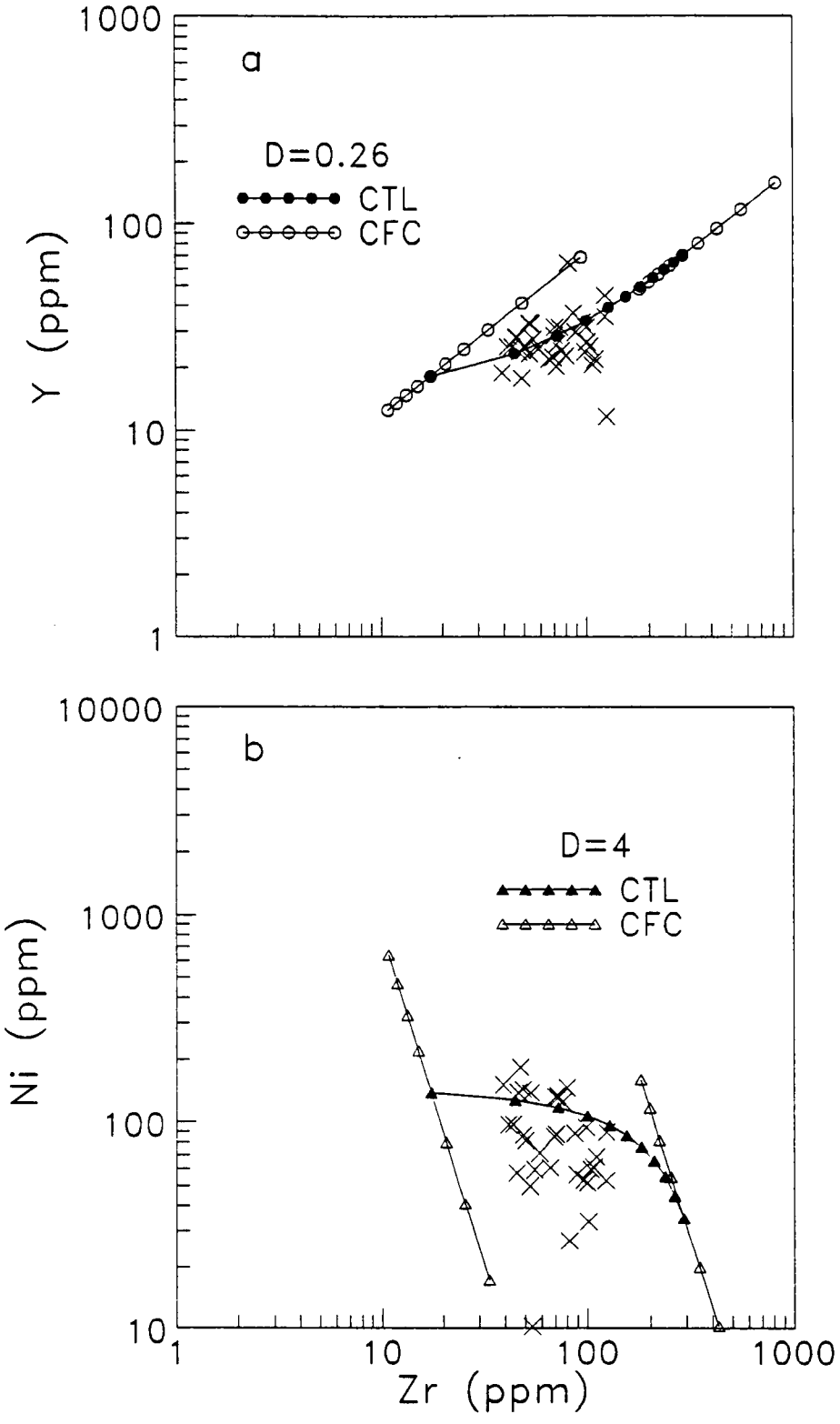

Figure 29. Selected isolated amphibolite data plotted against Zr with Chunky Gal Mountain CTL model curves and corresponding CFC model cumulate and liquid lines superimposed. Lithologic symbols as in previous figures, and $\bar{D}_i$s as indicated. (a) Y. (b) Ni.

The implications from the model curves for the relationship of the Kimsey Bald amphibolites to the Chunky Gal Mountain amphibolites and the isolated amphibolites are somewhat less certain but still compelling. Data are available for only four of the elements modeled, Zr, Y, P_2O_5, and TiO_2, and the FeO/MgO ratio. These data all cluster at the lower ends of the Chunky Gal Mountain trends (Chapter III). The data for P_2O_5 concentrations appear to be anomalously high. There are two plausible reasons for these high values: 1) they result from the sorting of apatite, or 2) they result from differences between analytical equipment or methods. It is not possible to discriminate between these alternatives from the available data. However, the data for Y, TiO_2 and Zr (together with major-element data and the physical proximity of the body) strongly suggest that the Kimsey Bald amphibolites are genetically related to the Chunky Gal Mountain amphibolites, and that their protoliths were cumulate rocks with small amounts of trapped intercumulus liquid.

Models for the Lake Chatuge Suite

Figures 30a and 30b show the Lake Chatuge data for Y and Ni overlain by the Chunky Gal Mountain/isolated amphibolite CTL and CFC model curves. For Y, the other incompatible elements and FeO/MgO, many of the Lake Chatuge samples plot on

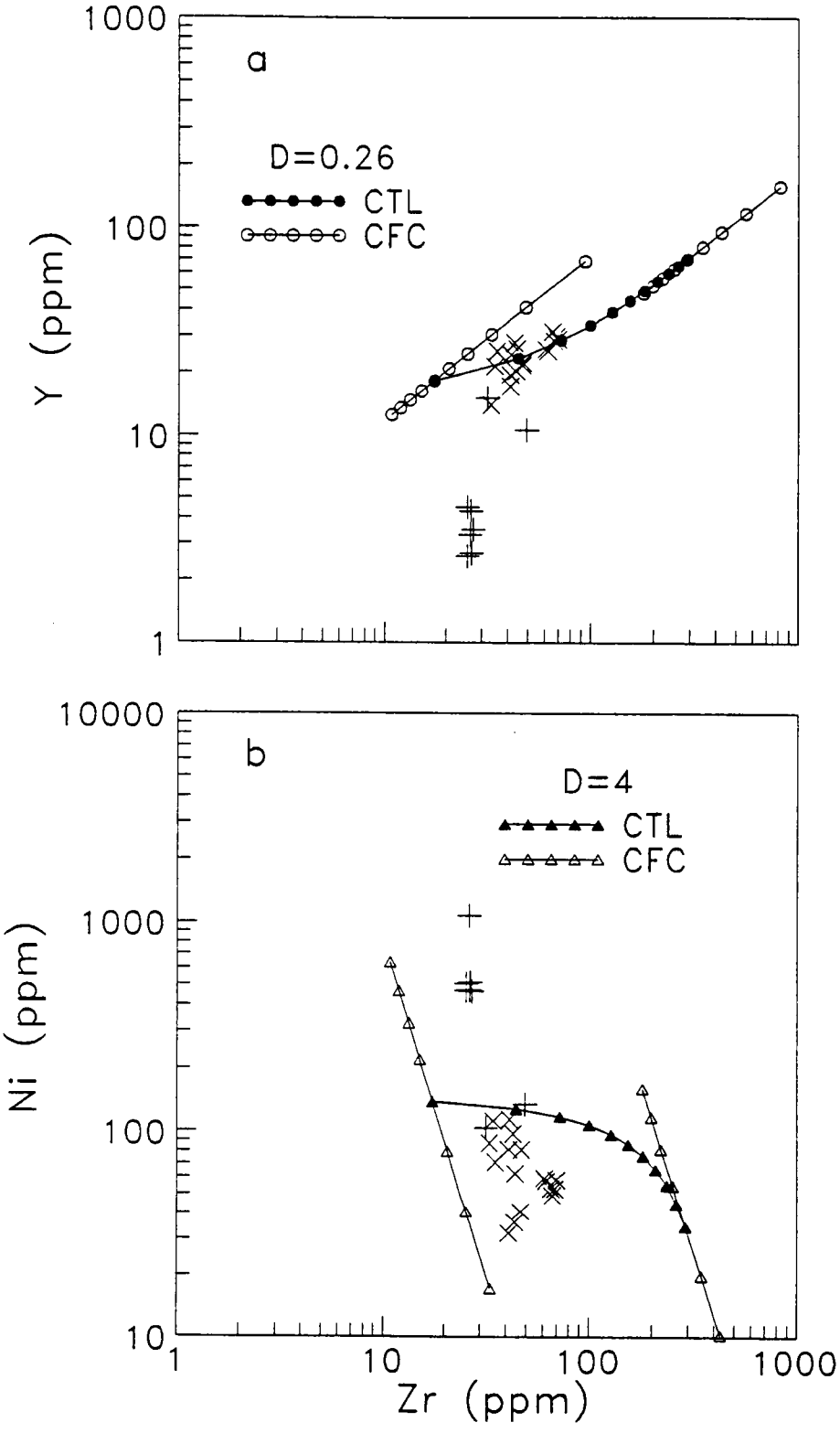

Figure 30. Selected Lake Chatuge Complex data plotted against Zr with Chunky Gal Mountain CTL model curves and corresponding CFC model cumulate and liquid lines superimposed. Lithologic symbols as in previous figures, and $\bar{D}_i$s as indicated. (a) Y. (b) Ni.

or near the Chunky Gal Mountain/isolated amphibolite model curves. In particular, there is a rather tight cluster of points at relatively high Zr which consistently plots on the CTL curves for these elements at $k < 0.2$. On the compatible element diagrams, illustrated by Ni, these same samples plot well below the CTL model curves. However, the Chunky Gal Mountain data for Cr and Ni for which the curves were drawn show considerable scatter also, and the vertical placement of the model curves can only be regarded as approximate. In addition, crystal sorting or small amounts of assimilation or element mobility may contribute the apparent Ni and Cr depletion in these rocks relative to the Chunky Gal Mountain rocks (cf. the isolated amphibolite data for Ni, which show even greater scatter). The data for many of the Lake Chatuge amphibolites are thus consistent, quantitatively for the incompatible elements and qualitatively for the compatible elements, with their having been cumulates, with relatively small amounts of trapped liquid, from a Chunky Gal Mountain-type magma. These amphibolites were collected from several locations across the complex and thus appear to be a integral component of the Lake Chatuge Complex.

Most amphibolite samples with lower Zr concentrations tend to show some amount of vertical scatter for all elements, and the amphibolites and olivine gabbros are clearly distinguishable on all plots, except perhaps the plot for P_2O_5. The distributions of the low-Zr amphibolites and the olivine

gabbros are explainable by crystal sorting involving a Chunky Gal Mountain-type cumulate and one or more major or minor phases typically on the liquidus of a mafic liquid. The case for the olivine gabbros is clearer. The distribution of the olivine gabbros with respect to the other Lake Chatuge rocks is consistent with their high modal olivine (~30%); most obviously, they are enriched in Ni and depleted in TiO_2 and Y. It is highly unlikely that these samples represent equilibrium cumulates because the high modal olivine is not consistent with eutectic compositions at any pressure; Presnall et al. (1978) showed that increases in pressure in the equivalent synthetic system Fo - An - Di shift the eutectic point toward the An apex but do not substantially change the equilibrium modal proportion of Fo from less than 10%. The olivine gabbros are thus almost certainly the products of crystal sorting of olivine and perhaps also plagioclase. Comparison of Figures 30a and 30b with the corresponding Chunky Gal Mountain figures, 27a and 27f, respectively, shows that the olivine gabbros plot above the Chunky Gal Mountain dunites on the Y diagram and below them on the Ni diagram, positions that are qualitatively consistent with the relative proportions of olivine in the two lithologies. As in the case of the Chunky Gal Mountain dunites, the model sorting curves for olivine do not reproduce the distribution of the olivine gabbros well but are qualitatively consistent with the sorting hypothesis.

The vertical scatter seen in the amphibolites at relatively low Zr is also most likely a result of sorting, probably of more than one mineral. The low-Zr amphibolite distributions are suggestive of their being complementary to the olivine gabbros, i.e. they appear to be depleted in olivine (i.e. lower Ni) with respect to eutectic proportions. However, the overall picture appears to be somewhat more complicated. For example, the Nb distribution is not consistent with the sorting of only olivine, and it is probable that the distributions of these amphibolites are influenced by the sorting of other minerals (e.g. pyroxenes or oxide phases) and perhaps fractionation effects as well. Thus, although it may not be possible to distinguish all effects, it is clearly possible to relate all the Lake Chatuge amphibolites and olivine gabbros to each other and to the Chunky Gal Mountain/isolated amphibolite trends by plausible cumulate processes.

The pyroxene gabbros plot reasonably near the low-Zr amphibolite data on all diagrams. Neither phase relations nor relict lithologies (Table 1) observed at Lake Chatuge preclude these rocks being related to the olivine gabbros by fractional crystallization if the following crystallization sequence is assumed Ol; Ol + Pl; Ol + Pl + Cpx; Pl + Cpx + Opx. This sequence implies that the pyroxene gabbros were late-stage differentiates. However, their plotting positions are not consistent with this process alone, and one would have to

invoke crystal sorting and perhaps varying amounts of trapped liquid to explain the distributions; either of these processes is, of course, quite plausible. In addition changes in load pressure, P_{H2O}, or composition due to assimilation can result in changes in crystallizing assemblages from the same parent liquid. Thus there is nothing to preclude the pyroxene gabbros from being related to a Chunky Gal Mountain-type liquid, and all the Lake Chatuge rocks sampled for this study, as well as the garnet-pyroxene gneiss that have compositions similar to the amphibolites (Dallmeyer, 1974), are relatable to the Chunky Gal Mountain/isolated amphibolite liquid trend by reasonable cumulate processes.

Models for the Carroll Knob Complex

Relationships to the Chunky Gal Mountain/Isolated Amphibolite Trends

Figures 31a through 31d show the Chunky Gal Mountain-derived CTL curves and the corresponding CFC lines superimposed over the Carroll Knob data for selected modeled elements and FeO/MgO. The data for most of the Carroll Knob samples plot in vertical patterns to the left of and above and below the Chunky Gal Mountain/isolated amphibolite CTL curves and clearly are not consistent with most of the Carroll Knob rocks being related to these amphibolites by the CTL process. However, the data for seven amphibolites, although somewhat

Figure 31. Selected Carroll Knob Complex data plotted against Zr with Chunky Gal Mountain CTL model curves and corresponding CFC model cumulate and liquid lines superimposed (symbols as in previous figures). Open stars denote CFC cumulate lines for a two-pyroxene gabbro cumulus assemblage, and filled stars are the corresponding CTL model curves. Lined parallelograms enclose estimated Carroll Knob liquid compositions. Representative partial error bars are also shown. Lithologic symbols as in previous figures. (a) Y. (b) TiO_2. (c) Cr. (d) FeO/MgO.

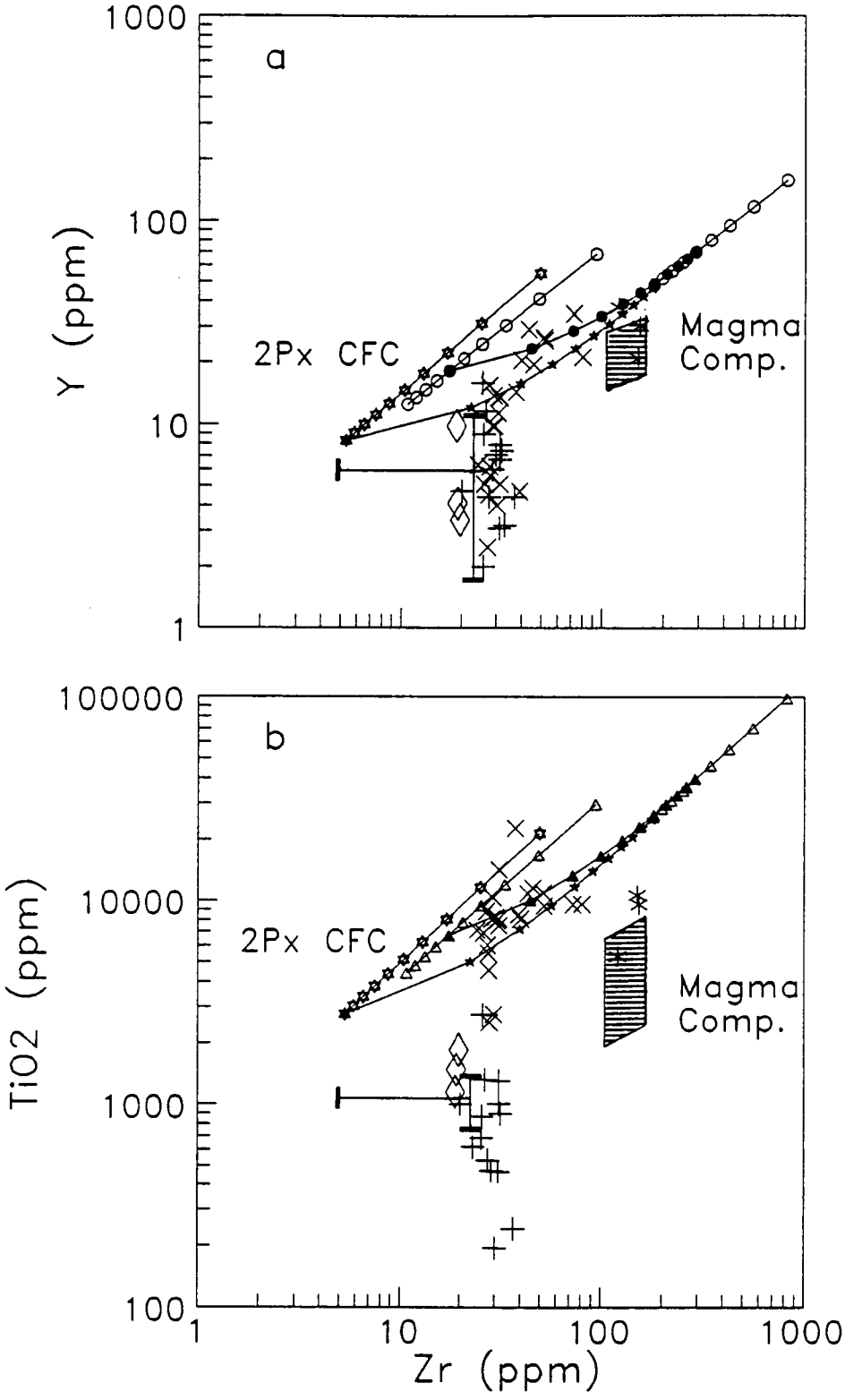
a
1000
100
10
1
Y (ppm)
2Px CFC
Magma
Comp.
b
100000
10000
1000
100
TiO2 (ppm)
2Px CFC
Magma
Comp.
1
10
100
1000
Zr (ppm)

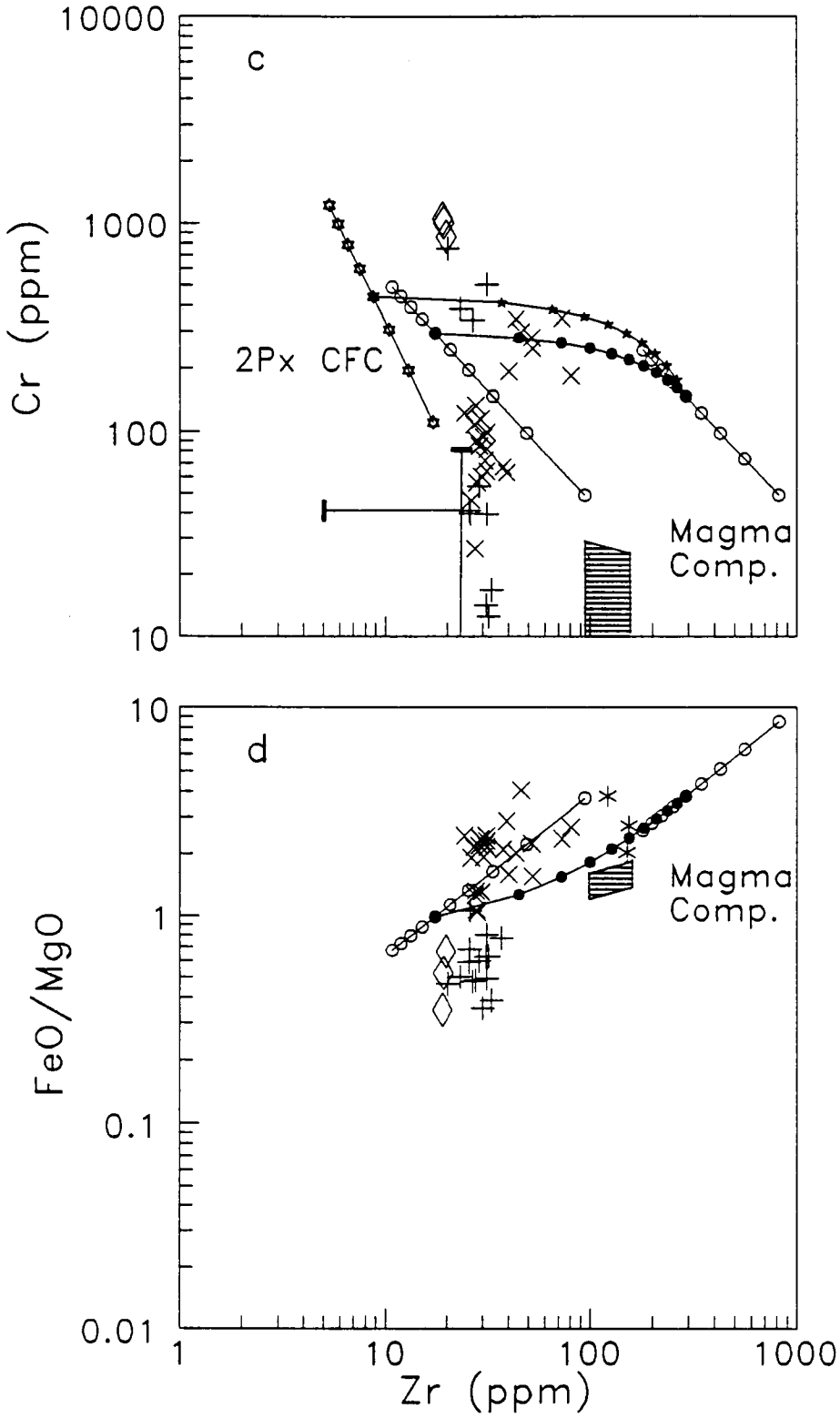
c
10000
1000
100
10
Cr (ppm)
2Px CFC
Magma
Comp.
d
10
1
0.1
0.01
FeO/MgO
Magma
Comp.
1
10
100
1000
Zr (ppm)

scattered, consistently plot around the Chunky Gal Mountain model curves at relatively high Zr values. All these amphibolites were collected from the periphery of the complex, and thus their spatial distribution, as well as their chemistry, suggest that they probably should be assigned to the isolated amphibolite suite rather than the Carroll Knob suite. It is also probable that some element mobility has occurred in these rocks both because of the observed scatter and because they include the biotite amphibolites described in the Carroll Knob petrology section in Chapter II, which show signs of late-stage major-element mobility. The epidosites plot in a field separate from the other Carroll Knob rocks and will be discussed later in this section.

The distributions of the data for the rest of the Carroll Knob samples with respect to the Chunky Gal Mountain CFC curves show that they cannot be equilibrium cumulates, with or without trapped liquid, from the magma that produced the Chunky Gal Mountain rocks. This conclusion is demonstrated on the TiO_2, Y and Cr plots on which, in addition to the Chunky Gal Mountain/isolated amphibolite CFC liquid and cumulate lines, a CFC cumulate line and a CTL curve are drawn for a two-pyroxene gabbro assemblage, as suggested by relict mineralogy at Carroll Knob. The two-pyroxene gabbro cumulate line is drawn for $k = 0$ and so that the corresponding two-pyroxene gabbro liquid line (not shown) passes through the Chunky Gal Mountain liquid line at $F = 0.6$; for Y and TiO_2 it

is almost identical to the Chunky Gal Mountain liquid line, and for Cr it is steeper. The two-pyroxene gabbro CTL curve is drawn for F = 1 on the Y and TiO_2 diagrams, and joins the point for F = 1 and k = 0 on the two-pyroxene gabbro cumulate line with the point that would be F = 1 and k = 1 on the corresponding liquid line. For reasons which will become apparent, the two-pyroxene gabbro CTL curve for Ni is drawn at F = 0.6.

The possibility that the Carroll Knob rocks might be cumulates from an earlier stage of fractionation of a Chunky Gal Mountain-like liquid is ruled out by the compatible element data. Cumulate rocks from a less evolved Chunky Gal Mountain-like liquid should have Cr and Ni contents well above the values for the majority of Carroll Knob samples, i.e. above the CTL curve for about F = 0.6 in Figure 31c. The metagabbros that plot near this area have modal pyroxene well above eutectic proportions (Cr and Ni are partitioned into pyroxenes, Table 3), cf. the pyroxenites. In addition, the Y and TiO_2 data clearly show that the Carroll Knob rocks cannot have crystallized from a more evolved Chunky Gal Mountain-type liquid. Cumulate rocks crystallizing from such a liquid at any value of F should have Y and TiO_2 concentrations much higher than observed in most of the Carroll Knob data, i.e. the data for these element should plot above the F = 1 CTL curves. (On the TiO_2 diagram most of the Carroll Knob amphibolites plot near the Chunky Gal Mountain cumulate

curves, but this is the only diagram on which they do so.) The near correspondence of the two-pyroxene gabbro and the olivine gabbro CFC cumulate lines, especially on the Y and TiO_2 diagrams, demonstrates that the above conclusions do not depend on the exact values of the $\bar{D}$s chosen, and the error bars drawn on the figures show that discrepancies between the cumulate curves and the data are much greater than analytical uncertainty. Thus the Carroll Knob rocks cannot be equilibrium cumulates, with or without trapped liquid, derived from a Chunky Gal Mountain-type liquid.

The locations of the vertical Carroll Knob data patterns at the cumulate ends of the Chunky Gal Mountain/isolated amphibolite CTL curves suggest that the these suites could be related by crystal sorting. Field relations, i.e. spatial separation, and probable differences in crystallizing assemblages, as implied by different relict cumulate lithologies, between Chunky Gal Mountain and Carroll Knob make sorting a rather unlikely relationship between the two suites. In addition, for sorting to be an explanation of the data distributions, pyroxene or an oxide phase would have to be depleted in the Carroll Knob rocks with respect to the Chunky Gal Mountain rocks to produce, for example, the lower Y and TiO_2 concentrations in the Carroll Knob data (Y and TiO_2 are both partitioned into pyroxenes and oxides, Table 3). Pyroxene depletion clearly cannot be an explanation for the data because Carroll Knob samples consisting of essentially

all pyroxene, i.e. the pyroxenites, and metagabbros very rich in pyroxene plot below the Chunky Gal Mountain data on the Y and TiO_2 diagrams. Neither is oxide depletion a plausible explanation. To produce, for example, the wide range of TiO_2 values spanned by the Chunky Gal Mountain cumulates and the Carroll Knob metagabbros one would have to invoke sorting of a few percent of a very TiO_2-rich phase, i.e. ilmenite. Such a mechanism should also produce elevated FeO/MgO ratios in the Chunky Gal Mountain cumulates with respect to all the Carroll Knob rocks, which clearly is not the case (Figure 31d). The Carroll Knob amphibolites, metagabbros and pyroxenites, therefore, cannot be related to the implied Chunky Gal Mountain/isolated amphibolite liquid trend by any plausible cumulate process, and most of the Carroll Knob rocks must have crystallized from a parent liquid of essentially different trace- and minor-element composition than that of the Chunky Gal Mountain/isolated amphibolite parent liquid.

Liquid Composition

An approximate range of liquid compositions from which the Carroll Knob rocks could have crystallized can be estimated from the model $\bar{D}$s and the CTL curves for a two-pyroxene gabbro assemblage as follows. First, an idea of the amount of trapped liquid, k, in the metagabbros is obtained from Equation (6) in Chapter IV, which expresses k in terms of $\bar{D}$ and $\hat{D}$. Electron microprobe data (Appendix A) for

clinopyroxenes in one of the best preserved samples (CK73B) indicate an average mineral FeO/MgO of 0.33. Dividing this value by the clinopyroxene/liquid partition coefficient for FeO/MgO, 0.24, (Church and Riccio, 1977; Irvine, 1979) gives a liquid FeO/MgO of about 1.4. Dividing the corresponding bulk rock FeO/MgO (0.5) by the 1.4 gives a $\hat{D}$ of 0.36, and k is then equal to 0.14 from Equation (6). This value of k is quite reasonable but, of course, must be considered very approximate. The range of Zr values observed in the metagabbros (~ 20 ppm) may be an indication of variable amounts of trapped liquid. If this is the case k = 0.14 may be near the lower limit because the sample from which it was calculated has the second lowest Zr of all the metagabbros. On the other hand, this sample has modal orthopyroxene/clinopyroxene in excess of assumed eutectic proportions, which would cause the above estimate of k to be somewhat too large.

The calculated value of k can be used to approximate the region of composition space in which the Carroll Knob liquid originated, using two-pyroxene gabbro CTL model curves. For example, placing the point for k = 0.14 of the $\bar{D}$ = 0.26 CTL curve on sample CK73B (about the middle of the FeO/MgO range) on the FeO/MgO diagram fixes the corresponding liquid composition at the point where k = 1, i.e. Zr = 130 ppm and FeO/MgO = 1.3. Figures 31a through 31d show parallelograms drawn to represent the ranges of probable Carroll Knob liquid

values for the elements shown estimated using the appropriate CTL curve. The range in Zr values encompassed by the parallelograms qualitatively expresses uncertainties in the value of k and is drawn about 20 to 30 ppm above and below Zr = 130 ppm, the value implied by k = 0.14 on the FeO/MgO diagram. The ranges in values for the elements on the ordinates of the plots account for the fact that the vertical trends in the data are almost certainly produced by crystal sorting (see next section), making it unclear which concentrations to choose as equilibrium cumulate values. The liquid concentrations are, of course, very approximate but are adequate to make some useful comparisons with the model Chunky Gal Mountain liquid.

Table 5 summarizes approximate allowable compositions and trace-element ratios for the Carroll Knob liquid. Except for P_2O_5 (which spans a broad range), trace-element abundances in the Carroll Knob liquid are clearly lower than those in the Chunky Gal Mountain model liquid at any stage of fractionation. In addition, trace-element ratios differ from those of the Chunky Gal Mountain model liquid. The ratios shown in Table 5 are normalized to Zr = 130 ppm. Zr/TiO_2, Y/Nb and Zr/Nb are all clearly higher than in the Chunky Gal Mountain model liquid. The low trace-element abundances and the elevated ratios are similar to those seen in island arc-type liquids (Pearce and Norry, 1979; Pearce and Cann, 1973; Hawkins, 1979; Serri, 1981; Miyashiro and Shido, 1979):

Zr/TiO_2 (cf. Figure 28b) and Y/Nb for the Carroll Knob liquid are within expected values for arc basalts, and Zr/Nb is rather high but is closer to arc basalt values than other liquid types. The range of Zr/Y (cf. Figure 28a), however, is higher than seen in most arc basalts and is more suggestive of ocean floor and within plate basalt values. The high Y/Nb value rules out the possibility that the liquid was alkaline, but is consistent with a tholeiitic or calc-alkaline character (Pearce and Cann, 1973). Major-element data are somewhat ambiguous on this point because, as will be shown in the next section, apparent iron-enrichment trends in the data are most likely due to crystal sorting-related processes rather than fractionation. In any case, although there are obviously large uncertainties in the Carroll Knob liquid trace-element abundances and ratios, it is clear: 1) that the Carroll Knob liquid had to have had a fundamentally different trace-element composition than the Chunky Gal Mountain liquid; and 2) that the estimated Carroll Knob liquid element abundances and ratios are most compatible with the chemical characteristics of island arc-type magmas.

Relationships within the Carroll Knob Suite

The relationships among the rocks of the Carroll Knob suite (except for the epidosites) can be explained by cumulate processes, chiefly crystal sorting. For the metagabbros, for which much relict mineralogy remains, comparison of modal data

for individual samples with major-, minor- and trace-element chemistry strongly suggests that the vertical patterns observed in the data result primarily from complementary variations in modal pyroxene and plagioclase. For major elements, for example, the data for those metagabbros with the highest modal plagioclase plot farthest toward anorthite on the ACF diagram shown in Figure 20d, and the pyroxenites and metagabbros with highest modal pyroxene plot toward the pyroxene apexes. For minor and trace elements, the pyroxenites and the metagabbros with highest modal pyroxene are those with the highest abundances of TiO_2 and Cr (both of which are partitioned into pyroxenes), and the rocks with lowest modal pyroxene are those with the lowest values of these elements. The continuous variations in modal pyroxene and plagioclase observed in the metagabbros (~25% to 80%) cannot result from fractionation alone (cf. the lack of curvature in the Cpx-Pl cotectic of the Cpx-Opx-Pl phase diagram, Figure 20c), and crystal sorting is the most likely explanation for the variations in modes and element concentrations. Model sorting curves do not fit the data well for the same reasons discussed in the section on the Chunky Gal Mountain dunites but are qualitatively consistent with the sorting hypothesis.

The metagabbros can also be related to the bulk of the amphibolites of the complex by mineral sorting, in this case of an Fe-Ti oxide phase. Chemically, the amphibolites differ

from the metagabbros by having generally lower CaO and MgO, notably higher FeO/MgO, FeO, TiO_2, MnO, V and Cr; concentration ranges for other elements are about the same. Some of the concentration differences might be explained by postulating that the amphibolites are more fractionated than the metagabbros; however, the relationships between the two groups on AFM and both major- and trace-element variation diagrams do not suggest fractionation trends. Element mobility may be responsible for the variations in CaO and MgO but is unlikely to be the explanation for differences in the other elements. Linear regressions of FeO/MgO versus major, minor and trace elements show good correlations for TiO_2, MnO, and V, but for no other elements (except FeO and MgO, which are automatically correlated). Because these elements and Cr are strongly partitioned into oxide phases, their higher concentrations in the amphibolites with respect to the metagabbros and the correlation patterns suggest that the amphibolites are enriched in one or more Fe-Ti oxide phases with respect to the metagabbros.

Petrography is qualitatively consistent with relative Fe-Ti oxide enrichment in the amphibolites. Rutile and ilmenite occur in both the metagabbros and the amphibolites. These minerals are always well below 1 volume % in the metagabbros but approach 5% in some of the amphibolites. Of the amphibolites in the XRF data set, those with the highest TiO_2 contain 2% to 5% ilmenite and/or rutile. Although it is not

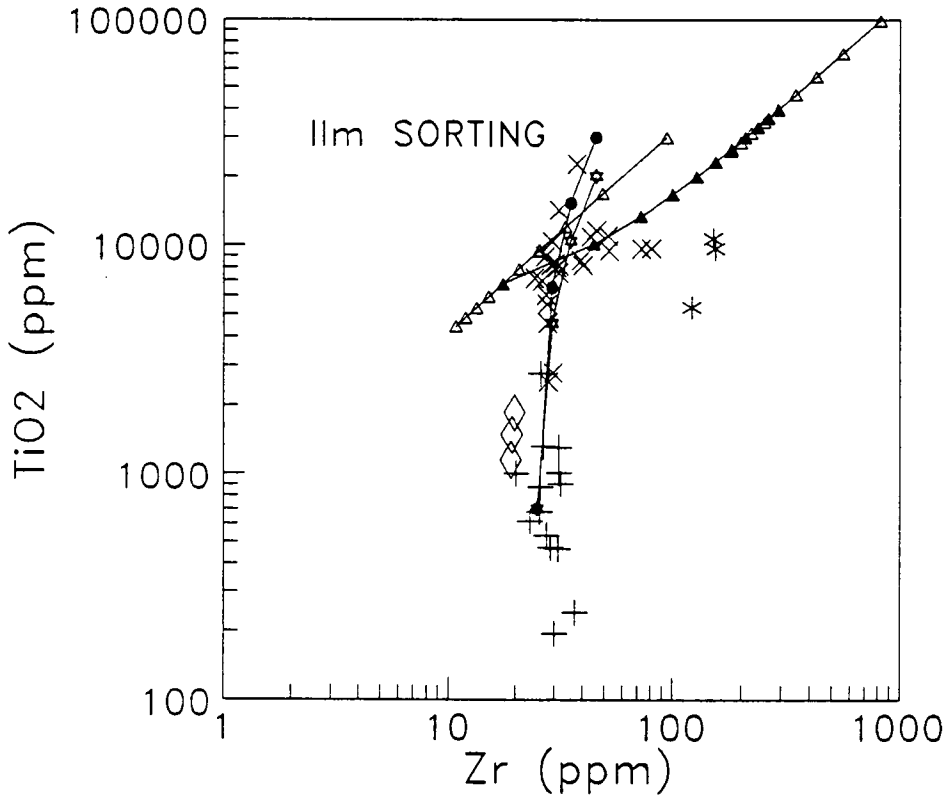

Figure 32. Carroll Knob Complex data for TiO_2 vs Zr with ilmenite sorting curves. $\bar{D}_{Zr}$ = 0.03, $\bar{D}_{TiO2}$ = 0.11, and D_{Zr}^{Ilm} = 0.28. Filled circles: D_{TiO2}^{Ilm} = 75, and open stars: D_{TiO2}^{Ilm} = 50. α = 0, at bottom of curve, 0.02, 0.05, 0.1. Chunky Gal Mountain CTL model curve and corresponding CFC model cumulate and liquid lines are also shown (symbols as in previous figures). Lithologic symbols as in previous figures.

possible to estimate pre-metamorphic modal abundances of ilmenite reliably, the hypothetical ilmenite mixing curves shown in Figure 32 indicate that mixing of only a few weight percent ilmenite with a typical metagabbro would produce the data pattern seen on the TiO_2 variation diagram. Unlike the mixing curves for olivine, the ilmenite curves fit the data well. This better behavior is mostly because the ilmenite partition coefficient for TiO_2 is so large that it overwhelms uncertainties in other partition coefficients, and the near vertical curve results.

The rocks of the epidosite/hornblendite association are rather enigmatic. Most occurrences of epidosite described in the literature are interpreted to be the result of metasomatism (Deer, Howie and Zussman, 1986), and one possibility, suggested by their textures and the similarity in their field occurrences, is that the epidosites are altered metagabbros, and the hornblendites are altered pyroxenites. No data are available on hornblendite compositions, but epidosite compositions tend to be quite different from the metagabbro compositions for major, minor and trace elements. Higher immobile, incompatible element concentrations could indicate that the epidosites represent late-stage differentiates of the Carroll Knob liquid, for example, diorites or trondjemites. Major element data, however, are not consistent with typical compositions of these rocks: the epidosites are much to rich in CaO and depleted in Na_2O.

Indeed the positions in which these rocks plot on the ACF diagram (Figure 20d) suggest that they may have a carbonate component. However, mixing a carbonate with a metagabbro would not produce the elevated trace-element concentrations. To explain the compositions of the epidosites then it seems necessary to invoke some combination of fractionation and contamination.

Phase Relations and Crystallization Sequences

The relict cumulate lithologies occurring at the three mafic/ultramafic complexes are consistent with the conclusion that the Carroll Knob liquid had a fundamentally different trace- and minor-element composition than the Chunky Gal Mountain/isolated amphibolite/Lake Chatuge liquid. As discussed earlier, the observed relict lithologies are: dunites and troctolites at Chunky Gal Mountain, dunites, troctolites, olivine gabbros and minor pyroxene gabbros at Lake Chatuge and websterites (Opx + Cpx), clinopyroxenites, two-pyroxene gabbros and clinopyroxene-gabbros at Carroll Knob. These lithologies imply two different crystallization sequences: Ol; Ol + Pl; Ol + Pl + Cpx, Pl + Cpx + Opx at Chunky Gal Mountain and Lake Chatuge and Opx; Opx + Cpx; Opx + Cpx + Pl; Cpx + Pl at Carroll Knob. Figures 33a and 33b are phase diagram models in the system Ol - Pl/Cpx - SiO_2 for these types of cumulate rocks, adapted from diagrams

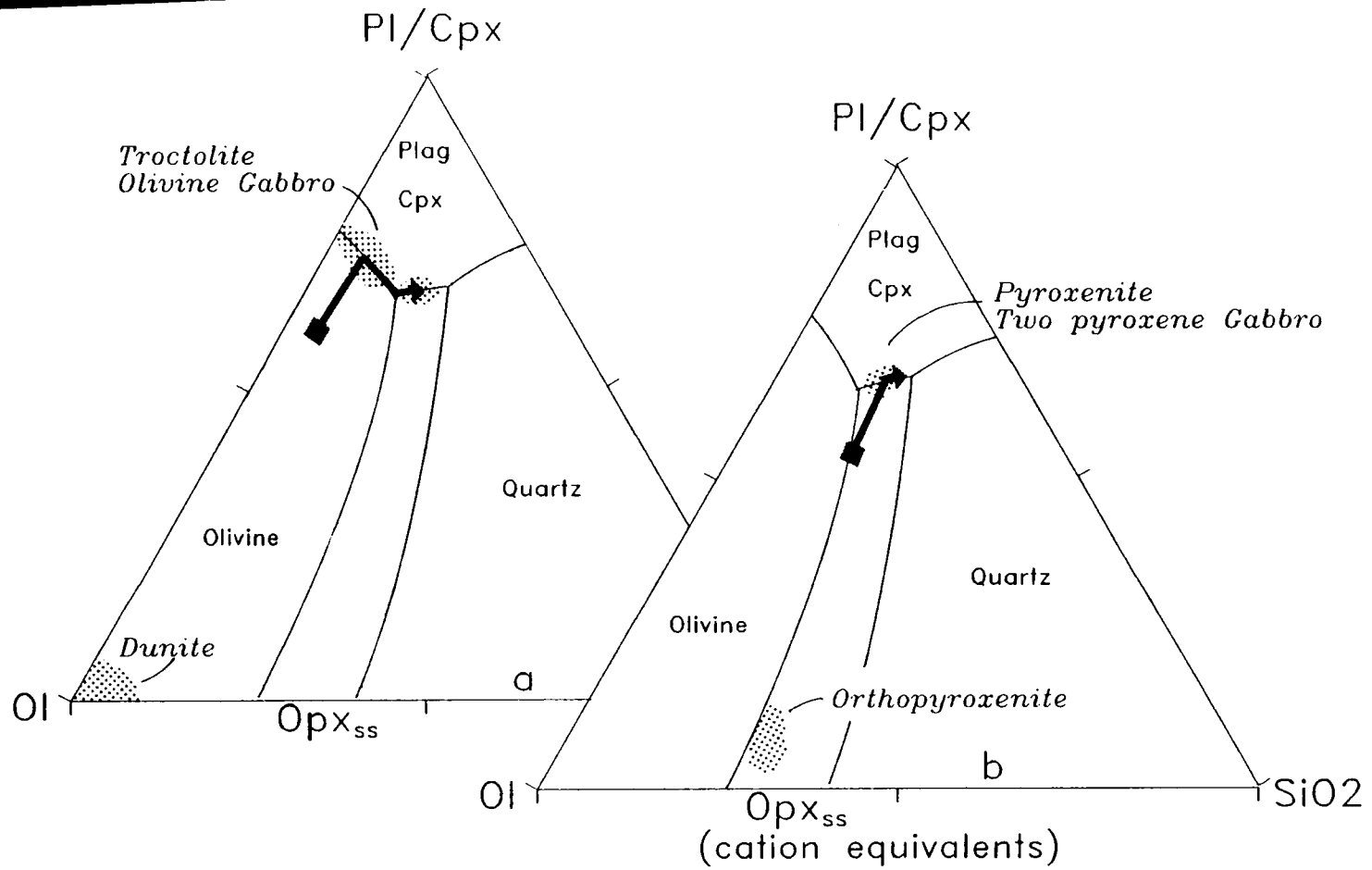

Figure 33. Phase diagram models adapted from Irvine (1970) showing hypothetical liquid compositions and liquid fractionation paths (connected squares and arrows) consistent with observed relict lithologies. (a) Chunky Gal Mountain and Lake Chatuge Complexes. (b) Carroll Knob Complex.

constructed by Irvine (1970). The figures show hypothetical liquid fractional crystallization paths implied by the relict cumulate assemblages at the complexes (Figure 33b allows for minor, as yet unobserved olivine at Carroll Knob). These diagrams illustrate that, for constant external conditions, the separate crystallization paths exhibited by the Carroll Knob and Chunky Gal Mountain-type liquids had to originate in different regions of composition space.

Because phase boundaries can be shifted substantially by changes in several parameters, the most important of which are lithostatic pressure and the partial pressure of water (P_{H2O}), and liquid compositions can be altered by assimilation, the phase relations illustrated in Figure 33 are only consistent with and do not prove different parent liquid compositions for the two complexes. Indeed the occurrence of apparently incompatible crystallization sequences in the same intrusion is a common feature of the large, layered continental intrusions. For example, both Chunky Gal Mountain-type and Carroll Knob-type sequences occur in the Muskox Intrusion and were explained by Irvine (1970) by an assimilation model in which the mixture of sialic roof rock with a liquid following a Chunky Gal Mountain-type liquid trend produces a liquid which follows a Carroll Knob-type liquid path (cf. Figures 33a and 33b). However, the low incompatible, trace-element abundances in the Carroll Knob estimated liquid composition relative to the Chunky Gal Mountain model liquid at any value

of F appear to rule out an assimilation relationship between the Chunky Gal Mountain and Carroll Knob liquids. Liquid mixing models involving the addition of SiO_2 can also be ruled out on a similar basis. Irvine (1970) also showed that a decrease in load pressure or P_{H2O} shifts phase boundaries away from the Pl/Cpx apex in Figure 33, in a manner that could lead to a transition in crystallizing assemblages from Carroll Knob-type to Chunky Gal Mountain-type. This model, however, is not convincing in the present case because it does not account for the clearly different trace- and minor-element compositions of the estimated Chunky Gal Mountain-type and Carroll Knob-type liquids. Thus, while not absolutely conclusive, phase relations and differences in crystallization sequences inferred from relict mineralogy support the trace- and minor-element evidence for fundamentally different parent liquid compositions for the Carroll Knob Complex and the other mafic rocks in the study area.

The differences in crystallization sequences for the Chunky Gal Mountain and related suites and for Carroll Knob are consistent with the different provenances for the suites suggested by the chemical data. The Chunky Gal Mountain-type crystallization sequence is the common sequence observed for ocean floor basalts. The Carroll Knob-type sequence is the common sequence for island arcs. This correlation between chemistry and crystallization sequence has also been noted for ophiolites, e.g. Bay of Islands (Chunky Gal Mountain-type)

versus Betts Cove (Carroll Knob-type), although some transitional types occur (Church and Riccio, 1977; Pearce et al., 1984; Serri, 1981).

CHAPTER VI

CONCLUSIONS

The discussions presented in the preceding chapters lead to two general conclusions regarding analyzing cumulate rocks:

1. Reliable conclusions about original tectonic settings of cumulate rocks cannot be derived by plotting their compositions directly on discriminant diagrams because cumulate processes significantly alter trace- and minor-element concentrations and ratios from liquid values.
2. Mathematical models can be used to identify the dominant processes that influenced compositional trends in cumulate rocks and to estimate liquid compositions. More realistic inferences about tectonic settings can be made from these model-derived liquid compositions.

The following are specific conclusions about the natures of and relationships among the mafic rocks of the eastern Blue Ridge in the study area:

1. The protoliths of the mafic rocks of all five suites were cumulate rocks.
2. The rocks from the Chunky Gal Mountain Complex, the Lake Chatuge Complex, Kimsey Bald amphibolites and the isolated amphibolites can all be derived from the same parent liquid and are almost certainly genetically related.

3. Trace- and minor-element trends and patterns in these suites are primarily the result of the trapping of residual liquid among cumulate crystals. The Lake Chatuge rocks are also strongly influenced by crystal sorting.

4. The model-derived liquid composition for the above suites is tholeiitic and consistent with genesis in either an ocean floor or a within-plate setting, but not with an island arc setting as previously suggested for the Chunky Gal Mountain, Kimsey Bald and Lake Chatuge amphibolites.

5. The Carroll Knob rocks had to have been derived from a liquid of different trace- and minor-element composition than the liquid that produced the other suites. The compositional patterns within the Carroll Knob suite are dominated by crystal sorting.

6. The estimated Carroll Knob liquid composition is consistent with a tholeiitic character and is most compatible with an island arc provenance.

7. Relict igneous lithologies and phase relations are consistent with different liquid compositions for the Carroll Knob Complex and the other suites and with the tectonic settings implied by the estimated liquid compositions.

REFERENCES

REFERENCES

Abbott, R. N., Jr., and Raymond, L. A., 1984, The Ashe metamorphic suite, northwest North Carolina: metamorphism and observations on geologic history: American Journal of Science, v. 284, p. 350-375.

Absher, B. S., and McSween, H. Y., 1985, Granulites at Winding Stair Gap, North Carolina: the thermal axis of Paleozoic metamorphism in the southern Appalachians: Geol. Soc. of America Bulletin, v. 96, p. 588-599.

Albarede, F., 1976, Some trace element relationships among liquid and solid phases in the course of the fractional crystallization of magmas: Geochimica et Cosmochimica Acta, v. 40, p. 667-673.

Allegre, C. J., Treuil, M., Minster, J. B., Minster, B., and Albarede, F., 1977, Systematic use of trace elements in igneous processes, part I: fractional crystallization processes in volcanic suites: Contrib. Mineral. Petrol., v. 60, p. 57-75.

Allegre, C. J., and Minster, J. F., 1978, Quantitative models of trace element behavior in magmatic processes: EPSL, v. 38, p. 1-25.

Anderson, A. T., and Greenland, L. P., 1969, Phosphorus fractionation diagram as a quantitative indicator of crystallization differentiation of basaltic liquids: Geochimica et Cosmochimica Acta, v. 33, p. 493-505.

Bence, A. E., and Albee, A. L., 1968, Empirical correction factors for the electron microanalysis of silicates and oxides: Journal of Geology, v. 76, p. 382-403.

Church, W. R., and Riccio, L., 1977, Fractionation trends in the Bay of Islands ophiolite of Newfoundland: polycyclic cumulate sequences in ophiolites and their classification: Can. J. Earth Sci., v14, p. 1156-1165.

Coish, R. A., 1977, Ocean floor metamorphism in the Betts Cove ophiolite, Newfoundland: Contrib. Mineral. Petrol., v. 60, p. 255-270.

Conte, J. A., 1986, Geochemistry and tectonic significance of amphibolites within the Precambrian Ashe Formation, northwestern North Carolina: unpublished M.S. thesis The University of Tennessee, Knoxville.

Cox, K. G., Bell, J. D., and Pankhurst, R. J., 1980, The Interpretation of Igneous Rocks: George Allen & Unwin, London, 450 p.

Dallmeyer, R. D., 1974, Eclogite inclusions in an Alpine peridotite sill, Georgia-North Carolina: their chemistry and petrogenetic evolution: American Journal of Science, v. 274, p. 356-377.

Deer, W. A., Howie, R. A., and Zussman, J., 1963, Rock-Forming Minerals, Volume 2 - Chain Silicates: John Wiley and Sons, Inc., New York.

Deer, W. A., Howie, R. A., and Zussman, J., 1986, Rock-Forming Minerals, Volume 1B - Disilicates and Ring Silicates: Longman Scientific & Technical, England, 629p.

DePaolo, D. J., 1981, Trace element and isotopic effects of combined wallrock assimilation and fractional crystallization: EPSL, v. 53, p. 189-202.

Eckert, J. O., Hathcher, R. D., Jr., and Mohr, D. W., 1989, The Wayah granulite-facies metamorphic core, southwestern North Carolina: high-grade culmination of Taconic metamorphism in the southern Blue Ridge: Geol. Soc. of America Bulletin, v. 101, p. 1434-1447.

Eggers, M. R., 1983, Petrology, structure and geochemistry of the Kimsey Bald mafic complex: unpublished M.S. thesis, University of South Carolina, Columbia, 72p.

Favret, P. D., and Williams, R. T., 1988, Basement beneath the Blue Ridge and Inner Piedmont in northeastern Georgia and the Carolinas: a preserved, late Proterozoic, rifted continental margin: Geol. Soc. of America Bulletin, v. 100, p. 1999-2007.

Fodor, R. V., and Vetter, S. K., 1984, Rift-zone magmatism: petrology of basaltic rocks transitional from CFB to MORB, southeastern Brazil margin: Contrib. Min. Petrol., v. 88, p. 307-321.

Fodor, R. V., 1987, Low- and high-TiO^2 flood basalts of southern Brazil: origin from picritic parentage and a common mantle source: EPSL, v. 84, p. 423-430.

Force, E. R., 1976, Metamorphic source rocks of titanium placer deposits - a geochemical cycle: U.S. Geological Survey Professional Paper 959-B, 14p.

Glover, L., III, Speer, J. A., Russell, G. S., and Farrar, S. S., 1983, Ages of regional metamorphism and ductile deformation in the central and southern Appalachians: Lithos, v. 16, p. 223-245.

Hartley, M. E., III, 1973, Ultramafic and related rocks in the vicinity of Lake Chatuge: Georgia Geological Survey Bulletin, v. 85, 61 p.

Hartley, M. E., III, and Penley, H. M., 1974, The Lake Chatuge sill outlining the Brasstown Antiform: Guidebook 13, The Geological Survey of Georgia, 27 p.

Hatcher, R. D., Jr., 1977, Macroscopic polyphase folding illustrated by the Toxaway dome, eastern Blue Ridge, South Carolina - North Carolina: Geol. Soc. America Bull., v. 88, p. 1678-1688.

Hatcher, R. D., Jr., 1978, Tectonics of the western Piedmont and Blue Ridge, southern Appalachians: review and speculation: American Journal of Science, v. 278, p. 276-304.

Hatcher, R. D., Jr., 1979, The Coweeta Group and Coweeta Syncline: major features of the North Carolina - Georgia Blue Ridge: Southeastern Geology, v. 21, p. 17-29.

Hatcher, R. D., Jr., and Odom, A. L., 1980, Timing of thrusting in the southern Appalachians, USA: model for orogeny?: Journ. Geol. Soc. London, v. 137, p. 321-327.

Hatcher, R. D., Jr., and Butler, J. R., 1979, Guidebook for southern Appalachian field trip in the Carolinas, Tennessee, and northeastern Georgia: International Geological Correlation Program, Caledonide Orogen Prog. 27 Fieldtrip guidebook, 117p.

Hatcher, R. D., Jr., Hooper, R. J., Petty, S. M., and Willis, J. D., 1984, Structure and chemical petrology of three southern Appalachian mafic-ultramafic complexes and their bearing upon the tectonics of emplacement and origin of Appalachian ultramafic bodies: American Journal of Science, v. 284, p. 484-506.

Hatcher, R. D., Jr., 1980, Geologic map and mineral resources summary of the Prentiss Quadrangle, North Carolina: North Carolina Department of Natural Resources and Community Development.

Hawkins, J. W., Jr., 1980, Petrology of back-arc basins and island arcs: their possible role in the origin of ophiolites: in Ophiolites - Proceedings International Ophiolite Symposium, Cyprus 1979, A. Panayiotou, ed., Cyprus Geological Survey Department, p. 244-254.

Helms, T. S., McSween, H. Y., Labotka, T. C., and Jarosewich, E., 1987, Petrology of a Georgia Blue Ridge amphibolite unit with hornblende + gedrite + kyanite + staurolite: American Mineralogist, v. 72, p. 1086-1096.

Henderson, P., 1984, General geochemical properties and abundances of the rare earth elements: in Rare Earth Element Geochemistry, P. Henderson, ed., Elsevier, Amsterdam, p. 1-29.

Hopson, J., 1990, personnel communication.

Huppert, H. E., and Sparks, R. S. J., 1985, Cooling and contamination of mafic and ultramafic magmas during ascent through continental crust: EPSL, v. 74, p. 371-386.

Irvine, T. N. and Baragar, W. R. A., 1971, A guide to the chemical classification of the common volcanic rocks: Can. J. Earth Sci., v. 8, p. 523-548.

Irvine, T. N., 1970, Crystallization sequences in the Muskox intrusion and other layered intrusions: in The Geological Society of South Africa, Special Publication 1, p. 441-476.

Irvine, T. N., 1979, Rocks whose composition is determined by crystal accumulation and sorting: in The Evolution of Igneous Rocks: Fiftieth Anniversary Perspectives, Princeton University Press, Princeton, p. 245-306.

Irvine, T. N., 1982, Terminology for layered intrusions: J. Petrol., v. 23, p. 127-162.

Irving, A. J., 1978, A review of experimental studies of crystal/liquid trace element partitioning: Geochim. Cosmochim. Acta, v. 42, p. 743-770.

Jones, L. M., Hartley, M. E., III, and Walker, R. L., 1973, Stontium isotope composition of Alpine-type ultramafic rocks in the Lake Chatuge district, Georgia-North Carolina: Contrib. Mineral. Petrol., v. 38, p. 321-327.

Kittleson, R., 1988, The amphibolite - to - granulite transition in the Franklin and Corbin Knob quadrangles, North Carolina Blue Ridge: unpublished M.S. thesis, The University of Tennessee, Knoxville.

Lacazette, J. R., 1986, Structural geology of the Chunky Gal Mountain, Clay county, North Carolina including a discussion of the mechanism of accretion of the Piedmont and a computer program for generating fabric density diagrams of the reference hemisphere: unpublished Ph.D. dissertation, University of Kentucky, Lexington, 331p.

Leake, B. E., 1964, The chemical distinction between ortho- and para-amphibolites: Journal. Petrol., v. 5, p. 238-254.

Libourel, G., Boivin, P., and Biggar, G. M., 1989, The univariant curve liquid = forsterite + anorthite + diopside in the system CMAS at 1 bar: solid solutions and melt structure: Contrib. Mineral. Petrol., v. 102, p. 406-421.

Lindsley, D. H., 1983, Pyroxene thermometry: American Mineralogist, v. 68, p. 477-493.

Long, L. K., 1983, The chemistry, genesis and tectonic significance of the Lake Chatuge mafic-ultramafic complex, North Carolina-Georgia: unpublished M.S. thesis, Vanderbilt University, Nashville, 115 p.

McElhaney, S. M., 1981, Petrogenesis of the Chunky Gal Mountain mafic-ultramafic complex: unpublished M.S. thesis, The University of Tennessee, Knoxville, 86p.

McElhaney, S. M., and McSween, H. Y., Jr., 1983, Petrology of the Chunky Gal Mountain mafic-ultramafic complex, North Carolina: Geol. Soc. America Bull., v. 94, p. 855-874.

McSween, H. Y., Jr., and Hatcher, R. D., 1985, Ophiolites (?) of the southern Appalachian Blue Ridge: in Field trips in the southern Appalachians.

Means, J. K., 1988, Mineral chemical variations in the Lake Chatuge mafic-ultrabasic complex North Carolina-Georgia: the pressue-temperature history of rocks in the Blue Ridge: unpublished draft paper sent to H. Y. McSween.

Minster, J. B., Treuil, M., and Allegre, C. J., 1977, Systematic use of trace elements in igneous processes, part II: inverse problem of the fractional crystallization process in volcanic suites: Contrib. Mineral. Petrol., v. 61, p. 49-77.

Misra, K. C., and Conte, J. A., in press, Amphibolites of the Ashe and Aligator Back Formations, North Carolina: Samples of late Proterozoic or early Paleozoic oceanic crust: submitted to Geol. Soc. of America Bulletin.

Misra, K. C., and McSween, H. Y., Jr., 1984, Mafic rocks of the southern Appalachians: a review: American Journal of Science, v. 284, p. 294-318.

Miyashiro, A. and Shido, F., 1975, Tholeiitic and calc-alkalic series in relation to the behaviors of titanium, vanadium, chromium, and nickel: American Journal of Science, v. 275, p. 265-277.

Morse, S. A., 1980, Basalts and Phase Diagrams: Springer-Verlag, New York, 493p.

Neumann, H., Mead, J., and Vitaliano, C. J., 1954, Trace element variation during fractional crystallization as calculated from the distribution law: Geochemica et Cosmochemica Acta, v. 6, p. 90-99.

O'Hara, M. J., and Mathews, R. E., 1981, Geochemical evolution in an advancing, periodically replenished, periodically tapped, continuously fractionated magma chamber: Journ. Geol. Soc. London, v.138, p. 237-277.

O'Hara, M. J., 1977, Geochemical evolution during fractional crystallization of a periodically refilled magma chamber: Nature, v. 266, p. 503-507.

Paster, T. P., Schauwecker, D. S., and Haskin, L. A., 1974, The behavior of some trace elements during solidification of the Skaergaard layered series: Geochemica et Cosmochemica Acta, v. 38, p. 1549-1577.

Pearce, J. A., and Cann, J. R., 1973, Tectonic setting of basic volcanic rocks determined using trace element analyses: EPSL, v. 19, p. 290-300.

Pearce, J. A., 1976, Statistical analysis of major element patterns in basalts: Journ. Petrol., v. 17, p. 15-43.

Pearce, J. A., Lippard, S. J., and Roberts, S., 1984, Characteristics and tectonic significance of supra-subduction zone ophiolites: in Kokelaar, B. P. and Howells, M. F., eds., Marginal Basin Geology, Geol. Soc. London Spec. Pub. 16, p. 77-94.

Pearce, J. A., and Norry, M. J., 1979, Petrogenetic implications of Ti, Zr, Y, and Nb variations in volcanic rocks: Contrib. Mineral. Petrol., v. 69, p. 33-47.

Presnall, D. C., Dixon, S. A., Dixon, J. R., O'Donnell, T. H., Brenner, N. L., Schrock, R. L., and Dycus, D. W., 1978, Liquidus phase relations on the join diopside-forsterite-anorthite from 1 atm to 20 kbar: their bearing on the generation and crystallization of basaltic magma: Contrib. Mineral. Petrol., v.66, p. 203-220.

Rankin, D. W., 1975, The continental margin of eastern North America in the southern Appalachians: the opening and closing of the Proto-Atlantic ocean: American Journal of Science, v. 275-A, p. 298-336.

Rankin, D. W., Espenshade, G. H., and Shaw, K. W., 1973, Stratigraphy and structure of the metamorphic belt in northwestern North Carolina and southwestern Virginia: a study from the Blue Ridge across the Brevard fault zone to the Sauratown Mountains anticlinorium: American Journal of Science, v. 273-A, p. 1-40.

Serri, G., 1981, The petrochemistry of ophiolite gabbroic complexes: a key for the classification of ophiolites into low-Ti and high-Ti types: EPSL, v. 52, p. 203-212.

Shaw, H. F. and Wasserburg, G. J., 1984, Isotopic constraints on the origin of Appalachian mafic complexes: American Journal of Science, v. 284, p. 416-436.

Smith, R. E., and Smith, S. E., 1976, Comments on the use of Ti, Zr, Y, Sr, K, P and Nb in classification of basaltic magmas: EPSL, v. 32, p. 114-120.

Taylor, H. P., 1980, The effects of assimilation of country rocks by magmas on $^{18}O/^{16}O$ and $^{87}Sr/^{86}Sr$ systematics in igneous rocks: EPSL, v. 47, p. 243-254.

Wager L. R., and Brown, G. M., 1967, Layered Igneous Rocks: W. H. Freeman and Company, San Francisco, 588p.

Watson, E. B., and Green, T. H., 1981, Apatite/liquid partition coefficients for the rare earth elements and strontium: EPSL, v. 56, p.405-421.

Wehr, F., and Glover, L., III, 1985, Stratigraphy and tectonics of the Virginia - North Carolina Blue Ridge: evolution of a late Proterozoic - early Paleozoic hinge zone: Geol. Soc. America Bull., v. 96, p. 285-295.

Williams, H, and Hatcher, R. D., Jr., 1982, Suspect terranes and accretionary history of the Appalachian orogen: Geology, v. 10, p. 530-536.

APPENDICES

APPENDIX A

ELECTRON MICROPROBE DATA AND GEOTHERMOMETRY FOR CARROLL KNOB COMPLEX PYROXENES

Analytical Methods

Chemical analyses of ortho- and clinopyroxenes from selected, well preserved metagabbros and pyroxenites from the Carroll Knob Complex were performed on the automated MAC 400S electron microprobe in use in the UTK Geological Sciences Department in 1985. Appropriate natural and synthetic standards were used for calibration. The pyroxenes were analyzed with a beam current of 0.05 μA, and a defocussed beam (~15 μ in diameter) was used to average the analyses over fine exsolution lamellae in the pyroxenes. Correction procedures were those of Bence and Albee (1968). At least three analyses were performed on each grain (unless otherwise indicated), and the results averaged.

Results and Two-Pyroxene Thermometry

The electron microprobe results show that the ortho- and clinopyroxenes of the metagabbros and the pyroxenites have about the same chemical composition. The clinopyroxenes are augites, and the orthopyroxenes are bronzites.

The microprobe results were used to infer the temperature of equilibration of the pyroxenes by the two-pyroxene thermometry method of Lindsley (1983). Pyroxene core compositions were used for thermometry to minimize reequilibration effects. The microprobe analyses were recalculated according to the procedure defined by Lindsley (1983) and projected onto his two-pyroxene thermometry diagram for a pressure of 5 kb. The pressure at which the pyroxenes crystallized is not known but is likely to have been in the 1 atm to 5 kb range. The temperature contours on Lindsley's diagrams at these two pressures are almost the same, and use of the 1 atm plot rather than the 5 kb plot would not make any difference in the inferred temperatures. The temperatures derived from Figure A.1 are 800 to 1000 ^{0}C for the clinopyroxenes and 700 to 800 ^{0}C for the orthopyroxenes, both of which are clearly in the igneous range. Lindsley (1983) estimates that the isotherms in the diagrams are accurate to approximately 20^{0} to 30^{0}, and that errors in composition introduce additional uncertainties of at least 20^{0} to 30^{0}. The differences between temperatures estimated for the two types of pyroxenes may reflect greater reequilibration in the orthopyroxenes; Lindsley (1983) notes that orthopyroxenes tend to reequilibrate more quickly than clinopyroxenes. However, they probably are also related to the fact that, because of the closeness of isotherms in the orthopyroxene region, small analytical errors in the small wollastonite component of the

orthopyroxenes can have large effects on the inferred temperature. The pyroxene analyses are shown in A.1 through A.3. The two-pyroxene thermometry diagram is shown in Figure A.1.

A.1. Representative Microprobe Analyses of Coexisting Pyroxenes from Carroll Knob Complex Metagabbros and Pyroxenites

	Sample CK73B		Sample CK73B	
	CPX3B1	OPX3B1	CPX3B3	OPX3B2
SiO_2	51.07 (0.30)*	53.68 (0.09)	50.89 (0.12)	53.43 (0.05)
Al_2O_3	3.39 (0.05)	2.58 (0.02)	3.33 (0.05)	2.66 (0.12)
MgO	15.54 (0.16)	27.49 (0.10)	15.34 (0.26)	27.05 (0.18)
Na_2O	0.16 (0.03)	0.02 (0.02)	0.10 (0.04)	0.01 (0.02)
TiO_2	0.13 (0.02)	0.05 (0.00)	0.14 (0.02)	0.05 (0.01)
CaO	23.27 (0.30)	0.55 (0.32)	24.50 (0.18)	0.25 (0.04)
FeO	5.86 (0.17)	14.92 (0.15)	4.86 (0.12)	15.53 (0.16)
MnO	0.20 (0.04)	0.27 (0.03)	0.12 (0.01)	0.27 (0.01)
Cr_2O_3	0.25 (0.02)	0.14 (0.00)	0.19 (0.01)	0.14 (0.03)
Total	99.86	99.71	99.49	99.39

*Numbers in parentheses are standard deviations of replicate analyses.
Sample CK73B is a metagabbro.
Total iron calculated as FeO.

A.1. Representative Microprobe Analyses of Coexisting Pyroxenes Carroll Knob Metagabbros and Pyroxenites (Cont.)

	Sample CK79**		Sample CK73B	
	CPX1A1	OPX1A2	CPX3B4	OPX3B5
SiO_2	50.63	53.88	51.04 (0.13)*	54.11 (0.13)
Al_2O_3	3.19	2.69	3.12 (0.06)	2.61 (0.05)
MgO	14.79	28.18	15.67 (0.15)	26.91 (0.13)
Na_2O	-	-	0.11 (0.03)	0.04 (0.03)
TiO_2	-	-	0.14 (0.01)	0.05 (0.01)
CaO	23.54	0.29	24.44 (0.07)	0.64 (0.33)
FeO	4.87	13.65	4.59 (0.24)	14.59 (0.23)
MnO	-	-	0.13 (0.02)	0.30 (0.02)
Cr_2O_3	-	-	0.17 (0.01)	0.13 (0.02)
Total	97.02	99.71	99.49	99.37

*Numbers in parentheses are standard deviations of replicate analyses.
**Based on one analysis and included as a check on sample to sample consistency.
- Not analyzed for.
Samples CK79 and CK73B are metagabbros.
Total iron calculated as FeO.

A.1. Representative Microprobe Analyses of Coexisting Pyroxenes Carroll Knob Metagabbros and Pyroxenites (Cont.)

	Sample CK22	
	CPX1B2	OPX1B4
SiO_2	52.31 (0.37)*	53.37 (0.19)
Al_2O_3	2.20 (0.17)	2.51 (0.05)
MgO	15.95 (0.13)	27.51 (0.04)
Na_2O	-	-
TiO_2	-	-
CaO	23.91 (0.02)	0.30 (0.02)
FeO	4.57 (0.14)	15.57 (0.19)
MnO	-	-
Cr_2O_3	-	-
Total	98.94	99.26

*Numbers in parentheses are standard deviations of replicate analyses.
Sample CK22 is a websterite.
- Not analyzed for.
Total iron calculated as FeO.

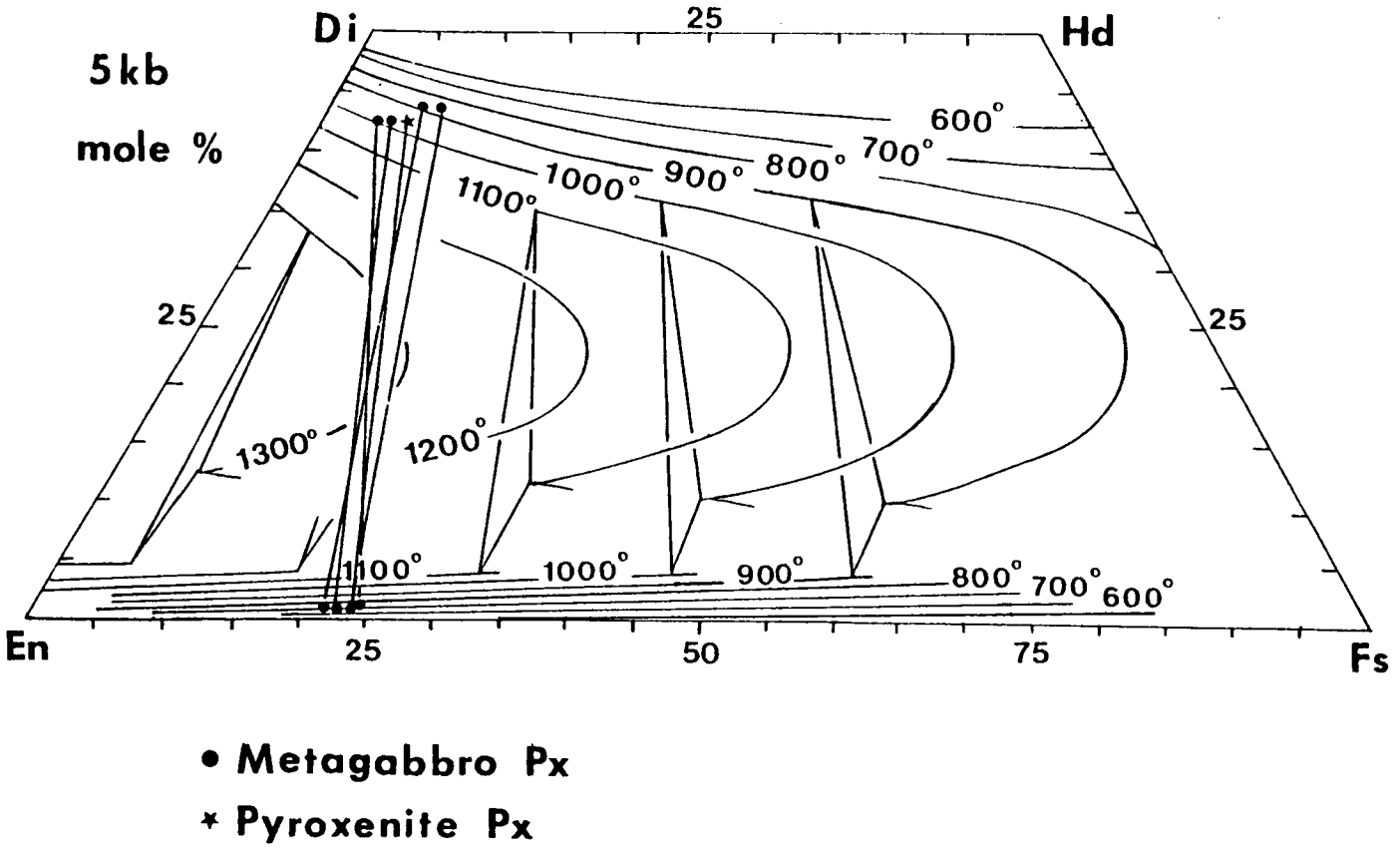

Figure A.1. Data for selected Carroll Knob Complex coexisting orthopyroxenes and clinopyroxenes projected onto a pyroxene quadrilateral showing polythermal orthopyroxene + augite, orthopyroxene + augite + pigeonite, and pigeonite + augite relations, contoured at 100 ^{0}C intervals for use in geothermometry (from Lindsley, 1983). Filled circles denote pyroxenes from metagabbros, and filled stars represent pyroxenes from a websterite.

APPENDIX B

XRF ANALYTICAL METHODS AND DATA

Sample Preparation

The XRF data for the Carroll Knob, Lake Chatuge, isolated amphibolite, and Chunky Gal Mountain suites were obtained on the UTK Geological Sciences Department's EG&G ORTEC model EEDS-II energy dispersive XRF equipment. Most of the Chunky Gal Mountain samples were the same pressed-powder pellets analyzed by McElhaney (1981). The Carroll Knob, Lake Chatuge, isolated amphibolite, and five Chunky Gal Mountain samples were pressed-powder pellets prepared according to the standard proceedures of the UTK Mineral Preparation Laboratory. The size of whole rock samples from which these pellets were made was at least 800 cm^3, i.e. somewhat larger than a standard handsample. Only samples that showed no signs of late-stage alteration and that had reasonably uniform mineral distributions, especially garnet distributions, were used. The whole rock samples were first crushed into pea-size pieces, a portion (~ 30 g) of which was then washed and dried. These pieces were then milled (6 minutes) into a powder, and a portion (~ 5 g) of the powder pressed into the final pellet. Throughout, care was taken not to contaminate samples. Final pressed powder pellets were stored in a dessicator.

Standards, Calibration and Results

The samples were analyzed using 19 USGS and South African rock standards and the IGROCK protocol (October, 1986). The standards used are shown in B.1. NORM 1 is a specially prepared glass sample used for normalization between different runs. The IGROCK protocol automatically sets appropriate run conditions and makes interelement corrections. Standard element values, errors of calibration and results of replicate analyses for selected standards are shown in B.2. Data for the samples from the four suites analyzed are shown in B.3 through B.6.

B.1. Standards used in IGROCK Protocol (October, 1986)

AGV-1	Andesite	BCR-1	Basalt
BHVO-1	Basalt	BIR-1	Basalt
DKBM	Basalt	DNC-1	Dunite
DTS-1	Dunite	G2	Granite
GSP-1	Granite	MRG-1	Gabbro
NORM-1	Glass	PCC-1	Dunite
RGM-1	Rhyolite	SARM3	Lujavrite
SARM4N	Norite	SARM5	Pyroxenite
SARM6D	Dunite	SRM688	Basalt
STM-1	Nepheline Syenite	W-2	Diabase

B.2. Values, Standard Error of Calibration and the Results of Analyses for Selected Standards

BCR-1

Element	Standard Value	Standard Error of Calibration	Analyses Average	Standard Deviation
(wt. %)				
Na2O	3.27	0.24	3.30	0.26
MgO	3.46	0.17	3.31	0.15
Al2O3	13.61	0.17	13.62	0.28
SiO2	54.50	0.45	54.74	0.61
Fe2O3	13.40	0.16	13.39	0.24
P2O5	0.36	0.03	0.31	0.04
K2O	1.70	0.04	1.67	0.04
CaO	6.92	0.07	6.81	0.04
MnO	0.18	0.01	0.18	0.002
TiO2	2.20	0.03	2.17	0.03
(ppm)				
V	399	30	209	5
Cr	18	50	138	16
Ni	16	21	54	13
Rb	47	4	35	2
Sr	330	13	349	5
Y	37	4	32	4
Zr	190	20	134	3
Nb	14	2	11	1

Averages and standard deviations based on seven replicate analyses.
Total iron calculated as FE2O3.

B.2. Values, Standard Error of Calibration and the Results of Analyses for Selected Standards (cont.)

W-2

Element	Standard Value	Standard Error of Calibration	Analyses Average	Standard Deviation
(wt. %)				
Na2O	2.20	0.24	2.18	0.11
MgO	6.37	0.17	6.31	0.09
Al2O3	15.45	0.17	15.30	0.09
SiO2	52.68	0.45	52.14	0.22
Fe2O3	10.80	0.16	10.74	0.07
P2O5	0.14	0.03	0.11	0.02
K2O	0.63	0.04	0.56	0.002
CaO	10.86	0.07	10.84	0.03
MnO	0.17	0.01	0.18	0.002
TiO2	1.06	0.03	1.06	0.01
(ppm)				
V	-	30	247	6
Cr	92	50	108	11
Ni	-	21	89	9
Rb	21	4	18	1
Sr	192	13	190	3
Y	23	4	24	1
Zr	100	20	80	1
Nb	7	2	7	1

Average and standard deviation based on seven replicate analyses.
Total iron calculated as FE2O3.
- No standard value.

B.2. Values, Standard Error of Calibration and the Results of Analyses for Selected Standards (cont.)

BIR-1

Element	Standard Value	Standard Error of Calibration	Analyses Average	Standard Deviation
(wt. %)				
Na2O	1.82	0.24	1.83	0.12
MgO	9.70	0.17	9.57	0.12
Al2O3	15.53	0.17	15.35	0.11
SiO2	47.96	0.45	48.26	0.23
Fe2O3	11.33	0.16	11.19	0.14
P2O5	0.02	0.03	0.017	0.02
K2O	0.03	0.04	0.08	0.002
CaO	13.32	0.07	13.33	0.04
MnO	0.18	0.01	0.18	0.002
TiO2	0.96	0.03	0.96	0.02
(ppm)				
V	-	30	329	5
Cr	373	50	308	17
Ni	166	21	169	8
Rb	2	4	3	1
Sr	107	13	115	29
Y	16	4	16	1
Zr	18	20	33	2
Nb	2	2	3	1

Average and standard deviation based on seven replicate analyses.
Total iron calculated as FE2O3.
- No standard value.

B.3. Carroll Knob Complex X-Ray Fluorescence Data

	Amphibolites							
	CK191A (a)	CK192 (b)	CK191B (c)	CK65 (d)	CK103 (e)	CK40C (f)	CK97 (g)	CK39 (h)
(wt. %)								
SiO2	47.50	47.94	45.95	48.35	46.70	47.14	52.35	46.95
Al2O3	16.79	18.10	16.52	18.74	15.69	21.40	15.99	16.59
Fe2O3	13.61	14.55	12.85	13.09	14.31	11.87	12.08	11.08
MgO	6.05	3.24	4.29	5.24	8.25	4.51	6.82	9.62
CaO	11.97	12.86	18.66	11.41	10.31	8.89	10.52	13.69
Na2O	2.97	3.06	0.34	3.02	1.31	3.45	0.80	0.94
K2O	0.30	0.28	0.16	0.17	0.60	0.55	0.16	0.12
TiO2	1.09	1.16	0.97	1.10	0.94	0.96	0.81	0.25
P2O5	0.08	0.00	0.06	0.14	0.04	0.06	0.11	0.03
MnO	0.33	0.25	0.39	0.18	0.19	0.13	0.15	0.19
Total	100.68	101.43	100.19	101.42	98.35	98.96	99.79	99.48
(ppm)								
Rb	3	4	7	3	6	12	3	5
Sr	56	56	439	102	227	408	50	127
Zr	44	46	80	52	52	73	40	28
Y	29	20	21	27	26	35	21	6
Ni	129	127	88	110	113	205	86	24
Nb	2	1	1	2	2	8	1	0
Cr	344	297	185	280	249	347	194	56
V	302	348	531	282	246	184	234	233

Letters in parentheses are keyed to sample locations shown in Figure 2.

B.3. Carroll Knob Complex X-Ray Fluorescence Data (Cont.)

	Garnet-Amphibolites							
	CK72 (i)	CK154 (j)	CK88 (k)	CK112 (l)	CK143A (m)	CK142 (n)	CK1 (o)	CK153 (p)
(wt. %)								
SiO2	45.92	46.80	43.33	44.10	46.36	47.62	44.63	44.98
Al2O3	18.38	15.61	18.74	18.91	21.85	18.83	18.71	20.79
Fe2O3	12.02	13.72	14.83	15.60	14.58	14.47	15.48	14.71
MgO	8.60	9.33	6.34	6.50	4.54	5.94	6.47	5.95
CaO	13.09	12.51	13.59	12.91	12.46	11.82	12.25	13.15
Na2O	1.49	1.75	2.33	1.67	1.76	1.70	1.65	1.21
K2O	0.18	0.24	0.26	0.17	0.12	0.06	0.23	0.06
TiO2	0.61	0.55	2.28	1.42	0.85	0.82	0.89	0.80
P2O5	0.05	0.07	1.67	0.20	0.34	0.20	0.08	0.10
MnO	0.20	0.22	0.27	0.21	0.26	0.22	0.19	0.19
Total	100.54	100.80	103.65	101.70	103.13	101.66	100.58	101.93
(ppm)								
Rb	4	6	5	5	3	2	3	2
Sr	138	121	251	202	231	170	152	178
Zr	28	28	38	31	39	29	27	31
Y	5	16	14	5	5	10	3	11
Ni	5	48	4	14	15	22	18	19
Nb	1	1	1	1	1	2	0	0
Cr	27	133	67	82	63	85	108	72
V	272	283	359	382	267	295	369	339

Letters in parentheses are keyed to sample locations shown in Figure 2.

B.3. Carroll Knob Complex X-Ray Fluorescence Data (Cont.)

	CK187 (q)	CK145 (r)	CK130A (s)	CK151 (t)	CK117 (u)	CK216 (v)	CK135 (w)	CK37 (x)
(wt. %)								
SiO2	43.61	44.74	44.24	45.44	46.33	45.68	49.07	42.84
Al2O3	18.41	16.82	18.16	18.87	16.21	18.53	17.02	22.44
Fe2O3	14.94	17.34	16.90	15.31	11.28	14.22	11.43	13.51
MgO	6.95	6.38	6.43	5.62	9.54	5.53	7.88	6.33
CaO	13.25	11.46	12.74	11.87	13.60	11.99	12.62	14.45
Na2O	1.25	1.20	1.23	1.52	1.20	1.52	0.98	0.55
K2O	0.16	0.15	0.13	0.23	0.17	0.29	0.04	0.10
TiO2	0.84	0.72	1.04	0.81	0.46	0.75	0.28	0.70
P2O5	0.01	0.02	0.17	0.20	0.05	0.15	0.06	0.01
MnO	0.18	0.31	0.22	0.27	0.18	0.21	0.22	0.16
Total	99.60	99.14	101.27	100.14	99.02	98.88	99.61	101.09
(ppm)								
Rb	4	4	4	4	4	3	3	4
Sr	173	122	170	198	112	182	131	147
Zr	30	24	29	31	28	31	30	26
Y	4	6	14	14	6	14	10	5
Ni	22	37	15	22	7	14	19	0
Nb	0	0	1	1	0	0	0	0
Cr	94	123	114	99	91	64	61	46
V	362	304	353	269	260	274	219	381

Letters in parentheses are keyed to sample locations shown in Figure 2.

B.3. Carroll Knob Complex X-Ray Fluorescence Data (Cont.)

	Metagabbros							
	CK45 (y)	CK73B (z)	CK79 (a′)	CK20B (b′)	CK92 (c′)	CK9 (d′)	CKTB (e′)	CK2 (f′)
(wt. %)								
SiO2	47.74	48.98	51.25	46.11	47.18	47.59	48.07	48.63
Al2O3	15.35	18.66	9.00	23.93	22.57	20.47	19.21	18.78
Fe2O3	11.75	6.15	9.02	5.70	6.23	7.32	7.58	5.66
MgO	10.01	10.98	17.40	8.56	8.89	10.40	11.47	10.66
CaO	13.70	16.72	14.16	16.49	15.47	13.43	13.84	15.31
Na2O	1.34	0.61	0.82	0.79	1.10	0.96	0.79	1.57
K2O	0.08	0.03	0.04	0.05	0.08	0.06	0.04	0.17
TiO2	0.28	0.06	0.10	0.05	0.05	0.09	0.07	0.13
P2O5	0.07	0.13	0.11	0.10	0.13	0.09	0.09	0.11
MnO	0.22	0.11	0.18	0.07	0.10	0.13	0.13	0.09
Total	100.55	102.43	102.07	101.86	101.80	100.53	101.29	101.11
(ppm)								
Rb	4	5	3	5	5	5	4	10
Sr	86	58	26	112	131	109	89	75
Zr	26	23	20	29	31	32	26	27
Y	9	6	5	6	3	7	16	12
Ni	12	78	152	11	36	16	37	75
Nb	1	1	0	1	0	1	0	1
Cr	40	385	754	54	14	13	41	340
V	238	236	230	183	170	161	172	191

Letters in parentheses are keyed to sample locations shown in Figure 2.

B.3. Carroll Knob Complex X-Ray Fluorescence Data (Cont.)

	CK4 (g′)	CK166D (h′)	CK165B (i′)	CK124 (j′)	CK93 (k′)	CK173 (l′)	CK85 (m′)
(wt. %)							
SiO2	48.66	46.61	45.71	46.81	45.97	47.85	45.98
Al2O3	20.15	20.56	30.32	17.54	21.88	16.49	27.63
Fe2O3	5.56	4.44	2.60	6.87	8.23	8.69	5.42
MgO	10.35	11.24	6.04	12.50	9.15	11.43	6.26
CaO	16.23	16.86	17.35	13.65	14.20	13.69	15.46
Na2O	0.92	0.32	0.55	0.92	0.97	0.97	0.77
K2O	0.07	0.10	0.06	0.19	0.12	0.10	0.07
TiO2	0.05	0.02	0.00	0.10	0.13	0.09	0.02
P2O5	0.11	0.03	0.07	0.03	0.06	0.04	0.06
MnO	0.09	0.05	0.00	0.10	0.10	0.15	0.07
Total	102.17	100.23	102.69	98.71	100.81	99.48	101.74
(ppm)							
Rb	6	7	8	5	6	4	8
Sr	86	106	119	127	149	94	185
Zr	28	30	33	31	31	26	37
Y	4	7	3	7	8	2	4
Ni	0	0	0	200	16	40	0
Nb	0	0	0	0	0	0	0
Cr	0	0	17	503	39	2	0
V	197	175	140	151	189	176	136

Letters in parentheses are keyed to sample locations shown in Figure 2.

B.3. Carroll Knob Complex X-Ray Fluorescence Data (Cont.)

	Pyroxenites			Epidosites		
	CK171B (n′)	CK80 (o′)	CK49 (p′)	CK183 (q′)	CK16C (r′)	CK195B (s′)
(wt. %)						
SiO2	44.71	53.64	53.53	42.60	51.93	53.33
Al2O3	6.47	3.63	4.78	22.48	16.80	15.60
Fe2O3	19.59	6.46	10.01	9.73	8.06	8.14
MgO	26.37	16.69	17.17	2.31	3.57	2.68
CaO	0.41	20.50	13.11	22.23	18.26	19.47
Na2O	0.00	0.84	1.13	0.00	0.04	0.00
K2O	0.00	0.08	0.10	0.10	0.12	0.07
TiO2	0.19	0.12	0.15	0.54	1.07	0.96
P2O5	0.00	0.14	0.14	0.42	0.58	0.47
MnO	0.31	0.21	0.18	0.15	0.14	0.15
Total	98.05	102.30	100.30	100.54	100.58	100.87
(ppm)						
Rb	1	6	4	11	9	16
Sr	9	9	15	666	815	941
Zr	20	19	19	121	151	154
Y	3	10	4	37	21	30
Ni	330	93	171	0	0	0
Nb	1	0	0	7	14	15
Cr	859	1053	1005	0	0	0
V	59	407	229	582	412	458

Letters in parentheses are keyed to sample locations shown in Figure 2.

B.4. Chunky Gal Mountain Complex X-Ray Fluorescence Data

	Amphibolites							
	1AM8I (a)	6AM25I (b)	6AM34I (c)	8-42I (d)	9-18I (e)	11AM9I (f)	12-1I (g)	12-2I (h)
(wt. %)								
SiO2	47.33	43.81	45.04	49.48	45.26	46.12	47.45	48.90
Al2O3	9.22	12.59	14.84	15.32	15.53	14.98	15.38	14.71
Fe2O3	12.91	15.13	14.82	12.39	12.94	13.16	10.21	10.97
MgO	12.80	8.89	8.03	8.00	7.86	8.71	7.22	8.56
CaO	12.27	11.81	11.64	9.57	11.78	11.39	16.71	12.27
Na2O	1.38	2.85	2.16	1.71	1.59	1.79	1.75	1.11
K2O	0.45	0.52	0.28	0.32	0.29	0.36	0.15	0.20
TiO2	0.69	1.36	1.12	0.97	0.98	0.92	0.91	0.76
P2O5	0.21	0.09	0.01	0.04	0.00	0.01	0.05	0.01
MnO	0.19	0.20	0.21	0.20	0.20	0.19	0.19	0.16
Total	97.44	97.27	98.14	98.00	96.42	97.62	100.01	97.66
(ppm)								
Rb	7	7	4	7	6	4	7	5
Sr	53	64	73	163	86	76	94	58
Zr	35	54	40	54	41	40	46	40
Y	50	37	28	28	32	28	21	26
Ni	801	146	134	137	223	147	83	108
Nb	6	7	3	3	4	2	1	2
Cr	1972	390	218	222	486	269	178	263
V	290	340	311	233	308	270	452	261

Letters in parentheses are keyed to sample locations shown in Figure 3.

B.4. Chunky Gal Mountain Complex X-Ray Fluorescence Data (Cont.)

	13-7I (i)	T7I (j)	2AM3II (k)	2-18II (l)	3-28II (m)	3-32II (n)	4-1II (o)	4-10II (p)
(wt. %)								
SiO2	47.23	46.19	48.18	47.39	45.23	46.85	47.17	47.54
Al2O3	14.88	14.61	13.10	13.48	14.30	13.36	13.23	13.92
Fe2O3	11.15	12.54	13.67	13.71	14.33	12.97	12.10	11.96
MgO	8.17	8.22	7.24	6.91	7.37	8.21	5.98	7.04
CaO	11.61	13.16	10.84	12.01	11.36	11.17	13.04	12.08
Na2O	1.97	2.31	2.54	1.72	2.76	2.77	2.75	3.15
K2O	0.23	0.19	0.38	0.41	0.60	0.39	0.35	0.34
TiO2	0.90	1.33	1.68	1.72	1.67	1.31	1.65	1.18
P2O5	0.03	0.07	0.12	0.14	0.11	0.09	0.16	0.07
MnO	0.20	0.18	0.17	0.18	0.19	0.20	0.19	0.17
Total	96.38	98.80	97.93	97.68	97.93	97.32	96.62	97.44
(ppm)								
Rb	8	5	5	8	6	6	10	5
Sr	106	152	163	317	153	170	304	200
Zr	46	62	81	94	82	63	98	64
Y	28	27	33	33	28	28	31	24
Ni	147	71	104	110	106	109	129	88
Nb	5	4	6	7	7	4	8	3
Cr	277	278	228	300	274	333	283	259
V	265	346	300	342	311	294	371	298

Letters in parentheses are keyed to sample locations shown in Figure 3.

B.4. Chunky Gal Mountain Complex X-Ray Fluorescence Data (Cont.)

	5-5II (q)	5-21II (r)	8-2II (s)	8-9II (t)	8-15II (u)	10-7II (v)	CG1 (w)	CG3 (x)
(wt. %)								
SiO2	50.95	48.68	46.81	46.28	45.32	47.99	46.25	46.17
Al2O3	15.00	13.13	13.73	13.56	14.69	13.59	13.70	13.95
Fe2O3	12.96	13.22	13.79	13.49	13.84	13.36	12.90	12.70
MgO	4.44	6.18	6.80	7.59	8.85	6.92	9.89	9.96
CaO	8.88	13.46	10.38	11.00	10.85	12.32	12.26	11.97
Na2O	3.71	1.71	2.63	3.37	2.75	2.63	2.11	2.13
K2O	0.34	0.30	0.47	0.48	0.46	0.42	0.28	0.25
TiO2	1.86	1.70	1.96	1.75	0.94	1.65	0.91	0.89
P2O5	0.31	0.14	0.17	0.16	0.05	0.13	0.05	0.06
MnO	0.21	0.20	0.21	0.19	0.21	0.19	0.19	0.19
Total	98.66	98.75	96.97	97.86	97.96	99.20	98.52	98.27
(ppm)								
Rb	4	7	7	8	7	7	4	3
Sr	249	242	173	199	78	247	89	81
Zr	138	87	97	84	39	88	40	41
Y	44	29	41	29	30	27	26	25
Ni	68	78	119	96	161	84	114	131
Nb	11	6	8	6	4	5	1	1
Cr	145	231	273	290	347	254	317	329
V	227	392	300	291	267	334	299	277

Letters in parentheses are keyed to sample locations shown in Figure 3.

B.4. Chunky Gal Mountain Complex X-Ray Fluorescence Data (Cont.)

	Dunites		
	CG4 (y)	CG6 (z)	CG5 (a′)
(wt. %)			
SiO2	47.66	40.43	40.15
Al2O3	14.61	1.02	1.27
Fe2O3	12.19	10.84	10.71
MgO	8.52	44.47	44.77
CaO	11.50	0.00	0.02
Na2O	2.66	0.26	0.14
K2O	0.22	0.00	0.00
TiO2	0.93	0.03	0.02
P2O5	0.07	0.01	0.03
MnO	0.18	0.15	0.14
Total	98.55	97.22	97.25
(ppm)			
Rb	4	0	0
Sr	88	5	6
Zr	43	24	23
Y	23	2	2
Ni	139	2126	2568
Nb	1	1	1
Cr	369	4104	4176
V	272	28	27

Letters in parentheses are keyed to sample locations shown in Figure 3.

B.5. Isolated Amphibolites X-Ray Fluorescence Data

	Amphibolites							
	CN5B (a)	CN81C (b)	F44A (a)	F19B (b)	F48A (c)	F39A (d)	F50A (e)	F38F (f)
(wt. %)								
SiO2	47.14	49.18	49.07	51.93	47.60	47.27	48.82	47.60
Al2O3	13.72	13.23	15.18	14.85	14.84	17.18	14.80	15.50
Fe2O3	15.85	14.73	12.47	11.66	10.98	10.04	11.04	12.57
MgO	6.90	6.58	6.36	6.97	8.70	9.17	7.70	8.38
CaO	8.47	11.11	11.64	11.27	13.45	10.91	12.87	9.90
Na2O	1.82	1.03	2.89	1.10	1.86	2.53	2.44	2.54
K2O	1.42	0.41	0.56	0.39	0.10	0.27	0.23	0.38
TiO2	2.85	2.59	1.86	1.54	1.10	0.92	1.34	1.31
P2O5	0.40	0.36	0.24	0.29	0.11	0.08	0.14	0.04
MnO	0.19	0.21	0.17	0.17	0.19	0.15	0.17	0.20
Total	98.75	99.45	100.45	100.18	98.93	98.53	99.55	98.41
(ppm)								
Rb	24	6	5	5	3	5	4	4
Sr	399	196	270	390	84	244	93	172
Zr	123	123	100	101	46	80	54	71
Y	35	45	31	27	28	23	33	31
Ni	90	53	52	33	57	146	10	88
Nb	17	7	5	5	1	3	1	6
Cr	200	162	159	202	239	179	58	315
V	246	330	321	287	318	222	325	240

Letters in parentheses are keyed to sample locations shown in Figure 1.
Quadrangles: CN Corbin Knob and F Franklin.

B.5. Isolated Amphibolites X-Ray Fluorescence Data (Cont.)

	F41B (g)	F49A (h)	FR17 (i)	FR13 (j)	F19D (k)	P4 (a)	FR15 (l)	P2 (b)
(wt. %)								
SiO2	46.71	49.23	47.30	52.38	49.21	47.02	48.86	48.05
Al2O3	13.22	14.43	13.15	15.16	15.65	16.47	14.23	15.81
Fe2O3	16.03	10.82	16.17	10.86	10.66	12.58	16.61	12.23
MgO	6.85	7.54	7.57	7.39	6.81	7.91	7.73	8.36
CaO	10.99	11.22	11.85	9.53	10.51	9.95	10.46	10.81
Na2O	2.52	3.10	2.42	2.04	2.68	2.63	1.52	2.75
K2O	0.60	0.23	0.30	0.61	1.05	0.73	0.37	0.40
TiO2	2.48	1.46	2.51	1.12	1.44	1.69	2.42	1.55
P2O5	0.20	0.14	0.20	0.14	0.15	0.22	0.19	0.24
MnO	0.21	0.20	0.17	0.18	0.12	0.28	0.23	0.20
Total	99.80	98.36	101.63	99.41	98.29	99.49	102.62	100.40
(ppm)								
Rb	5	5	4	8	15	13	6	6
Sr	536	192	211	152	344	382	212	390
Zr	99	74	76	96	104	110	72	107
Y	24	31	24	33	25	22	26	21
Ni	94	3	125	53	60	69	132	61
Nb	7	4	8	7	3	9	8	7
Cr	209	198	270	47	168	138	286	99
V	332	265	376	228	262	258	337	284

Letters in parentheses are keyed to sample locations shown in Figure 1.
Quadrangles: F and FR Franklin and P Prentiss.

B.5. Isolated Amphibolites X-Ray Fluorescence Data (Cont.)

	RBS1 (a)	RBS7 (b)	RBS5 (c)	RBS6 (g)	HB2918P (a)	HB3007 (b)	HB1881 (c)	HB2707 (d)
(wt. %)								
SiO2	45.94	49.40	45.69	49.76	47.22	44.50	45.65	48.54
Al2O3	22.90	13.09	21.51	12.95	20.05	17.60	17.15	14.00
Fe2O3	10.66	15.92	10.08	14.67	13.17	13.44	13.56	12.17
MgO	5.60	7.09	7.77	8.12	4.49	8.40	7.24	8.36
CaO	12.90	9.92	11.82	11.01	9.22	9.78	9.89	12.27
Na2O	2.11	3.11	2.35	2.69	3.84	2.66	3.47	1.42
K2O	0.33	0.09	0.24	0.23	0.37	0.31	0.22	0.22
TiO2	0.88	1.25	0.55	1.14	0.97	0.93	0.91	0.87
P2O5	0.15	0.10	0.31	0.13	0.05	0.04	0.06	0.04
MnO	0.11	0.27	0.11	0.22	0.21	0.14	0.16	0.21
Total	101.57	100.25	100.42	100.94	99.59	97.80	98.31	98.10
(ppm)								
Rb	16	2	9	3	4	5	4	5
Sr	97	121	178	253	181	127	129	83
Zr	50	53	49	56	53	47	46	44
Y	26	33	18	27	23	24	28	25
Ni	82	50	144	59	138	184	139	98
Nb	1	3	0	5	2	2	3	2
Cr	0	112	19	121	250	92	92	167
V	259	279	182	299	241	197	200	287

Letters in parentheses are keyed to sample locations shown in Figure 1.
Quadrangles: RBS Rainbow Springs and HB Hightower Bald.

B.5. Isolated Amphibolites X-Ray Fluorescence Data (Cont.)

	HB1882 (e)	HB2895 (f)	HB2918 (g)	HB3122 (h)	SC4 (b)	SC1 (a)	RBS10 (d)	RBS11 (e)
(wt. %)								
SiO2	44.53	49.05	50.83	49.85	49.53	51.02	47.25	45.16
Al2O3	16.82	13.94	13.70	16.55	11.58	15.01	18.89	14.51
Fe2O3	15.05	11.83	11.64	12.86	10.62	9.25	11.20	14.94
MgO	7.50	7.42	7.94	5.46	10.93	9.38	4.86	9.56
CaO	9.25	12.09	10.21	9.33	14.66	12.33	21.07	13.31
Na2O	3.13	1.63	1.68	3.29	2.13	1.74	0.90	1.28
K2O	0.19	0.48	0.38	0.25	0.54	0.52	0.14	0.27
TiO2	1.16	1.15	0.87	1.06	1.02	0.85	0.80	0.93
P2O5	0.03	0.11	0.07	0.02	0.20	0.16	0.18	0.09
MnO	0.22	0.19	0.22	0.19	0.18	0.15	0.16	0.17
Total	97.87	97.89	97.54	98.87	101.40	100.42	105.47	100.22
(ppm)								
Rb	4	9	5	3	11	9	18	6
Sr	141	172	51	81	164	144	954	201
Zr	39	66	42	49	69	72	125	59
Y	19	22	25	24	23	20	12	25
Ni	152	61	97	87	85	134	10	71
Nb	4	4	2	2	2	3	0	3
Cr	71	224	167	164	269	542	10	154
V	207	312	223	223	381	264	663	349

Letters in parentheses are keyed to sample locations shown in Figure 1.
Quadrangles: RBS Rainbow Springs, HB Hightower Bald and SC Shooting Creek.

B.5. Isolated Amphibolites X-Ray Fluorescence Data (Cont.)

	RBS12 (f)	WB4 (a)	WB9 (b)	WB2 (c)
(wt. %)				
SiO2	59.63	47.93	48.98	50.20
Al2O3	13.32	16.98	15.08	14.20
Fe2O3	11.54	10.91	11.17	11.68
MgO	3.33	8.87	9.09	7.77
CaO	14.27	11.03	11.96	11.61
Na2O	0.92	2.40	1.64	2.09
K2O	0.10	0.19	0.48	0.35
TiO2	1.30	1.33	1.38	1.54
P2O5	0.22	0.16	0.18	0.20
MnO	0.18	0.15	0.21	0.19
Total	104.82	99.95	100.16	99.83
(ppm)				
Rb	6	4	7	7
Sr	154	123	272	199
Zr	82	70	89	87
Y	64	29	30	37
Ni	27	133	56	89
Nb	9	4	3	4
Cr	45	173	310	249
V	387	276	321	304

Letters in parentheses are keyed to sample locations shown in Figure 1.
Quadrangles: RBS Rainbow Springs and WB Wayah Bald.

B.6. Lake Chatuge Complex X-Ray Fluorescence Data

	Amphibolites							
	LCH13 (a)	LCH31 (b)	LCH3 (c)	LCH29 (d)	LCH11 (e)	LCH1 (f)	LCH12 (g)	LCH10 (h)
(wt. %)								
SiO2	48.09	48.12	43.64	48.00	46.83	44.42	48.95	48.12
Al2O3	15.21	13.61	13.29	13.46	14.66	12.71	13.69	14.24
Fe2O3	10.83	13.55	13.54	13.65	12.33	12.61	12.85	11.92
MgO	8.68	7.04	10.49	6.99	8.73	10.71	7.76	7.36
CaO	12.89	12.01	14.35	12.35	13.18	14.71	11.48	14.24
Na2O	1.58	2.56	1.75	2.56	1.55	1.66	2.49	2.05
K2O	0.14	0.24	0.13	0.25	0.25	0.14	0.27	0.14
TiO2	0.75	1.46	1.26	1.51	0.93	1.29	1.13	1.25
P2O5	0.04	0.15	0.00	0.16	0.05	0.07	0.13	0.12
MnO	0.18	0.21	0.17	0.20	0.19	0.18	0.22	0.20
Total	98.40	98.97	98.62	99.14	98.68	98.49	98.97	99.64
(ppm)								
Rb	5	5	3	5	4	6	5	3
Sr	130	142	112	135	123	129	140	127
Zr	47	69	35	67	41	43	62	61
Y	22	30	21	28	20	28	25	26
Ni	41	53	112	49	32	97	58	60
Nb	1	5	1	3	1	2	3	4
Cr	156	176	307	152	123	285	244	218
V	285	324	407	341	329	405	285	380

Letters in parentheses are keyed to sample locations in Figure 4.

B.6. Lake Chatuge Complex X-Ray Fluorescence Data (Cont.)

	LCH8 (i)	LCH24 (j)	LCH26 (k)	LCH4 (l)	LCH22 (m)	LCH25 (n)	LCH28 (o)	LCH30 (p)
(wt. %)								
SiO2	47.72	47.73	46.42	43.36	46.44	46.83	47.89	48.00
Al2O3	15.13	12.89	13.03	14.11	14.17	12.27	13.51	13.35
Fe2O3	10.74	13.71	14.46	13.98	12.44	14.45	13.54	13.76
MgO	9.59	7.82	7.05	9.93	8.98	8.44	7.26	7.15
CaO	13.73	12.09	12.44	14.13	13.99	13.04	12.01	12.21
Na2O	1.35	2.26	1.86	1.60	1.93	1.78	2.24	2.46
K2O	0.16	0.23	0.18	0.34	0.05	0.19	0.31	0.24
TiO2	0.75	1.57	1.98	1.48	1.27	1.67	1.51	1.51
P2O5	0.08	0.11	0.15	0.00	0.04	0.04	0.15	0.15
MnO	0.20	0.22	0.17	0.17	0.19	0.22	0.19	0.20
Total	99.46	98.63	97.75	99.09	99.49	98.92	98.60	99.03
(ppm)								
Rb	6	5	4	6	4	3	6	4
Sr	123	129	139	248	120	129	171	140
Zr	44	44	42	48	33	36	70	66
Y	20	26	24	22	14	25	29	32
Ni	36	63	114	81	88	71	59	53
Nb	1	3	3	1	0	1	4	4
Cr	145	133	114	329	314	163	165	166
V	306	340	377	413	388	384	326	337

Letters in parentheses are keyed to sample locations in Figure 4.

B.6. Lake Chatuge Complex X-Ray Fluorescence Data (Cont.)

	Gabbros			Olivine-Gabbros					
	LCH20 (q)	LCH6 (r)	LCH7 (s)	LCH2 (t)	LCH34 (u)	LCH17 (v)	LCH16 (w)	LCH18 (x)	LCH17A (y)
(wt. %)									
SiO2	49.21	48.14	47.25	43.55	44.06	44.05	44.11	44.44	44.35
Al2O3	13.92	15.00	15.68	12.11	12.93	12.79	13.14	13.03	11.90
Fe2O3	7.64	5.41	7.99	5.50	9.47	10.02	9.90	9.56	10.23
MgO	10.96	12.66	10.58	29.13	21.38	22.78	22.73	21.78	22.06
CaO	14.92	16.31	16.94	8.37	9.95	9.22	9.43	10.01	10.26
Na2O	1.50	0.86	1.43	0.50	0.95	0.95	0.75	0.86	0.89
K2O	0.08	0.07	0.06	0.04	0.05	0.05	0.04	0.04	0.05
TiO2	0.55	0.23	0.48	0.00	0.08	0.06	0.03	0.06	0.11
P2O5	0.08	0.04	0.08	0.06	0.03	0.00	0.02	0.02	0.02
MnO	0.13	0.07	0.13	0.10	0.14	0.16	0.16	0.15	0.16
Total	98.99	98.80	100.61	99.36	99.03	100.10	100.31	99.94	100.03
(ppm)									
Rb	5	6	6	4	4	4	3	4	3
Sr	105	261	90	77	94	96	91	95	90
Zr	41	49	32	26	27	27	26	27	26
Y	17	11	15	3	4	3	3	4	5
Ni	82	135	103	1068	465	512	506	471	466
Nb	0	0	0	0	1	0	1	0	0
Cr	594	284	246	907	344	244	286	332	667
V	278	255	353	63	103	81	87	99	115

Letters in parentheses are keyed to sample locations in Figure 4.

VITA

Kathryn A. Walter received her B.S. and M.S. degrees in physics from Indiana University in 1969 and 1971, respectively. For the next ten years she worked for the U.S. Department of Energy (U. S. DOE) and its predecessors in technical staff and management positions in Washington, D. C. and Oak Ridge, TN. While pursuing a Ph.D. in geology at the University of Tennessee, she worked for several years as a technical writer. During the last two years she was a full-time consultant to Oak Ridge National Laboratory engaged in computer modeling of contaminant transport and evaluation of remedial alternatives for hazardous waste sites. She is currently employed by Automated Sciences Group and is on assignment to DOE's Hazardous Waste Remedial Action Program (HAZWRAP) as a geochemist and hydrogeologist. She is a member of the Geological Society of America and the Association of Ground Water Scientists and Engineers.